POME-derived Ag/TiO_2-based ternary nanocomposites for oxytetracycline degradation under visible light and membrane integration

by

Danielson Ngo Joseph
(23020173)

Presented to the
FACULTY OF RESOURCE SCIENCE AND TECHNOLOGY
in Fulfillment of the Requirement for the Degree of

MASTER OF SCIENCE
(Environmental Science)

2026

UNIVERSITI MALAYSIA SARAWAK

DECLARATION

I hereby declare that the work presented in this thesis was conducted in full compliance with the regulations of Universiti Malaysia Sarawak (UNIMAS). Except where proper acknowledgment is given, this work is solely the effort of the author. This thesis has not been accepted for the award of any other degree and is not being **concurrently** submitted for any other academic qualification.

Signature _____

Student Name: Danielson Ngo Joseph

Matric No: 23020173

Date: 6 November 2025

Faculty of Resource Science and Technology
Universiti Malaysia Sarawak (UNIMAS)

ACKNOWLEDGMENT

First and foremost, I would like to thank God for His faithfulness and anointing as I navigate through my research journey. It is through His wisdom that I am able to navigate my thoughts and emotions as I push through the ups and downs of academia.

I am incredibly thankful to my supervisor, AP Dr. Devagi a/p Kanakaraju, for the mentorship guidance, patience and opportunities given throughout my Postgraduate studies. Her wisdom, encouragement and leadership have left a lasting impression on me, both personally and professionally. It has truly been a privilege to be under her guidance.

Additionally, I would like to also acknowledge the efforts of Madam Dyg Fatimawati Bt. Awg Alli, Mr. Wahap Bin Marni, and Mr. Shahfri Bin Semawi for their guidance in instrumentation analysis of SEM-EDX. I would also like to thank Dr. Lim Ying Chin from UiTM Shah Alam for her assistance with XRD and UV-DRS analysis and for contributing her knowledge to my studies. Moreover, I would also like to extend my thanks to Dr Khairul Anwar bin Mohamad Said for sharing his knowledge and guiding me in the final phases of my research.

To my parents, Joseph Piree and Samang Uyo and my sister, Esther Layu Joseph, your love, support and sacrifices have paved the way for me to pursue academia despite the hardships. Lastly, to the love of my life, Stephanie Arleen Apoi, you are the strong foundation that has been the voice of reason, empathy, and kindness as I battle my inner struggles in academia.

Finally, I would like to tell 21 year-old me who never thought academia would be achievable when I decided to change the whole trajectory of my field of study in 2020. We've come a long way.

POME-derived Ag/TiO_2-based photocatalyst for oxytetracycline degradation under visible light and membrane integration

ABSTRACT

The rise of emerging pollutants demands efficient and sustainable water treatment technologies. Ag/TiO_2-driven photocatalysis is a viable solution due to its durable visible-light activity and antimicrobial properties, yet stability, recovery, and overall synthesis sustainability remain major challenges that hinder its practical application. Therefore, the need to develop a green, durable, and easily recoverable Ag/TiO_2-based photocatalyst is crucial to advance photocatalysis as an eco-friendly solution for the treatment of complex pollutants. To overcome these drawbacks, this study explored the green synthesis of Ag/TiO_2-based ternary nanocomposites using palm oil mill effluent (POME) as a natural reducing and stabilizing agent. Two ternary photocatalysts, Ag/Bi_2MoO_6/TiO_2 (ABMOT) and Ag/g-C_3N_4/TiO_2 (AGCNT), were synthesized via a microwave-assisted method and extensively characterized by Fourier Transform Infrared Spectroscopy (FTIR), X-ray Diffractometry (XRD), Scanning Electron Microscopy with Energy-Dispersive X-ray (SEM-EDX), and UV-Visible Diffuse Reflectance Spectroscopy (UV-Vis DRS). Their photocatalytic activities were evaluated against oxytetracycline hydrochloride (OTC). Under visible-light irradiation, ABMOT achieved 97.2% OTC degradation at an optimal dosage of 0.6 g/L, while AGCNT reached 81.3% under the same conditions. ABMOT demonstrated stronger dark-adsorption capacity and greater tolerance to increasing pollutant concentrations than AGCNT, indicating better surface affinity and active-site accessibility. Regardless, both nanocomposites showed good stability over four consecutive recycling cycles, indicating superior stability and reusability potential. Additionally, both nanocomposites further demonstrated antibacterial activity against *Escherichia coli* and *Staphylococcus aureus*, confirming their multifunctional potential. To address the limitation of powder recovery in slurry photocatalysis, both nanocomposites were immobilized in polyacrylonitrile (PAN) membranes via the phase-inversion method. Structural and surface analyses confirmed successful integration, with nanocomposite-loaded membranes exhibiting enhanced hydrophilicity and porosity. Permeation studies revealed that AGCNT@PAN (2 wt%) achieved the highest pure water flux (170.94 $L \cdot m^{-2} \cdot h^{-1}$) and rejection rate (90.34%) compared to bare PAN membranes with 149.51 $L \cdot m^{-2} \cdot h^{-1}$ pure water flux and 44.88 % rejection rate. Consequently, ABMOT@PAN also showed improvements. Overall, this study demonstrates a novel, eco-friendly approach for synthesizing multifunctional photocatalysts by valorizing agro-industrial waste. These findings provide valuable insights into advancing green nanotechnology for sustainable water treatment applications.

Keywords: Palm oil mill effluent, green synthesis, titanium dioxide, silver, photocatalysis, antibacterial, membrane.

Fotopemangkin berasaskan Ag/TiO_2 daripada POME untuk degradasi oksitetrasiklin di bawah cahaya nampak dan integrasi dalam membran

ABSTRAK

Peningkatan bahan cemar muncul yang semakin membimbangkan memerlukan teknologi rawatan air yang cekap dan lestari. Fotopemangkinan yang berasaskan Ag/TiO_2 berpotensi menjadi salah satu kaedah untuk mengatasi isu ini kerana keupayaannya untuk diaktifkan di bawah cahaya nampak serta sifat antibakterianya. Namun demikian, aplikasi fotopemangkin berasaskan-Ag/TiO_2 masih terhad disebabkan oleh isu kestabilan, kesukaran untuk perolehan semula dan cabaran dalam kaedah sintesis yang lestari. Oleh itu, terdapat keperluan untuk membangunkan fotopemangkin berasaskan-Ag/TiO_2 yang hijau, lestari dan mudah untuk diperoleh semula agar teknologi fotopemangkinan dapat dikembangkan sebagai solusi mampan untuk rawatan air serta degradasi bahan cemar muncul. Kajian ini meneroka sintesis hijau nanokomposit pertigaan berasaskan Ag/TiO_2 dengan menggunakan efluen kilang kelapa sawit (POME) sebagai agen penurun dan penstabil semula jadi. Dua fotopemangkin pertigaan iaitu, Ag/Bi_2MoO_6/TiO_2 (ABMOT) dan Ag/g-C_3N_4/TiO_2 (AGCNT), disintesis melalui kaedah mikrogelombang dan dicirikan menggunakan FTIR, XRD, SEM-EDX dan UV-Vis DRS. Ujian terhadap oksitetrasiklin hidroklorida (OTC) menunjukkan ABMOT dapat mencapai degradasi sebanyak 97.2% dengan dos optimum 0.6 g/L, manakala AGCNT mencatatkan 81.3% di bawah cahaya tampak. Selain itu, kapasiti penjerapan dalam keadaan gelap untuk ABMOT lebih tinggi jika dibandingkan dengan AGCNT. Ini menunjukan bahawa ABMOT mempunyai toleransi yang lebih tinggi untuk kepekatan bahan cemar yang lebih tinggi kerana afiniti permukaan yang lebih sesuai terhadap oksitetrasiklin. Walau bagaimanapu, kedua-dua nanokomposit menunjukkan kestabilan yang baik untuk empat kitaran degradasi secara berterusan yang menjadi penanda aras kepada keupayaan pengitaran semula. Kedua-dua nanokomposit turut menunjukkan keberkesanan antibakteria terhadap Escherichia coli dan Staphylococcus aureus. Bagi menangani kekangan pemulihan serbuk, nanokomposit telah dimuatkan ke dalam membran poliakrilonitril (PAN) melalui kaedah kensongsangan fasa. Membran yang tersekatgerak dengan nanokomposit menunjukkan peningkatan hidrofilisiti dan porositi, dengan AGCNT@PAN (2 wt%) mencapai fluks air tulen tertinggi (170.94 $L \cdot m^{-2} \cdot h^{-1}$) dan kadar penyingkiran sebanyak 90.34% berbanding dengan membran PAN tanpa pengubahsuaian yang hanya mempuntai fluks air tulen sebanyak 149.51 $L \cdot m^{-2} \cdot h^{-1}$ dan kadar penyingkiran sebayank 44.88%. Secara keseluruhan, kajian ini membuktikan pendekatan mesra alam dan baharu untuk menghasilkan fotopemangkin pelbagai fungsi melalui pemanfaatan sisa industriagro POME. Penemuan ini memberikan perspektif yang bermakna ke arah kemajuan nanoteknologi hijau bagi aplikasi rawatan air yang lestari.

Kata Kunci: *Efluen Kilang Kelapa Sawit (POME), sintesis hijau, titanium dioksida, argentum, fotopemangkinan, antibakteria, membran*

TABLE OF CONTENTS

LIST OF TABLES

LIST OF FIGURES

LIST OF APPENDICES

LIST OF ABBREVIATIONS

ABMOT	$Ag/Bi_2MoO_6/TiO_2$
AGCNT	$Ag/Bi_2MoO_6/TiO_2$
ATR	Attenuated Total Reflectance
DRS	Diffuse Reflectance Spectroscopy
EDC	Endocrine-Disrupting Chemical(s)
EDX	Energy Dispersive X-ray
FTIR	Fourier Transform Infrared Spectroscopy
GAE	Gallic Acid Equivalent
NCs	Nanocomposite(s)
NPs	Nanoparticle(s)
OTC	Oxytetracycline hydrochloride
PAN	Polyacrylonitrile
PBS	Phosphate Buffer Solution
POME	Palm Oil Mill Effluent
PPCPs	Pharmaceutical and Personal Care Products
PWF	Pure Water Flux
QE	Quercetin Equivalent
RR	Rejection Rate
SEM	Scanning Electron Microscopy
SPR	Surface Plasmon Resonance
TEM	Transmission Electron Microscopy
TPC	Total Phenolic Content
TFC	Total Flavonoid Content
UV-Vis	Ultraviolet-Visible
XRD	X-ray Diffractometry

CHAPTER 1:

INTRODUCTION

1.1 Background of Study

As population growth and industrialization continue to progress around the world, the inevitable fate of water contamination from the penetration of various emerging pollutant sources poses a threat to both human well-being and the environment. Among various emerging pollutants, pharmaceutical and personal care products (PPCPs) have been recognized as an environmental concern due to their persistence, bioaccumulation potential, and adverse effects on aquatic ecosystems and human health Hena et al. (2021). Despite lacking regulatory status, the European Union (EU) announced that at least 33 compounds were prioritized for removal over the next 2 decades (Arumugam et al., 2025). Some of the compounds that were listed include anti-inflammatory drugs (e.g. ibuprofen, diclofenac) and antibiotics (Kumar et al., 2023). These compounds are well known to be endocrine-disrupting chemicals (EDCs) or carcinogenic. Although they are typically found in trace amounts (~0.1 ng/L to 200 ng/L), the concentrations of these compounds have been increasing in recent years, raising concerns about potential environmental risks (Hena et al., 2021; Kanakaraju et al., 2025; Ślósarczyk et al., 2021).

Despite the existence of conventional technologies in wastewater treatment, such as coagulation, flocculation and biological methods, they are limited in their ability to completely remove decontamination of the said emerging pollutants, including persistent organic/inorganic pollutants, and heavy metals (Ahmed & Haider, 2018; Anvari et al., 2021; Della Rocca et al., 2021). Generally, these processes end up producing secondary pollutants, which require further processing (Kweinor Tetteh & Rathilal, 2021). Therefore, there is a need to develop advanced wastewater treatment methods that efficiently purify contaminated water in a more sustainable way.

Advanced oxidation processes (AOPs) have emerged as effective wastewater treatment technologies for removing persistent, non-biodegradable organic pollutants. AOPs

operate by generating highly reactive oxygen species (ROS), particularly hydroxyl radicals ($HO\bullet$), which have a strong oxidation potential (~2.8 eV) and can degrade a wide range of organic contaminants into simpler and less harmful compounds (Kumari & Kumar, 2023). Unlike conventional treatment methods, AOPs can mineralize recalcitrant pollutants rather than merely transferring them from one phase to another. Common AOPs used for the degradation of organic contaminants include ozonation, Fenton and photo-Fenton processes, electrochemical oxidation, and photocatalysis, the latter of which has gained increasing attention due to its operational simplicity and environmental compatibility.

In recent years, advances in nanotechnology have highlighted the use of AOPs as a promising tool for wastewater treatment across various settings (Kweinor Tetteh & Rathilal, 2021). Photocatalysis has been extensively studied for water treatment because it uses semiconductor materials and light energy to drive redox reactions. In a typical photocatalytic process, irradiation with light energy equal to or greater than the semiconductor's band gap excites electrons from the valence band (VB) to the conduction band (CB), generating electron–hole pairs. The photogenerated holes oxidize water or hydroxide ions to form hydroxyl radicals ($HO\bullet$), while the excited electrons reduce dissolved oxygen to generate superoxide radicals ($O_2\bullet$) These reactive species play a crucial role in the degradation and mineralization of organic pollutants in aqueous systems.

Among numerous nano-based materials, titanium dioxide (TiO_2) is widely applied as a nanocatalyst in the wastewater treatment method known as photocatalysis (Celebi et al., 2021; Dahl et al., 2014). This is primarily due to TiO_2 being non-toxic, chemically stable, and possessing efficient charge separation, which contributes to its high photocatalytic activity (Zoubi et al., 2021). However, pristine TiO_2 has some drawbacks due to its high bandgap, which leads to rapid recombination of photogenerated electron-hole pairs. This limits the photocatalytic effectiveness of TiO_2, as its photoexcitation is primarily confined to the ultraviolet (UV) spectrum, with minimal functionalization in the visible light region (Lin et al., 2006). Therefore, extensive research has been conducted to address the limitations of pristine TiO_2 by incorporating dopants (e.g. metals and non-metal elements) or co-catalysts (e.g. perovskites, semiconductors, etc.) in the fabrication process (Zhang et al., 2021).

Past researchers have successfully fabricated TiO_2 with plasmonic metals like gold (Au) and silver (Ag) using various methods including sol-gel, photoreduction and solvothermal (Wang et al., 2019; Wu et al., 2021; Yang et al., 2022). These materials can

enhance the photocatalytic performance of TiO_2, as plasmonic metals cause photoexcitation of the binary composite under visible light through surface plasmon resonance (SPR). Perovskite-based catalysts, such as bismuth (Bi)-based photocatalysts, on the other hand, can align the Fermi energy levels of the binary due to its narrow bandgap with a wide range of light absorption (Arif et al., 2021). Given its lower energy bandgap (E_g = 2.5 eV – 2.9 eV) in comparison to TiO_2, Bi-based perovskite, such as bismuth molybdate (Bi_2MoO_6), has suitable band structures to form heterojunctions which minimize electron-hole recombination, improve charge separation efficiency, and combine the favorable traits of the two photocatalysts (Belousov et al., 2024). Additionally, the incorporation of graphitic carbon nitride (g-C_3N_4) has also been widely studied. g-C_3N_4 is advantageous for its ability to harness visible light and for its suitable energy bandgap (E_g = 2.7 eV), which enables it to form heterojunctions with TiO_2, substantially boosting the collective photocatalytic performance of g-C_3N_4/TiO_2 heterojunction systems (Nemiwal et al., 2021).

Incorporation of g-C_3N_4 and Bi_2MoO_6 in the fabrication of Ag/TiO_2-based ternary composites has shown potential for the treatment of different pollutants (Ranjithkumar et al., 2023; Yin et al., 2021). However, there remains a need for a greener, simpler fabrication process to enhance photocatalytic performance under visible light. In most studies, the fabrication process uses harsh solvents (Aravind et al., 2021). Hence, the possibility of utilizing plant extracts, microorganisms, or agricultural waste via green synthesis can be performed to mediate the fabrication of ternary heterostructures of Ag/Bi_2MoO_6/TiO_2 and Ag/g-C_3N_4/TiO_2, providing a greener and more benign synthesis alternative.

The palm oil industry is among the largest in tropical regions such as Southeast Asia and Africa. Generally, about 10% of palm produce generates oil, and the other 90% ends up as vegetative waste such as empty fruit bunches, palm press fibers, palm kernel shells, and palm oil mill effluent (POME) (Ofori-Boateng & Lee, 2013). These wastes contain an abundance of phytochemicals such as carotenoids, phenolics, sterols, flavonoids and tocopherols, which have been previously studied and applied for the synthesis of various nanomaterials (Gan et al., 2012; Lucas-Gómez et al., 2020; Pradhan et al., 2022; Shankar & Rhim, 2016; Sowani et al., 2016). While the high organic content in POME could pose a threat to the environment, these unutilized compounds could also be a promising resource in the green synthesis of nanomaterials.

While conventional Ag/TiO_2-based NCs exhibit promising photocatalytic activity, their synthesis often relies on chemical reducing agents and surfactants that may introduce

surface defects, residual toxicity, or poor interfacial stability (Bhardwaj & Singh, 2021). In contrast, POME contains naturally occurring phenolic compounds, flavonoids, and organic acids that can act as mild reducing agents, capping agents, and stabilizers during nanocomposite formation (Imam et al., 2025). These biomolecules promote controlled nucleation, improved particle dispersion, and enhanced interfacial contact between composite components. As a result, POME-derived nanocomposites are expected to exhibit comparable or improved photocatalytic and antibacterial performance while offering a greener, more sustainable synthesis route and improved surface functionality for pollutant interaction.

1.2 Problem Statements

Previous studies have successfully demonstrated the green synthesis of Ag nanoparticles (NPs) (AgNPs) and gold nanoparticles (AuNPs) by utilizing POME as a reducing and stabilizing agent (Aliero et al., 2024; Gan et al., 2012). While these works have greatly contributed to the advancement of POME-derived nanomaterials, they largely focus on individual NPs. The fabrication of more complex ternary NCs requires more nuanced methods, especially when using an unconventional green source such as POME. Despite growing interest in sustainable synthesis routes, few studies explore the formation of ternary nanocomposites using POME as a key component. Furthermore, no comprehensive studies have investigated the photocatalytic and functional performance of POME-derived ternary systems.

Another drawback that needs to be addressed in the application of NCs in photocatalytic treatment is the difficulty of separating their powder post-treatment. One way to overcome this drawback is to immobilize the NC on materials that are easily removed or replaced, which has recently attracted research interest in integrating photocatalytic NCs with polymeric membranes (Elrasheedy et al., 2019). Amongst various membranes, polyacrylonitrile (PAN) is a well-known commercial polymer with good solubility in organic solvents, unique chemical and thermal properties, radiation stability, and low cost. However, PAN-based membranes also have disadvantages, including low chemical stability, fouling, and hydrophobicity. To enhance its properties and address its shortcomings, PAN can be modified with nanomaterials.

Therefore, this study aims to use POME extracts in the green fabrication of ternary Ag/TiO_2-based NCs, namely Ag/Bi_2MoO_6/TiO_2 and Ag/g-C_3N_4/TiO_2, and assess their effectiveness and functionality as visible-light-driven photocatalysts for degrading oxytetracycline hydrochloride (OTC), a model emerging pollutant. OTC has been chosen as the model pollutant owing to its widespread use as a veterinary and human antibiotic, especially in aquaculture. Furthermore, this study emphasizes incorporating POME-derived NCs into PAN membranes via the phase-inversion method. To develop a multifunctional membrane-photocatalyst system for potential wastewater treatment applications, a performance comparison with a powder-based photocatalytic system was also presented.

1.3 Research Hypothesis

This study hypothesizes that Ag/TiO_2-based ternary NCs synthesized using POME as a green reducing and stabilizing agent will exhibit enhanced physicochemical properties, visible-light photocatalytic activity, and antibacterial performance compared to conventionally synthesized counterparts. It is further hypothesized that immobilizing these NCs into polyacrylonitrile (PAN) membranes will improve material recovery and filtration performance without significantly compromising their functional properties.

1.4 Research Question

With respect to the aforementioned criteria, several research questions were raised:

i. How does the use of POME extracts influence the morphology, crystallinity and chemical composition of Ag/Bi_2MoO_6/TiO_2 and Ag/g-C_3N_4/TiO_2 NCs?
ii. How effective are the POME-derived ternary NCs against OTC?
iii. How effective are POME-derived ternary NCs against gram-positive and gram-negative bacteria?
iv. What are the effects of incorporating POME-derived NCs into PAN membranes on the permeability, separation efficiency and physicochemical properties?
v. Does the use of POME as a green synthesis agent present a viable alternative to chemical synthesis routes in terms of environmental and functional performance?

1.5 Research Objectives

Hence, the objectives of this study were:

i. To synthesize ternary Ag/Bi_2MoO_6/TiO_2 and Ag/g-C_3N_4/TiO_2 NCs using POME extracts as a green reducing and stabilizing agent, and characterize their physicochemical and structural properties.
ii. To evaluate the photocatalytic performance of the synthesized ternary NC in degrading OTC under visible light,
iii. To assess the antibacterial activity of the synthesized ternary NCs against gram-positive (*E. coli*) and gram-negative (*S. aureus*) bacteria,
iv. To fabricate PAN membranes embedded with POME-derived ternary NCs via the phase inversion method and determine their permeability and separation efficiency,
v. To compare the removal efficiency of bare ternary NC powders with membrane-integrated systems for the removal of OTC.

1.6 Significance of Study

This study successfully demonstrated a green and sustainable approach in synthesizing ternary Ag/TiO_2-based NCs using POME, which is an underutilized agro-industrial waste. By extending the application of POME beyond the synthesis of singular NPs to the fabrication of more complex heterostructure NC systems, this research contributed to the development of an eco-friendly photocatalyst with good functionality under visible light. In addition to evaluating the potential of POME-derived NCs in powder form, this research explored their incorporation into PAN membranes via the phase inversion method. Although the membrane systems were not applied under photocatalytic conditions, their basic filtration performance was evaluated to gain insight into how NC loading influences membrane properties, providing a basis for understanding the effectiveness of incorporating ternary NCs into membrane systems. The outcomes of this study provided useful insights into the viability of using POME as a green route for synthesizing ternary photocatalysts and the potential of integrating ternary NCs into filtration membranes for future multifunctional water treatment applications. This work supports the advancement of sustainable materials and highlights a pathway for the valorization of agro-industrial waste into high-value components in material science and environmental remediation technologies.

1.7 Research Hypothesis

This study focuses on the green synthesis of Ag/TiO_2-based ternary NCs using POME as a natural reducing and stabilizing agent. Two photocatalysts, Ag/Bi_2MoO_6/TiO_2 and Ag/g-C_3N_4/TiO_2, were synthesized via a microwave-assisted method and characterized for their physicochemical, structural, and optical properties using FTIR, XRD, SEM-EDX, and UV-Vis DRS.

The photocatalytic performance of the synthesized NCs was evaluated under visible-light irradiation for the degradation of OTC as a model emerging pollutant. The effects of catalyst dosage, initial pollutant concentration, and reusability were investigated. Antibacterial activity against gram-negative (*E. coli*) and gram-positive (*S. aureus*) bacteria was also assessed.

To address limitations in catalyst recovery, the synthesized NCs were incorporated into PAN membranes via the phase-inversion method. The membrane study was limited to evaluating morphology, permeability, and rejection performance under filtration conditions. Photocatalytic membrane operation, large-scale application, and by-product toxicity analysis are beyond the scope of this study.

CHAPTER 2:

LITERATURE REVIEW

2.1 Advanced oxidation processes

Advanced oxidation processes (AOPs) are powerful chemical treatment technologies that emerged to remediate water, as they can remove a wide range of pollutants without producing secondary pollutants. This advantage addressed the limitations of conventional physicochemical and biological processes, which are further constrained by stringent environmental legislation (Liu et al., 2021). The first mentions of AOPs can be traced back to 1987 for the degradation of organic and non-biodegradable pollutants via the generation of hydroxyl radicals ($HO\bullet$) in place of oxidation with reagents such as potassium permanganate, potassium dichromate and sodium persulfate (Khan et al., 2020). This was because oxidation of pollutants with these reagents only produced partially oxidized intermediates that served as a secondary source of pollution. Instead, the generations of radicals led to the complete mineralization of pollutants into simpler products, such as carbon dioxide and water. Hence, in recent years, various AOPs have been introduced, including Fenton-based, ozone-based, and photocatalytic-based AOPs. In general, all these processes follow the same fundamental steps in which they produce either one or more species of ROS, such as $HO\bullet$ radical, superoxide radicals ($O_2\bullet$), peroxyl radical ($RO_2\bullet$), and so forth (Kumari & Kumar, 2023).

2.1.1 Photocatalysis

Among AOPs, photocatalysis has attracted considerable attention as an effective and sustainable water treatment technology. In recent years, there has been increased research interest due to its ability to generate ROS in situ (mainly ⬚ and ⬚), while operating under relatively mild conditions compared with other conventional AOPs such as Fenton and ozone-based systems (Arifin et al., 2023). Fenton and ozone-based systems generally require strict pH control, continuous chemical input, and complex operational setups. In

photocatalytic systems, semiconductor materials are often employed to absorb photons with energy that is either equal to or greater than the energy band gap, E_g. This results in the excitation of electrons from the valence band (VB) to the conduction band (CB), forming electron-hole pairs (Abey et al., 2025). These charge carriers subsequently participate in surface redox reactions, thereby producing ROS. The combination of operational simplicity, the catalyst's reusability (due to the heterogeneous nature of the process), and the potential for complete mineralization has positioned photocatalysis as a promising and versatile AOP for the removal of persistent and emerging pollutants.

2.1.2 Photocatalytic reaction mechanism

Following the general principles of photocatalysis, the fundamentals of photocatalytic reaction mechanisms in water treatment involve a sequence of steps. The first step often involves charge generation, followed by transport and finally, the interfacial redox reactions of the photogenerated charge carriers on the surface of the catalyst (Chakravorty & Roy, 2024). The final step governs pollutant degradation reactions. Upon irradiation with incident photons, a semiconductor photocatalyst absorbs energy. This promotes electrons from the VB to the CB, resulting in the formation of electron-hole pairs. These charge carriers may undergo recombination or migrate to other catalyst surface, where they participate in simultaneous oxidation and reduction reactions. The photogenerated holes (h^+) can oxidize surface-adsorbed water molecules and hydroxide ions to form $HO\bullet$ radicals while excited electrons (e^-) reduce dissolved oxygen to generate $O_2\bullet$ radicals. The ROS subsequently attacks organic pollutant molecules through a series of complex reactions, which ultimately end in the mineralization of these complex pollutants to harmless by-products such as CO_2, H_2O, and inorganic ions. However, photocatalytic efficiency is strongly influenced by critical factors such as recombination rate, light absorption capacities, overall surface areas, and the availability of reactive sites on the photocatalyst surface (Bekele & Alamnie, 2025).

2.1.3 Application of photocatalyst in wastewater treatment

Metal oxide-based semiconductors are the most extensively investigated class of photocatalysts for wastewater treatment due to their chemical stability, ease of synthesis, and strong redox capability. The most widely studied metal oxides include zinc oxide (ZnO),

tungsten trioxide (WO_3), iron oxide (Fe_2O_3), and titanium dioxide (TiO_2), each exhibiting distinct band structures and photocatalytic behaviors, producing different treatment outcomes.

ZnO has been reported to exhibit photocatalytic activity comparable to that of TiO_2 under UV irradiation. For example, ZnO yielded degradation efficiencies of 99% for Tartrazine (TRZ), and 98% for naproxen (NAP) after 120 minutes of exposure under UV (Balu et al., 2019; Mohamed et al., 2023). However, its practical application is often limited by photocorrosion and dissolution. Another candidate photocatalyst, WO_3, has a narrower band gap (approximately 2.4 eV) and therefore exhibits strong visible-light-driven activity. For instance, Manganese and Copper (Mn-Cu) doped WO_3 nanostructures achieved 86.7% degradation of methylene blue (MB) within 175 minutes and 75.9% of levofloxacin (LVF) within 120 minutes under visible light (Rizvi et al., 2024). Similarly, Ag-doped WO_3 composites have shown enhanced performance in degrading chloramphenicol (CLP) (Truong et al., 2025). Fe_2O_3, despite being abundant and absorbing visible light, its efficiency is often limited by rapid charge carrier recombination, though it can be improved through heterojunction formation (Hitam & Jalil, 2020).

Among the afore-mentioned semiconductors, TiO_2 remains as the benchmark material due to its high chemical stability, non-toxic nature and resistance to photocorrosion. Modified TiO_2 systems, such as black TiO_2, have achieved 100% degradation of ciprofloxacin (CIP) under LED irradiation in 70 minutes (Samy et al., 2024). While TiO_2 primarily exhibits UV activity due to its wide band gap (3.2 eV), its consistent performance and environmental compatibility make it the reference material in research on heterogeneous photocatalytic wastewater remediation. A summary of various photocatalysts used for the degradation of organic pollutants is presented in Table 2.1.

Table 2–1: Summary of selected metal oxide-based photocatalysts for the removal of organic pollutants

Semiconductor	Dopant/Co-catalyst	Target Pollutant	Conditions	Removal Efficiency	Reference
TiO_2	Nitrogen	CIP	• Visible light • 70 minutes	100.0%	Samy et al. (2024)
WO_3	Mn-Cu	MB	• Visible light • 175 minutes • pH 11	86.7%	Rizvi et al. (2024)

WO_3	Ag	CLP	• Visible light • 120 minutes	~80.0%	Truong et al. (2025)
ZnO	g-C_3N_4/α-Fe_2O_3	TRZ	• Visible light • 120 minutes • pH 7 (Neutral)	99.34%	Balu et al. (2019)

ZnO	Pristine	NAP	• UV light • 120 minutes	98.7%	Mohamed et al. (2023)
Fe_2O_3	Carbon quantum dots	MB	• Visible light (Xenon) • 180 minutes	~90%	Hitam and Jalil (2020)

2.2 Titanium dioxide, TiO_2 as a photocatalyst

The adaptation of TiO_2 as a photocatalyst has been widely studied ever since the discovery of its water-splitting abilities under the irradiation of UV light by Fujishima and Honda (1972). Following this revelation, a study by Frank and Bard (1977) paved the way for the incorporation of TiO_2 in the photocatalytic oxidation of aqueous sulphite and cyanide ions. This study was one of the earliest mentions of the application of TiO_2 in water purification technology. Subsequently, further studies on the properties and mechanism of TiO_2 single crystals were established by Wang et al. (1999), which paved the path for numerous other studies with a variety of applications in photocatalysis. To date, various studies on the application of TiO_2 photocatalyst have been established, such as its application in water purification, cancer therapy, green energy generation, energy storage and so forth (Çeşmeli & Biray Avci, 2019; Demir et al., 2019; R. Li et al., 2020; Singh et al., 2020). The versatility of TiO_2 in the aforementioned areas is attributed to the properties of TiO_2 being environmentally friendly, non-toxic, non-corrosive, highly stable, cost-effective and reusable (Qamar et al., 2023).

2.2.1 Crystalline properties of TiO_2

There are three main polymorphs ascribed to TiO_2, which are anatase, rutile and brookite. These crystalline phases of TiO_2 are widely available in nature and are caused by the distortion of the TiO_2 octahedral forms (Eddy et al., 2023). Based on Figure 2.1, rutile and brookite phase octahedrons exhibit a slight orthorhombic distortion, whereas in anatase, a more significant distortion is observed, making anatase less symmetrical than the other two variations (Chen & Mao, 2007). The Ti−Ti distances in anatase are larger, whereas the Ti−O distances are shorter than those in rutile. In the rutile structure, each octahedron is in contact with 10 neighbor octahedrons (two sharing edge oxygen pairs and eight sharing corner oxygen atoms), while in the anatase structure, each octahedron is in contact with eight neighbors (four sharing an edge and four sharing a corner). Differences in lattice structures

lead to distinct mass densities and electron band structures of the TiO_2 polymorphs (Janczarek et al., 2022).

Figure 2–1: The three crystal structures of TiO_2 polymorphs Adapted [reprinted] from Haggerty et al. (2017).

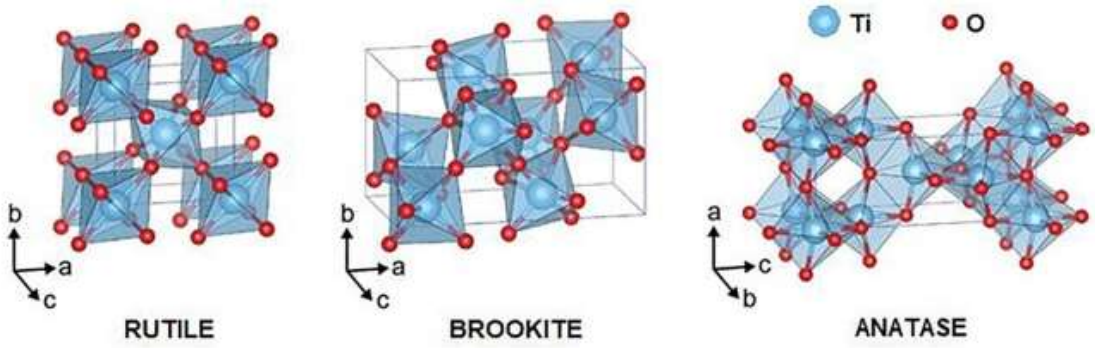

Nevertheless, in photocatalytic water-splitting applications, the rutile and anatase polymorphs of TiO_2 are the most extensively studied, as they exhibit greater photoactivity compared to the brookite phase (Eddy et al., 2023). The difference in their photocatalytic activity is mainly attributed to the difference in their band structure, mass density, and the effective mass of the photogenerated charge carriers (Zhang et al., 2014). Despite the rutile phase having a lower energy bandgap (3.0 eV) than the anatase phase (3.2 eV), past studies have shown that anatase has a smaller effective mass and a longer lifetime of photogenerated electron-hole (Luttrell et al., 2014; Yamakata & Vequizo, 2019; Žerjav et al., 2022). This is a result of having an indirect bandgap in comparison to the other two phases, which have a direct bandgap configuration. This leads to higher photocatalytic reduction activity of anatase TiO_2. Depending on the goal of its application, the various phases can be well-suited for a variety of photocatalytic reactions.

2.2.2 Application of TiO_2 in water purification

Given the versatility of the different phases of TiO_2 polymorphs in photocatalysis, the recent decade has witnessed an exponential increase in studies with regard to the water purification process (Armaković et al., 2023; Dharma et al., 2022; Magaña-López et al., 2021; Riaz & Park, 2020; Venkata Reddy et al., 2019; Wetchakun et al., 2019). Photocatalysis has emerged as a promising alternative to conventional approaches for removing pollutants from water, as pollutants can be transformed into non-toxic degradation products. Generally, the photocatalytic mechanism of TiO_2 begins with the generation of

electron-holes in the conduction band (e^-_{cb}) and the valence band (hv^+_{vb}), upon irradiation of UV light, as shown in Figure 2.2 (Chen et al., 2020). According to Paumo et al. (2021), the formation of electron-holes will result in the formation of radicals (hydroxyl radicals, $HO\bullet$ and superoxide radicals, $O_2\bullet$) through interactions with oxygen and water molecules that are absorbed onto the surface. These radicals will then react with the pollutants to degrade them into simpler and non-toxic byproducts such as carbon dioxide and water (Figure 2.2). The mechanisms involved in the TiO_2 photocatalysis are shown in the equations (Eq) below:

$$TiO_2 + hv_{UV} \rightarrow e^-_{cb} + h^+_{vb} \quad \text{(Eq 2.1)}$$

$$hv^+_{vb} + OH^-_{surface} \rightarrow HO\bullet \quad \text{(Eq 2.2)}$$

$$hv^+_{vb} + H_2O_{absorbed} \rightarrow HO\bullet + H^+ \quad \text{(Eq 2.3)}$$

$$e^-_{cb} + O_{absorbed} \rightarrow O_2\bullet \quad \text{(Eq 2.4)}$$

$$hv^+_{vb} + Organic \rightarrow Oxidation\ products \quad \text{(Eq 2.5)}$$

$$\bullet OH + Organic \rightarrow Degradation\ products \quad \text{(Eq 2.6)}$$

$$e^-_{cb} + Organic \rightarrow Reduction\ products \quad \text{(Eq 2.7)}$$

Figure 2–2: Schematic illustration of photocatalytic activity in the TiO_2 photocatalyst.

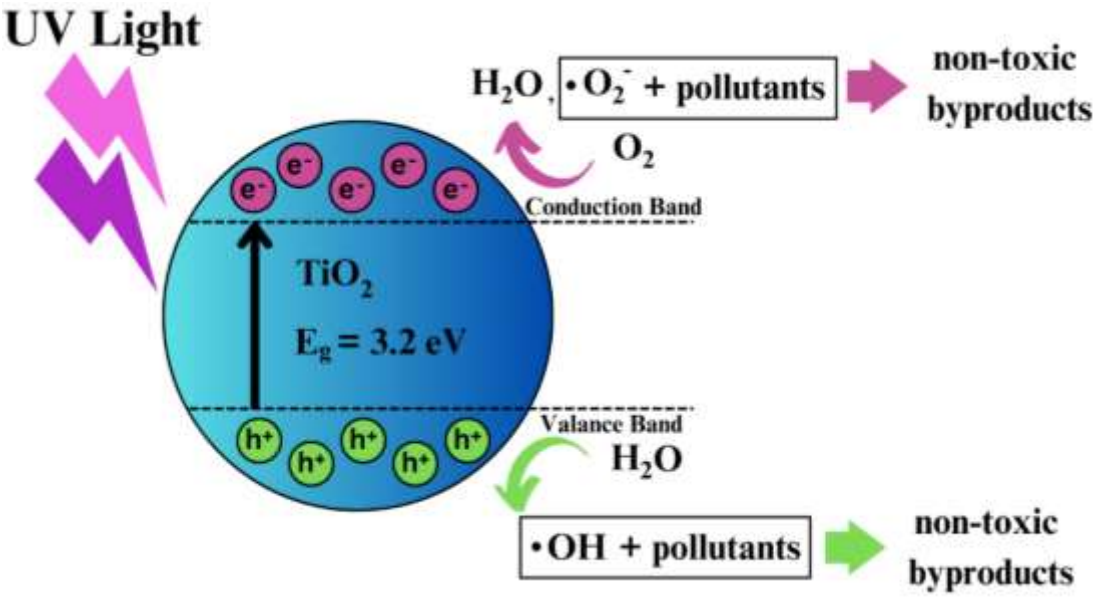

2.2.3 Drawbacks of TiO_2

Despite numerous desirable traits as a photocatalyst, the use of pure TiO_2 for light-induced water purification is hindered because its photocatalytic activity is limited to UV irradiation. Moreover, in most cases, TiO_2 used in photocatalytic water purification is in the nanoscale (Al-hamoud et al., 2022; Alkorbi et al., 2022; Ancy et al., 2022; Kim et al., 2021; Malakootian et al., 2020). For most nano-scaled semiconductors like TiO_2 NPs, the quantum size effect alters semiconductor properties due to the great difference in the size of the particle to the wavelength of the electron (Nunzi & De Angelis, 2022). The quantum size effect is simply the change in optical and electronic properties that is reflected in the energy levels, potential wells, valence bands, conduction bands, and electron energy bandgaps (Neikov & Yefimov, 2019) (Figure 2.3).

Figure 2–3: Quantum size effect on semiconductor materials of different sizes Adapted [reprinted] from Liu et al. (2022).

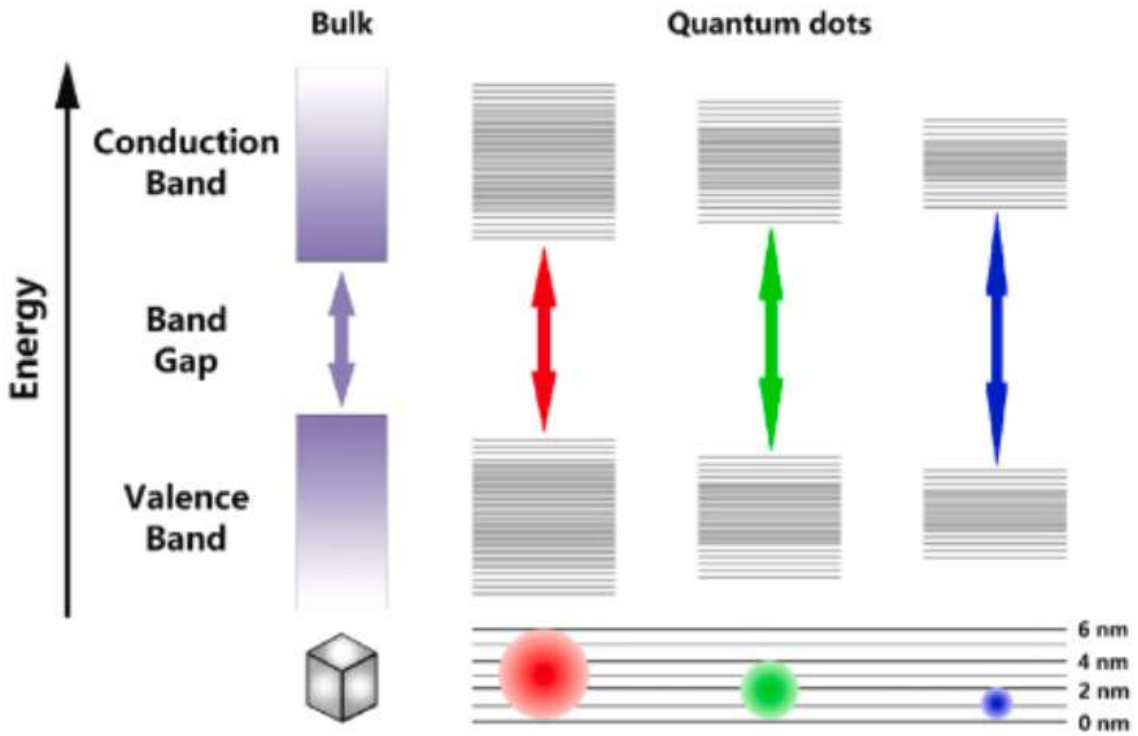

Bulk materials of semiconductor metals often exhibit a small bandgap due to defects that cause deep and shallow traps near the band edge of the electronic states (Lin et al., 2006). This is caused by the mild delocalization of molecular orbitals, which, in turn, results in a red shift in the absorbance spectrum (Lin et al., 2006). However, when the size of these

materials is within the nanoscale (<30 nm), quantum size effects have been reported to take place as electrons and holes in the quantum-sized semiconductors are spatially confined in a potential well, which in turn induces a blue shift in the absorbance spectrum (Lin et al., 2006). This phenomenon demonstrates that pure nano-TiO_2 exhibits strong UV absorbance due to the high-energy bands of both rutile and anatase phases, which are 3.0 eV and 3.2 eV, respectively. This absorbance is also dependent on the size of nano-TiO_2 particles. For instance, Jiménez Reinosa et al. (2016), found that as the size of TiO_2 decreases from the microscale to the nanoscale, the bandgap increases from 3.15 eV to 3.37 eV, resulting in a blue shift (391 nm to 357 nm) in the UV absorption edge. Another study by D. Li et al. (2020) also revealed that the absorbance edge of pure nano-TiO_2 with anatase crystallinity showed strong absorption within the UV region at 400 nm. These studies suggest that the particle size of TiO_2 influences the absorption edge; therefore, nano-TiO2 needs to be modified to enhance its photocatalytic ability, as UV accounts for only 5% of solar radiation.

2.3 Current strategies to improve TiO_2's photocatalytic performance

Various strategies have been developed to further improve the photocatalytic activity of TiO_2, with current trends toward the functionalization of TiO_2-based NCs for visible-light and near-infrared regions. This is because in the overall solar spectrum, visible light and infrared radiation account for at least 42% and 49% of the total incident rays, respectively (Bano et al., 2021). This can be achieved by the fabrication of TiO_2 with other materials such as metals, perovskites and carbon-nitride materials. Additionally, in recent years, researchers have shown growing interest in the recyclability, stability, and recovery of TiO_2-based NCs. Consequently, numerous studies have examined how different support materials influence stability. An illustration of the current strategies employed in modifying TiO_2-based NCs is shown in Figure 2.4.

Figure 2–4: Strategies employed to improve the functionalization and stability of TiO_2-based nanocomposites under a wider range of light irradiation.

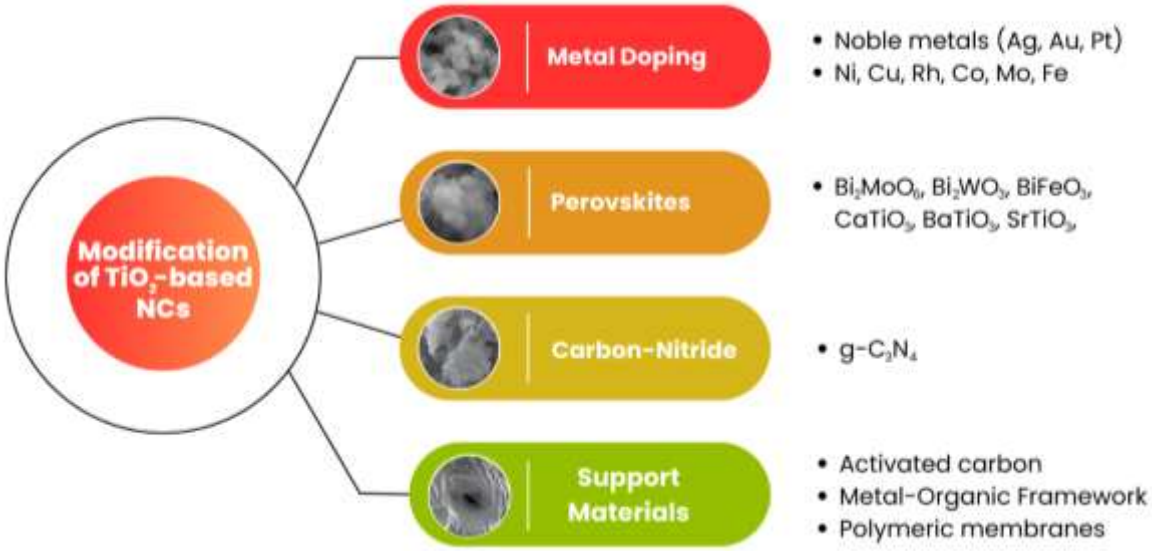

2.3.1 Metal Doping

In general, doping of TiO_2-based NCs has been done in two ways, namely with anionic non-metal elements (e.g. carbon, nitrogen, sulphur, fluorine) and cationic dopants (e.g. transition metals, noble metals, rare earth elements). Metal doping has been widely studied due to the ability of metal dopants to act as an electron trap to reduce electron-hole recombination, introduce new energy levels in the bandgap structure of TiO_2, induce SPR effects and create new gap states through their interaction with the VB states of TiO_2 (Kumaravel et al., 2019). Figure 2.5 presents a schematic illustration depicting the effects of metal doping on TiO_2-based NCs.

Figure 2–5: Schematic illustration of the photocatalytic mechanism involved in a metal-doped TiO_2 photocatalyst.

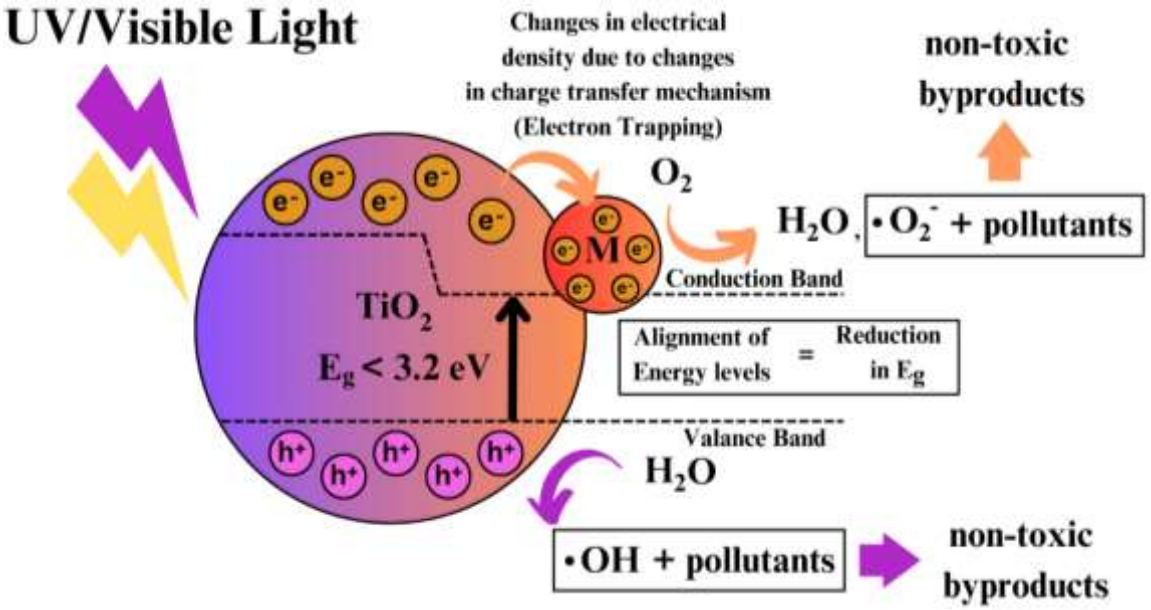

Amongst a myriad of metals explored for enhancing the photocatalytic ability of TiO_2, the most widely studied dopants namely Au, Ag, platinum (Pt), palladium (Pd), and copper (Cu). The addition of metal dopants is often aimed at enhancing and prolonging the lifetime of the charge carrier. Therefore, the selection of metal dopants is important as the photoactivity of TiO_2-based photocatalysts that are modified with metal dopants varies depending on how well the overall photocatalytic working system functions, despite the aforementioned enhancements on the photocatalyst. This is because the synergistic effects of metal dopants rely on whether it is an active or inactive dopant in the different crystalline phases of TiO_2.

Cu is a popular choice among metal dopants because it is abundant as an earth element, making it a highly cost-effective option. Albornoz Marin et al. (2022) synthesized core-shell Cu@TiO_2 through the wet impregnation technique as a means of introducing Cu^{2+} ions into the crystal lattice of TiO_2 for the degradation of phenol. The incorporation of Cu into TiO_2 resulted in a photocatalyst with reduced crystalline size, increased lattice strain and a decrease in the bandgap energy, E_g from 3.01 eV to 2.67 eV for 3.0% Cu. Although the degradation rate under UV irradiation was not particularly high, it doubled under visible light due to the reduced bandgap and the SPR effects of Cu. A similar finding was reported by Pascariu et al. (2022), where Cu/TiO_2 composite nanofibers with Cu-doped onto TiO_2, achieved nearly complete degradation of 25 ppm amaranth dye, reaching a degradation rate of 99.8% under both UV and visible light. Notably, the crystalline phase of TiO_2 differed

between the two studies whereby Albornoz Marin et al. (2022) used a mixed anatase/rutile phase TiO_2, while Pascariu et al. (2022) used a pure anatase phase TiO_2. The differences between these two studies highlight the importance of selecting an appropriate metal dopant, depending on the TiO2 crystalline phase, to achieve optimal photocatalytic degradation properties.

Apart from Cu, various studies on noble metal doping of TiO_2-based photocatalysts have been conducted. Noble metals such as Ag, Au, Pt and Pd have been shown to induce desirable traits in comparison to other metals due to the conductive properties of these metals. Nevertheless, the application of Au, Pt and Pd in modifying TiO_2-based photocatalysts is difficult as these elements are expensive and difficult to source out despite being superior to Ag as a dopant. However, Ag excels as a dopant compared to other noble metals. It has superior conductivity, can induce SPR effects similar to those of other metals, is significantly more abundant than the other noble metals, and is well known for its antibacterial properties (Raes et al., 2024). For instance, Gomes et al. (2018) studied the effects of Ag, Pd and Pt loading on the efficiency of TiO_2 for the photocatalytic ozonation of parabens. It was observed that at higher loading, Pd and Pt outperformed Ag in degrading parabens, whereas at lower concentrations, Ag exhibited superior photocatalytic activity. This study highlights the economic advantage of Ag compared to other noble metal dopants with photocatalytic enhancements of TiO_2 that are close to those of the others. However, it is also worth noting that maximizing the performance of Ag-doped TiO_2 photocatalytic materials requires selecting suitable TiO_2 crystalline phases, as Ag exhibits varying synergistic effects depending on whether it is incorporated into pure or mixed phases, as demonstrated in previous studies (Kusdianto et al., 2018).

2.3.2 Perovskites

In recent years, there has been an increase in the fabrication of TiO_2 with co-catalysts such as perovskites. Perovskites are considered as third-generation photocatalysts due to their unique physicochemical characteristics that include high chemical stability, high thermal stability and excellent electronic conductivity. The general chemical formula of perovskite is ABX_3 in which A, B and X sites stand for alkaline-earth/rare-earth cations with large atomic radii such as bismuth (Bi), transition metal cations such as molybdenum (Mo) with smaller atomic radii, and anions, namely, oxygen (O), sulphur (S), nitrogen (N), and

halides (Wang et al., 2021). The formation of perovskites happens when cations A form a 12-fold coordination at the centre of the cube of B cations that are combined with 6 anions X to form BX_6 coordination in an octahedral molecular geometry (Figure 2.6). The differences in the valences and atomic radii of these three components generate distortion in the structure that induces characteristics such as oxygen vacancies, active redox sites, narrow energy bandgap, visible light photocatalytic activity and superior electrical conductivity and thermal stability (Kong et al., 2019; Kumar et al., 2020).

Figure 2–6: An ideal ABX_3 structure of a cubic perovskite crystal Adapted [reprinted] from Kong et al. (2019).

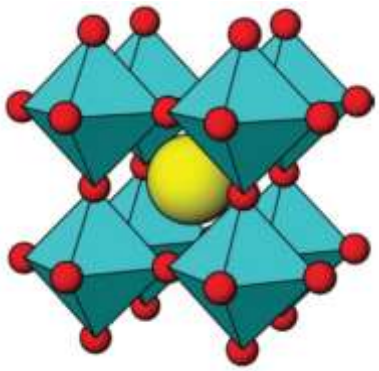

Some of the most common phases in the perovskite family that have been currently studied include the Dion-Jacobson phase, Ruddlesden-Popper phase and Aurivillius phase (Kubacka et al., 2012). However, amongst all the available phases in the perovskite families, the Aurivillius phase is considered the class that has been shown to have the most significant results in terms of its photocatalytic performance (Collu et al., 2022; Guo et al., 2019; Malik et al., 2021; Yao et al., 2024). Given the exceptional properties of perovskite materials as photocatalysts, recent years have seen the use of various perovskite types as co-catalysts to enhance TiO_2-based photocatalysts under visible light (Fatima et al., 2024).

A study by Liu et al. (2019) successfully fabricated Bi_2MoO_6/TiO_2 via a facile solvothermal-calcination method for the photodegradation of ciprofloxacin (Figure 2.7). A binary anatase/rutile TiO_2 with a rod-like shape, and with nano-plate-like Bi_2MoO_6 was produced. The photocatalyst also exhibited a reduced bandgap of ~2.60 eV, along with improved charge-carrier dynamics and reduced electron-hole recombination. The photocatalyst exhibited exceptional performance in degrading ciprofloxacin, achieving nearly 60.0% dark adsorption and close to 99.0% photodegradation under visible light.

Figure 2–7: Characterizations and photocatalytic performance of Bi_2MoO_6/TiO_2 Adapted [reprinted] from Liu et al. (2019).

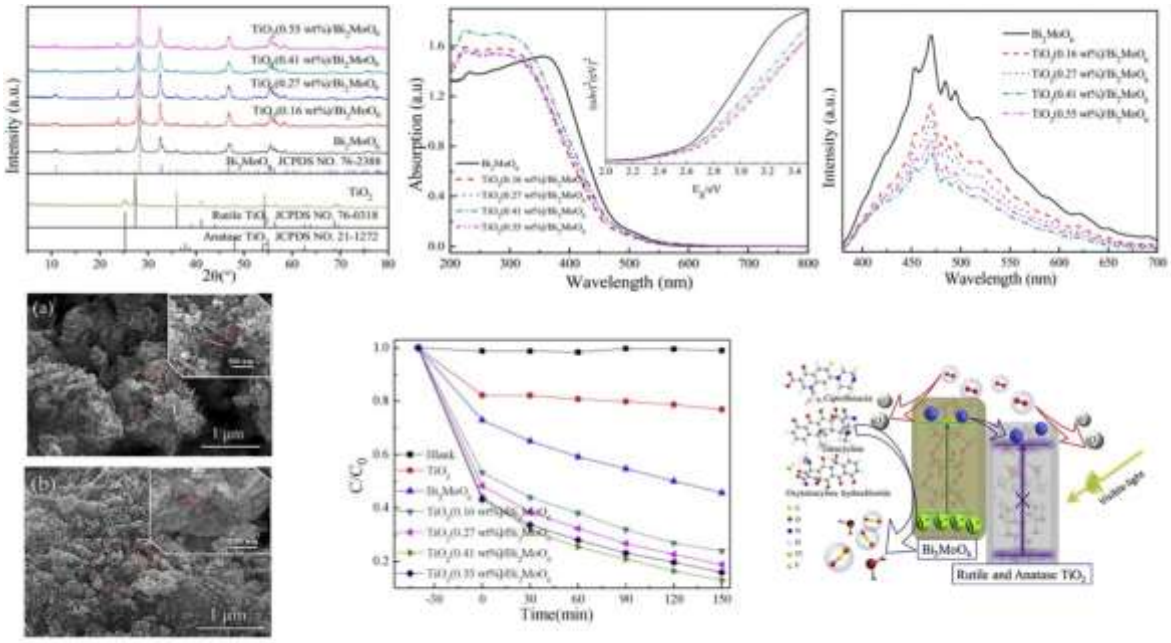

Furthermore, another study by Yin et al. (2021) fabricated Bi_2MoO_6/TiO_2 with Ag quantum dots (QDs) for the degradation of tetracycline hydrochloride using a multi-step solvothermal-wet impregnation method. In comparison to Liu et al. (2019), the morphology of the synthesized $AgQD/Bi_2MoO_6/TiO_2$ was controlled by using fluorine-doped tin oxide glass as a template for the synthesis of the photocatalyst. Their method produced single-phase TiO_2 rutile nanorods, a Bi_2MoO_6 nanosheet photocatalyst, and Ag QDs with sizes less than 1 nm. The ability of the $AgQD/Bi_2MoO_6/TiO_2$ to degrade tetracycline hydrochloride with an efficiency of 90.8% can be attributed to characteristics reported by Liu et al. (2019). These included a reduction in the energy bandgap, electron-hole recombination rate and enhanced charge separation dynamics with a longer lifetime (Figure 2.8).

Figure 2–8: Characterizations and photocatalytic performance of $AgQD/Bi_2MoO_6/TiO_2$ Adapted [reprinted] from Yin et al. (2021).

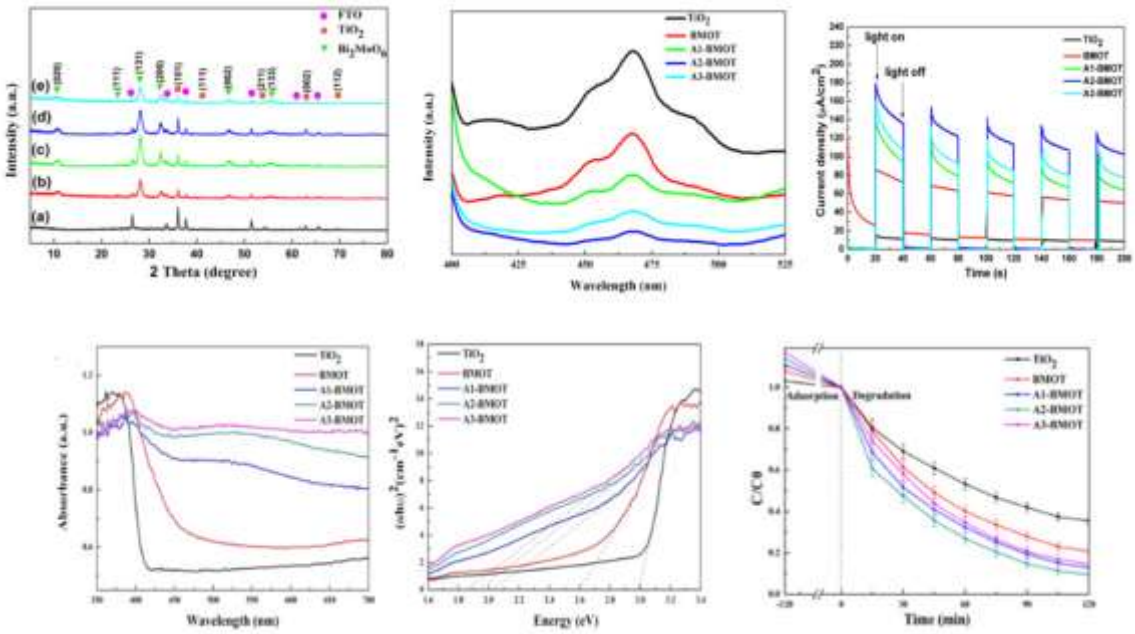

In summary, the ability of perovskite-based material such as Bi_2MoO_6 is shown to be able to reduce the energy bandgap of TiO_2 and further improve its charge dynamics as a result of the different bandgap structures. This shows the potential of fabricating TiO_2 with a perovskite co-catalyst to broaden and enhance the applications of TiO_2-based photocatalytic nanomaterials in water treatment.

2.3.3 Carbon Nitrides

Besides perovskite-based materials, co-catalyst, g-C_3N_4 is another widely studied candidate for the fabrication of TiO_2-based photocatalytic materials. Layered g-C_3N_4, as another conventional semiconductor, has two building blocks (triazine [C_3N_3] and tri-s-triazine/heptazine [C_6N_7]) rings, homogeneously distributed in the g-C_3N_4 microstructure. The most commonly used method for preparing bulk g-C_3N_4 is the thermal polymerization of nitrogen-rich organic precursors (including dicyandiamide, urea, and melamine) at relatively high temperatures (400–700 °C) (Zhang & Jiang, 2022). g-C_3N_4 is chemically and thermally stable (up to 600 °C in air) owing to the presence of aromatic C–N heterocycles in the material's structure, and it cannot be dissolved in organic or acid/alkali solvents under ambient conditions (Martin et al., 2014; Teixeira et al., 2018; Wang et al., 2021). Thus, g-C_3N_4 has been widely studied as a metal-free semiconducting photocatalyst

for a variety of applications over the past decades (Huang et al., 2019). Moreover, g-C_3N_4 and g-C_3N_4–based materials are considered to be chemically active only in the case of photogenerated charge pairs being consumed before the recombination takes place (Ong et al., 2016).

As one of the most stable carbon nitride allotropes, g-C_3N_4 has been extensively investigated in visible-light-driven photocatalysis-related fields. Despite its various advantageous properties, g-C_3N_4 is nevertheless still not an ideal photocatalyst. This is due to its irregular morphology (which attenuates charge transfer), low specific surface area (less than 20 m^2/g), and partially blocked reactive sites of the close-packed system (Huang et al., 2019; Ong et al., 2016).

Therefore, studies have been conducted to improve the performance of g-C_3N_4 by combining it with TiO_2, as smaller TiO2 particles can further increase the composite's total surface area. Given the narrow bandgap of g-C_3N_4 (~2.7 eV), the synergistic effects of the staggered band positions between TiO_2 and g-C_3N_4 can enable functionalization of g-C_3N_4/TiO_2 under visible light, with enhanced performance compared to their individual counterparts. For instance, a study by Kanakaraju et al. (2024) synthesized TiO_2/ZnS/g-C_3N_4 photocatalyst through a facile hydrothermal process. The study revealed that the photocatalyst showed enhanced photodegradation of multiple organic pollutants, with RhB having the highest degradation rate of 90%. The synthesized TiO_2/ZnS/g-C_3N_4 showed a remarkable ability to degrade mixed pollutants owing to the enhanced optoelectrical and structural properties of the photocatalyst. The fabrication of g-C_3N_4 also proved the ability of TiO_2 to increase the surface area of the overall composite which allows for better contact with pollutants, thus enhancing the performance of the overall composite. Other studies have also reported similar results (Gahlot et al., 2021; Kocijan et al., 2022; Monga & Basu, 2019; Sutar et al., 2020).

This shows the potential of fabricating Ag/TiO_2-based nanocomposite with g-C_3N_4 to further enhance its functionality under visible light. Combining the SPR effects of Ag and the narrow energy bandgap of g-C_3N_4 can result in a superior photocatalyst that complements each weakness of its singular components to form a high-performing Ag/g-C_3N_4/TiO_2 photocatalyst under a wider spectrum of light sources.

2.4 Fabrication of TiO_2 with Ag, Bi_2MoO_6 and g-C_3N_4

It has been proven that the fabrication of TiO_2 through metal doping or combination with co-catalysts such as perovskites and g-C_3N_4 has been shown to enhance the photocatalytic properties of TiO_2 as a photocatalyst. Noble metals such as Ag can be used for the modification of TiO_2-based photocatalysts. By depositing nano-Ag on the surface of TiO_2, the photocatalytic ability of TiO_2 can be enhanced as Ag would act as an electron trap or charge carrier due to the Schottky barrier between Ag and TiO_2 (Chakhtouna et al., 2021). This is possible as the Fermi energy level of Ag influences the charge separation between the interface of the TiO_2 and Ag dopant (Kanakaraju et al., 2022). Given that the Fermi energy level of Ag is located below that of TiO_2, this causes the bandgap of TiO_2 to decrease, hence improving charge separation and preventing electron-hole recombination in the TiO_2 crystal lattice.

Moreover, as previously mentioned, due to the excellent SPR of Ag, hot electrons upon excitation by UV or visible light are injected via the Schottky junction into the conduction band of TiO_2 (Ding et al., 2014). The hetero-interaction between TiO_2 and nano-Ag, serving as a co-catalyst in the overall mechanism, enhances the reactive sites of the Ag-TiO_2 photocatalyst, leading to improved charge separation and efficient electron transport between Ag and TiO_2 (Shoaib et al., 2016). This is mainly due to the excess negative charge in Ag and the excess positive charge in TiO_2 as a result of the Schottky barrier formed at the heterojunction of the Ag-TiO_2 surface. Additionally, fabrication with bismuth molybdate (Bi_2MoO_6) could provide additional benefits to the ternary structure of Ag/Bi_2MoO_6/TiO_2. Given that Bi_2MoO_6 have a narrow bandgap with a wide range of light absorption, this allows for an alignment of the Fermi energy levels of TiO_2, which thus enables the reduction of the energy bandgap of the overall ternary composites (Figure 2.9). This allows for a more efficient charge transfer mechanism as well as better visible light response of the photocatalyst.

Figure 2–9: Proposed photocatalytic degradation of tetracycline hydrochloride by $Ag/Bi_2MoO_6/TiO_2$ under visible light irradiation Adapted [reprinted] from Yin et al. (2021)

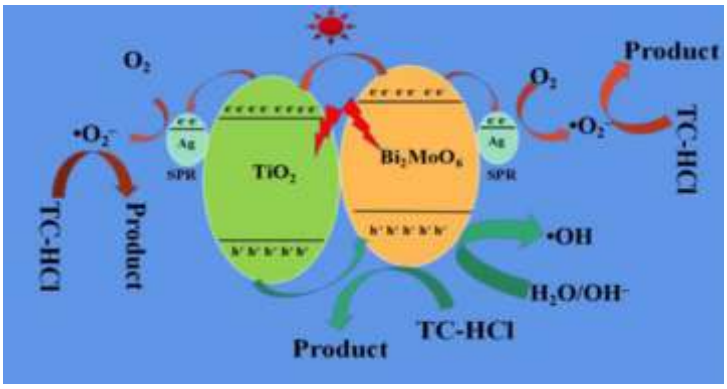

Similar to fabrication with Bi_2MoO_6, combining TiO_2 with g-C_3N_4 can also form an effective heterojunction, enabling improved charge transfer dynamics, introducing additional energy levels, and enhancing the visible light functionality of TiO_2 (Acharya & Parida, 2020) (Figure 2.10). Moreover, given that the downside of g-C_3N_4 is its low surface area, fabrication with TiO_2 could also result in a NC with a higher relative surface area which can allow for more contact with pollutants, thus enhancing adsorption capacity and increasing the number of active sites for photocatalysis to occur.

Figure 2–10: Proposed photocatalytic degradation of rhodamine B by $Ag/g\text{-}C_3N_4/TiO_2$ under visible light irradiation Adapted [reprinted] from Zhou et al. (2019).

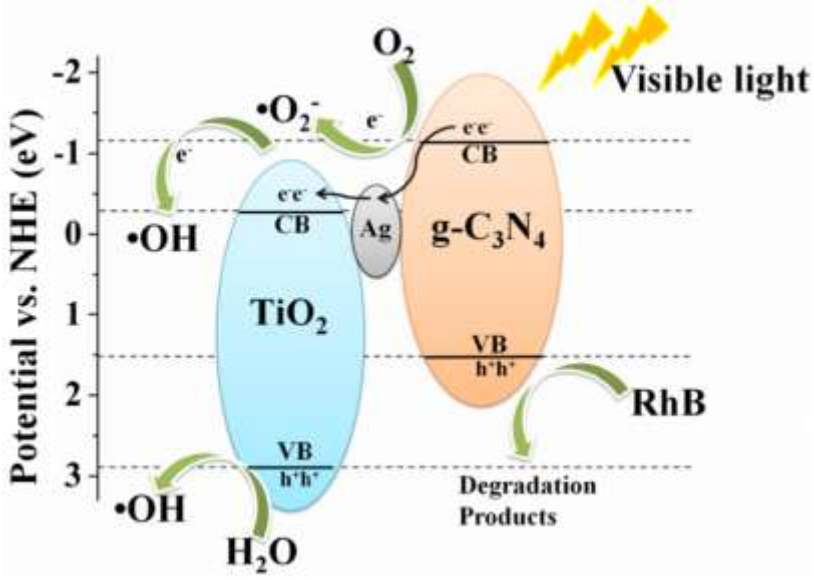

In general, the SPR of Ag and the narrow bandgap of Bi_2MoO_6 and g-C_3N_4 will help enhance the photocatalytic ability of TiO_2 in the visible light region whilst reducing the recombination rate of photogenerated electron holes by providing an alternate pathway for electron transfer within the NC. In addition to this, given the distinctive morphology of both co-catalyst Bi_2MoO_6 and g-C_3N_4, this can allow for an increase in the surface area and provide more active sites for photocatalysis to occur on the surface of the photocatalyst.

2.5 Method of fabricating Ag/TiO_2-based NCs

The effective implementation of enhancement strategies, such as noble metal deposition, heterojunction engineering, and coupling with visible-light-responsive semiconductors, depends strongly on the selected fabrication method. In Ag/TiO_2-based NCs, the synthesis route plays a critical role in governing particle size distribution, crystallinity, and interfacial contact, which are essential for harnessing the SPR effect of Ag and promoting efficient charge separation within TiO_2. Consequently, various chemical and physical approaches have been developed to construct Ag/TiO_2-based binary and ternary systems, each imparting distinct structural features and photocatalytic performances.

2.5.1 Sol-gel synthesis

The sol-gel method is one of the most established approaches for producing Ag/TiO_2-based NCs, as it enables high purity and molecular-level homogeneity (Chen et al., 2025). This method involves transitioning a system from a liquid sol to a solid gel phase, typically via hydrolysis and polycondensation of metal alkoxides or inorganic salt precursors (Sadek et al., 2022; Utomo et al., 2024). In the context of Ag/TiO_2 fabrication, the sol-gel process enables the uniform distribution of Ag within the TiO_2 matrix. For instance, a previous study used sol-gel techniques combined with chemical deposition to fabricate a NiO/Ag-TiO_2 NC electrode (Ravishankar et al., 2022). In this study, the sol-gel method enabled the formation of uniform TiO_2, facilitating the in-situ deposition of Ag and NiO within the matrix in a two-step synthesis process. This method was particularly effective for creating multi-component systems with high surface area and stable crystalline phases, which are essential for producing an efficient photocatalyst for water remediation.

2.5.2 Hydrothermal/Solvothermal synthesis

Hydrothermal and solvothermal methods are highly regarded for their ability to produce well-crystallized Ag/TiO_2-based heterostructures in a single step, without requiring further calcination. This is due to the high pressure and temperature in a sealed autoclave synthesis environment (Feng & Yam, 2024a). Unlike ambient methods, hydrothermal and solvothermal routes can facilitate and control the growth of specific crystal facets such as nanorods, nanoplates, and nanosheets. These unique morphological characteristics are often linked to enhanced charge carrier properties due to the presence of higher active sites for photocatalysis reactions to take place (Feng & Yam, 2024b). In a past study, the hydrothermal route was employed to fabricate a complex ternary system of g-C_3N_4/Ag-TiO_2 NCs (Sewnet et al., 2023). This method was deemed suitable for combining the materials, as it allows interfacial contact between TiO_2 and promotes Ag nucleation for deposition, whilst simultaneously promoting exfoliation of g-C_3N_4 to form nanosheets. Additionally, changing solvent environments in solvothermal processes can promote fine-tuning of the energy band gap and induce oxygen vacancies, which boost visible-light response and increase the number of active sites in NCs (Jiang et al., 2024).

2.5.3 Microwave-assisted synthesis

Microwave-assisted synthesis has recently emerged as a rapid and efficient alternative to conventional heating methods. It is highly compatible with most conventional methods such as chemical deposition and sol-gel synthesis and allows for a significant reduction in reaction time and energy consumption. In this approach, microwave irradiation is used to introduce TiO_2 and Ag into precursor solutions, enabling the facile in situ fabrication of ternary ZnO/TiO_2/Ag NCs (Mohan et al., 2021). This method is often paired with green synthesis techniques, such as using *Morinda citrifolia* fruit extract as a stabilizing or reducing agent, to produce biocompatible and bactericidal NCs. The localized and rapid heating provided by microwaves helps in achieving uniform distribution of AgNPs across the TiO_2 matrix, which is critical for enhancing the material's photocatalytic and antibacterial properties. The compatibility of microwave-assisted synthesis with bio-derived reducing and stabilizing agents has accelerated the shift towards sustainable nanomaterial fabrication. As a result, green chemistry has recently emerged as a viable alternative to conventional

chemical synthesis by leveraging naturally occurring biomolecules to synthesize nanomaterials (Kirubakaran et al., 2026).

2.6 Green synthesis of Ag/TiO_2-based nanocomposite

Recently, green chemistry has opened an alternative pathway to standard chemical synthesis by utilizing naturally occurring biomolecules for the synthesis of nanomaterials in a method called green synthesis (Devatha & Thalla, 2018). Nature provides a wide range of naturally occurring biomolecules that can be used in very diverse ways. These biomolecules, found in microorganisms and plants, are used to drive the synthesis of nanomaterials (Rana et al., 2020). However, in most cases, plant extract-mediated green synthesis reactions have been more frequently utilized than microorganism-based green synthesis. This is because plants are easier to use, readily available, and have a higher potential in the mass production of nanomaterials due to their fast reaction (Guerra et al., 2018). In addition, plant extract-mediated green synthesis provides precise control over the production of high-yield nanomaterials with well-defined sizes and varying morphologies in a one-pot reaction (Zhu et al., 2019).

Various studies have shown the successful synthesis of Ag-TiO_2 NCs with well-defined sizes and morphologies. For instance, green synthesized Ag-TiO_2 by Jayapriya and Arulmozhi (2021) using *Beta vulagris* peel extract had spherical morphology with a reduced size of about 40 nm as observed by SEM and TEM. Another study by Nguyen et al. (2022) reported that green synthesized Ag-TiO_2 via *Cleistocalyx operculatus* leaf extract also demonstrated spherical surface morphology with sizes ranging from 20 nm to 40 nm. Various other studies also revealed similar surface morphology of spherical Ag NPs covering the surface of TiO_2 with promising application in the photodegradation of organic pollutants (Jiang et al., 2019; Kumar et al., 2016; Mohapatra et al., 2021; Nethravathi et al., 2022; Saeed et al., 2019; Tavakoli et al., 2019). This suggests that green synthesis via plant extracts can form Ag-TiO_2 NCs with controlled morphology. A compilation of green-synthesized Ag-TiO_2 NCs can be seen in Table 2.2.

Table 2–2: Summary of selected studies of TiO_2-based nanocomposite synthesized via green synthesis for the photocatalytic degradation of organic pollutants

Type of plant extract	Photocatalyst	Morphology and size	Organic pollutant	Major findings	Reference
Beta vulagris peel	Ag-TiO_2	Spherical 25 ± 74 nm	Methylene Blue, Congo Red, Methyl Orange	Degradation efficiency for removal of Methylene Blue (92% in 9 min), Congo Red (84% in 20 min) and Methyl Orange (88% in 10 min).	Jayapriya and Arulmozhi (2021)
Cleistocalyx operculatus leaf	Ag-TiO_2	Spherical 20 – 40 nm	Rhodamine B	Up to 91.4% of Rhodamine B was successfully removed within 180 min.	Nguyen et al. (2022)
Mangifera indica leaf	Ag-TiO_2	Spherical	Methylene Blue	68% photodegradation was achieved for 7.81×10^{-5} mol/L initial MB concentration at pH 8 by using 0.19 g/L photocatalyst	Mohapatra et al. (2021)
Cucumis melo juice	Ag-TiO_2	Spherical 9.12 nm	Methylene Blue	95.3% of Methylene Blue was degraded in 120 min under irradiation of visible light.	Nethravathi et al. (2022)
Azadirachta indica leaf	Ag-TiO_2	Spherical	Methylene Blue, Rhodamine B	More than 90% of Methylene Blue and Rhodamine B dyes were degraded in 120 min	Saeed et al. (2019)
Pranus Cerasus seed	Ag-TiO_2-G	Spherical Ag-TiO_2 distributed onto graphene sheets 10-20 nm	Acid Orange 7 (AO7)	Graphene with 35 wt% Ag exhibits 99% AO7 degradation within 20 min	Tavakoli et al. (2019)

				but only 61% of degradation for bare TiO_2	
Cinnamomum camphora leaf	Au-Ag-TiO_2	Spherical 12.6 ± 1.7 nm	Methyl Orange	Degradation rate of Au-Ag-TiO_2 reached ~90% within 30 min of UV-vis light irradiation but pure-TiO_2 only had 50% after 60 min	Jiang et al. (2019)
Nephelium lappaceum L. peel	Ag-TiO_2	Spherical 100-180 nm	Methylene Blue	>81% degradation rate of Methylene Blue in 600 min under sunlight for Ag-TiO_2.	Kumar et al. (2016)

Therefore, despite the prevalence of reports on the successful green synthesis of binary TiO_2-based NCs, the synthesis of ternary NCs using the same methods remains feasible. This potential is supported by the binding properties of naturally occurring compounds in plant-based extracts. These compounds are also prevalent in palm oil mill waste, and it could prove as a possible source to obtain extracts that are also rich in phytochemicals for the green synthesis of nanomaterials.

2.6.1 Principles and mechanisms of green synthesis

Green synthesis of nanomaterials is fundamentally governed by redox reactions mediated by naturally occurring biomolecules, offering an environmentally benign alternative to conventional chemical synthesis routes. In this approach, bio-derived compounds function as reducing agents, stabilizers, and, in some cases, capping agents, thereby eliminating the need for toxic chemicals and energy-intensive processes (Zhu et al., 2019). The general mechanism of green synthesis involves three main stages: the reduction of metal precursor ions, the nucleation and growth of nanoparticles, and the stabilization of the resulting nanostructures to prevent agglomeration.

In plant extract-mediated green synthesis, a diverse mixture of phytochemicals including polyphenols, flavonoids, polysaccharides, terpenoids, alkaloids, proteins, and

organic acids, collectively drives these processes (Bawazeer et al., 2021). These biomolecules donate electrons to metal ions such as Ag^{+} ions, facilitating their reduction to metallic nanoparticles, while functional groups in the phytochemicals adsorb onto the nanomaterial surface, providing steric or electrostatic stabilization. Figure 2.11 illustrates the general mechanism involved in the green synthesis of Ag/TiO_2-based NCs. The process is relatively simple and does not require the separation or purification of individual bioactive compounds prior to synthesis, making it attractive for scalable and sustainable nanomaterial production.

Figure 2–11: General mechanism involved in the green synthesis of Ag/TiO_2-based NCs

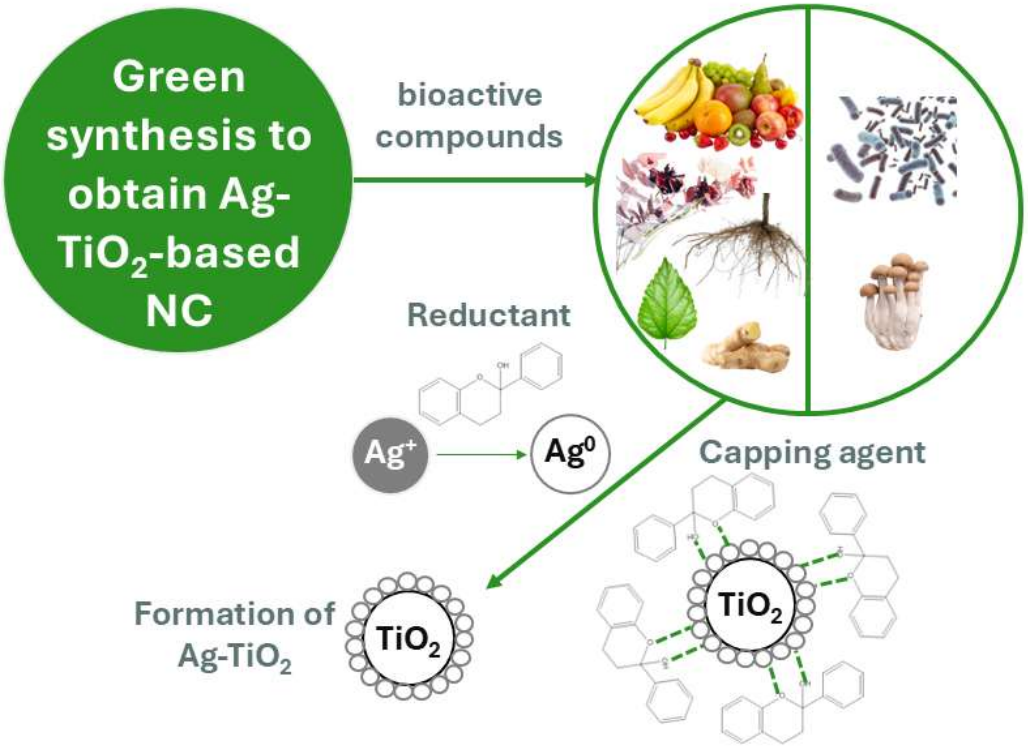

Despite these advantages, the heterogeneous nature of plant extracts introduces variability in reaction kinetics, nanoparticle size, and morphology. This variability arises from differences in phytochemical composition, concentration, and functional group distribution among plant species, plant parts, and extraction conditions. Spectroscopic analyses such as FTIR have provided insight into the functional groups involved in nanoparticle formation. For example, Chand et al. (2019) reported that flavonoids and terpenoids present in onion and tomato extracts were primarily responsible for the reduction

and stabilization of AgNPs. However, the precise contribution of individual phytochemicals often remains difficult to isolate due to synergistic interactions within the complex NP matrix.

As phytochemical profiles differ significantly across botanical sources, the selection of plant material plays a crucial role in determining the efficiency, reproducibility, and functionality of green-synthesized nanomaterials. While fresh plant extracts have been widely investigated, increasing attention is being directed toward agricultural waste materials such as fruit peels and plant residues, which are rich in bioactive compounds yet remain underutilized (Ying et al., 2022). These waste-derived resources offer a sustainable, cost-effective alternative while supporting circular-economy principles through biomass valorization. Therefore, exploring agricultural waste as a reducing and stabilizing agent offers a promising pathway to the controlled synthesis of Ag/TiO_2-based NCs with enhanced photocatalytic and antibacterial performance.

2.6.2 POME as a green reducing and stabilizing agent

POME is a highly concentrated wastewater generated during the final stages of palm oil processing, characterized by significant levels of organic pollutants, solids, and oils that pose substantial environmental risks if not properly managed. Despite its reputation as a problematic industrial waste, POME has emerged as a viable and sustainable alternative to conventional plant extracts for the green synthesis of nanomaterials (Aliero et al., 2024; Gan et al., 2012). As a waste-derived resource, POME aligns with circular economy principles by providing a low-cost, eco-friendly source of bioactive compounds needed for the biogenic reduction of metal ions. The transition from fresh botanical extracts to POME is increasingly seen as a strategic pathway to mitigate environmental pollution while simultaneously producing high-value nanomaterials for biomedical and industrial applications.

The viability of POME as a reducing and stabilizing agent is primarily attributed to its rich profile of phenolic compounds and other bioactive phytochemicals. High-Performance Liquid Chromatography and Gas Chromatography Mass Spectroscopy analyses have identified several key phenolic acids in POME, including gallic acid, caffeic acid, ascorbic acid, vanillic acid, coumaric acid, and myricetin (Aliero et al., 2024). These compounds possess potent antioxidant properties and contain functional groups such as

hydroxyl, carbonyl, and carboxylic groups that actively facilitate the reduction of Ag^{+} into Ag^{0} (Aliero et al., 2025). Furthermore, these phytochemicals act as capping agents, forming a protective layer around the nanoparticles that prevents aggregation and ensures long-term stability.

In addition to phenolic acids, POME contains various other phytonutrients, including carotenoids, tocols (vitamin E), sterols, and squalene, which can be extracted using green techniques such as microwave- or ultrasound-assisted extraction (Ofori-Boateng & Lee, 2013; Teh et al., 2017). The synergistic interaction of these diverse bioactive components enables POME to serve as an effective all-in-one matrix for nanomaterial formation, often yielding AgNPs with superior stability and significant biological activity (Aliero et al., 2025). For instance, AgNPs synthesized from POME have demonstrated high crystalline stability and remarkable antibacterial and antibiofilm efficacy against pathogens such as *Staphylococcus aureus* and *Pseudomonas aeruginosa*. By harnessing these discovered bioactive compounds, the utilization of POME not only addresses industrial waste management challenges but also provides a robust, reproducible platform for the controlled synthesis of functional Ag/TiO_2-based NCs.

2.7 Immobilization of Ag/TiO_2-based nanocomposites onto membranes

Regardless, the main issue in the actual application of TiO_2-based NCs is the difficulty of separating them after post-treatment. Therefore, the immobilization of TiO_2-based NCs has been actively studied to overcome this problem. Various materials, particularly polymers and ceramics, have been widely used as supports for TiO_2-based UV-responsive photocatalytic membranes (PMs). Some of the immobilized TiO_2 PMs include TiO_2-coated and TiO_2-blended PMs. This is achieved by various methods such as dip-coating (Djafer et al., 2010; Fischer et al., 2015), layer-by-layer self-assembly (Starr et al., 2016), electrospraying (Lang et al., 2022), atmospheric plasma spraying (APS) (Lin et al., 2012), as well as chemical vapor deposition (CVD), which are summarized in Table 2.3.

Table 2–3: Fabrication methods of TiO_2-based UV-responsive photocatalytic membranes.

	Membrane type	TiO_2 precursor/TiO_2 type	Membrane fabrication method	Remarks	Reference
TiO_2-coated membranes	Al_2O_3 UF tubular membrane	Titanium isopropoxide (TTIP)	Chemical vapor deposition (CVD)	• A gaseous stream enriched with TTIP vapor. • Pyrolytic decomposition of TTIP vapor in a 600 °C furnace and TiO_2 NPs formation. • TiO_2 nanoparticles deposited on the membrane surface.	Athanasekou et al. (2012)
	Al_2O_3	TiO_2	Atmospheric plasma spraying	• TiO_2 powder preparation. • The plasma power (21 kW) was used to spray TiO_2 powder at a spraying distance (10 cm) to coat TiO_2 on Al_2O_3 support.	Lin et al. (2012)
	Nylon-6	TiO_2 NPs	Electrospraying	• The coating was constructed by coupling the electrospinning of a polymer solution with the electrospray of TiO_2.	Daels et al. (2014)
TiO_2 blended membranes	PVDF	TiO_2 NPs	Phase inversion	• Casting solutions included PVDF and TiO_2 particles in n-methyl-2-pyrrolidone (NMP) solvent at 60–65 °C. • Casting solutions were cast onto the non-woven sheet as a base substrate. • Membranes were immersed in a	Damodar et al. (2009)

			23–25 °C tap water coagulation bath for 1 day and were washed with distilled water.	
Cellulose triacetate membrane (CTA)	TiO_2 NPs	Phase inversion	• Casting solutions included CTA, plasticizer, and TiO_2 in CH_3Cl solvent. • Casting solutions were mixed and placed to allow the solvent evaporation and polymerization occurrence.	Molinari et al. (2004)
PVDF/SPES	TiO_2 NPs	Phase inversion	• Polyethersulfone sulfonation treatment (SPES). • Casting solutions included PVDF, SPES and TiO_2 in DMAc solvent with polyvinyl pyrrolidone (PVP) as the pore former. • Casting solutions were cast on polyester non-woven fabric, and were immersed in water, and washed.	Rahimpour et al. (2011)

Whether they are for ceramic or polymer supports, the bonding strength of the photocatalysts and membrane supports is a key criterion, influencing the membrane's normal operation. Several studies have shown that the attachment of photocatalysts to membranes is often insufficient to enable the photocatalytic membrane to withstand multiple cycles without a decline in performance (Leong et al., 2014). To achieve better adhesion, membrane modification has been targeted and has attempted to introduce the key functional groups on the membrane surface that can stably hold TiO_2-based catalysts. It is well known that the surface of polymers with –COOH, –SO_2OH, and ether bonds exhibits self-assembly behaviors of TiO_2 through two different adsorption schemes (Shi et al., 2019). One scheme

is that TiO_2 is bound to the oxygen atoms of these groups via coordination with the ion Ti^{4+}. The other scheme is to form a hydrogen bond between these groups and the hydroxyl group of the TiO_2 surface. For instance, the plasma-enhanced graft of polyacrylic acid (PAA) with –COOH groups on the surface of the membrane, including PVDF and PTFE, has been reported to facilitate TiO_2 to deposit onto functionalized membrane surfaces successfully (You et al., 2012). Another approach was attempted by blending other polymers, such as poly- (styrene-alt-maleic anhydride) (SMA) with –COOH, and the sulfonated polyethersulfone (SPES) with sulfone group and ether bond for TiO_2 self-assembly.

Through green synthesis, bonding between the TiO_2-based NC and the membrane supports may be achieved, as plant extracts attached to the green-synthesized NC surface may strengthen interactions with functional groups on the membrane surface. Moreover, the addition of fabricated TiO_2 could enable a responsive photocatalytic membrane in the visible-light region. This can promote the application of these membranes under solar-irradiated systems.

CHAPTER 3:

RESEARCH METHODOLOGY

3.1 Materials

Titanium butoxide, $Ti(OCH_2CH_2CH_2CH_3)_4$ (97% reagent grade), bismuth (III) nitrate pentahydrate, $Bi(NO_3)_3 \cdot 5H_2O$ (ACS reagent, ≥98.0%), Sodium molybdate dihydrate, $Na_2MoO_4 \cdot 2H_2O$ (ACS reagent, ≥99 %), urea, NH_2CONH_2 (ACS reagent, 99.0-100.5%), and polyvinylpyrrolidone, $(C_6H_9NO)_n$ (average M_w ~1,300,000) were purchased from Sigma-Aldrich. Hydrochloric acid (HCl), Sodium hydroxide (NaOH), ethylene glycol ($HOCH_2CH_2OH$, ≥99.5%) and absolute ethanol (EtOH) were obtained from Merck. Silver nitrate, $AgNO_3$ (AR, 99.98%), was procured from Bendosen. Other materials include polyacrylonitrile $(C_3H_3N)_n$ (average M_w ~150,000), ultrapure water, UPW (HPLC grade) and dimethyl sulfoxide, $(CH_3)_2SO$ (AR, ≥99.9%) that were purchased from Shanghai Macklin Biochemical Co., Ltd., Fisher Chemical, and RCI Labscan Ltd., respectively. A schematic overview of the experimental methodology performed in this study is illustrated in Figure 3.1.

Figure 3–1: Schematic overview of the overall experimental methodology

3.2 Preparation and analysis of POME extracts

Raw POME was obtained from the SALCRA Oil Palm Mill in Kota Samarahan, Sarawak. POME extract was prepared according to a previous study (Gan et al., 2012).

Sampled raw POME was dried at 60 °C for 24 hours in a glass container. After drying, the POME samples were scraped, ground into powder, and sieved to remove coarse particles. Bioactive compounds were extracted from the dried POME by mixing 3 g of the dried POME powder with 100 mL of distilled water and stirring the mixture at 80 °C for 30 minutes. The mixture was then filtered using Whatman filter paper to attain the POME extract. The extract was kept in a refrigerator at 4 °C until further use. Figure 3.2 shows the extraction process of raw POME.

Total phenolic content (TPC) and Total flavonoid content (TFC) analysis was carried out to confirm the presence of bioactive compounds that were responsible for the reduction and stabilization of the POME-derived ternary NCs. TPC and TFC analysis was carried out using the Follin-Ciocalteu method and aluminum chloride colorimetric method as described by Nuzul et al. (2022) with some slight modifications. Prior to TPC and TFC analysis, POME extracts were subjected to a vacuum filter to obtain the crude extracts. For TPC analysis, about 5 mg of the samples was dissolved in 5 mL of EtOH. A total of 300 uL of the dissolved samples was taken and put in a test tube. Then, 2250 uL of Folin–Ciocalteu reagent was added and allowed to rest for about 10 minutes before 2250 uL of 6% sodium carbonate solution was added to the mixture. The mixture was gently mixed and left to further react for 60 minutes. This was followed by measuring the absorbance value via UV-Vis spectrometry at λ max of 765 nm by using gallic acid standards (100, 200, 300, 400, 500 ug/mL) as the reference standard. The results were expressed as mg GAE/g extract.

For TFC analysis, 5 mL of the dissolved sample was mixed with 5 mL of 2% aluminum chloride solution in a test tube. The mixture was shaken and left to stand for 10 minutes before being analyzed with UV-Vis spectrometry. Flavonoid detection was performed at the λ max of 415 nm, with quercetin (25, 50, 75, 100, 125 ug/mL) as the reference standard. The results were expressed as mg QE per g of extract.

Figure 3–2: Extraction of bioactive compounds from raw POME

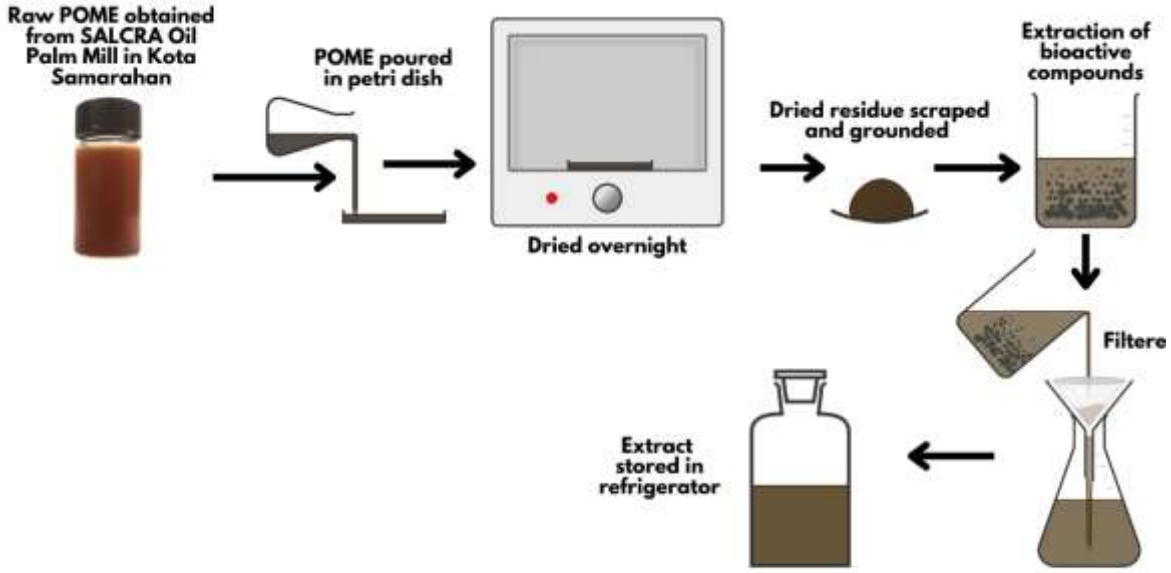

3.3 Synthesis of TiO_2.g-C_3N_4 and Bi_2MoO_6

TiO_2 was synthesized using the sol-gel method with titanium (IV) butoxide as the precursor, while g-C_3N_4 was prepared via pyrolysis of urea, following our previously published work (Kanakaraju et al., 2024). The sol-gel synthesis of TiO_2 was performed by mixing titanium (IV) butoxide with EtOH in a 1:2 ratio. The mixture was stirred for 30 minutes, after which 100 mL of distilled water was added dropwise. The resulting solution was then stirred for an additional 2 hours, followed by filtration and washing three times with distilled water and EtOH. The gel was then dried at 110 °C for 2 hours before calcination in a furnace (Protherm PLF 110/30) at 300 °C for 5 hours.

For g-C_3N_4 synthesis, approximately 10 g of urea was placed in a crucible and subjected to pyrolysis at 550 °C for 3 hours, resulting in bulk g-C_3N_4. The g-C_3N_4 obtained was dispersed in deionized water, then filtered and washed to remove impurities. The resulting material was then dried in an oven to obtain the yellow bulk g-C_3N_4.

Bi_2MoO_6 was synthesized via a green solvothermal method with slight modifications from reported procedures (Kanwal et al., 2023; Selvamani et al., 2023). In this process, 2 mmol of $Bi(NO_3)_3 \cdot 5H_2O$ and 1 mmol $Na_2MoO_4 \cdot 2H_2O$ were each dissolved in 30 mL of ethylene glycol under magnetic stirring to obtain Solution A and B, respectively.

Subsequently, Solution A and Solution B were combined, and 30 mL of EtOH was added. A 3 mL of POME extract (10% v/v relative to the ethanol volume) was then added to the mixture as a stabilizing agent, and the solution pH was adjusted to 8, resulting in the precipitation of Bi_2MoO_6. The solution was transferred into a hydrothermal reactor and kept at 150 °C for 12 hours. After the reaction was completed, the precipitate was filtered and washed with deionized water and EtOH several times. Finally, the precipitate was dried in an oven at 110 °C for 2 hours.

3.4 Green synthesis of $Ag/Bi_2MoO_6/TiO_2$ and $Ag/g\text{-}C_3N_4/TiO_2$ NCs

The synthesis of $Ag/Bi_2MoO_6/TiO_2$ (ABMOT) NC was performed by mixing TiO_2 and Bi_2MoO_6 in a 1:0.3 ratio in 50 mL of distilled water. The mixture was then left under continuous stirring for 30 minutes. Ag deposition was carried out by dissolving $AgNO_3$ in 50 mL of water, followed by the addition of 5 mL of POME extract (10% v/v relative to the water volume) to facilitate Ag reduction. The POME extract used for Ag deposition was prepared from the same raw material, with the same extraction conditions applied throughout, ensuring a consistent bioactive composition across batches. This solution was then combined with the Bi_2MoO_6/TiO_2 mixture and subjected to microwave irradiation in a commercial microwave oven at 100 W for 6 minutes to promote the deposition of AgNPs onto the binary system. The resulting mixture was subsequently stirred magnetically for another 2 hours, then filtered, washed and dried at 100 °C for 2 hours. The resulting ABMOT ternary NC was then calcinated at 450 °C for 3 hours and stored for further testing. The synthesis of $Ag/g\text{-}C_3N_4/TiO_2$ (AGCNT) was done in the same manner as the above-mentioned method, but by mixing $g\text{-}C_3N_4$ with TiO_2 in a 1:1 ratio. A schematic summary of the overall synthesis methodology for the prepared NCs is presented in Figure 3.3.

Figure 3–3: Schematic summary for the synthesis of ABMOT and AGCNT NCs.

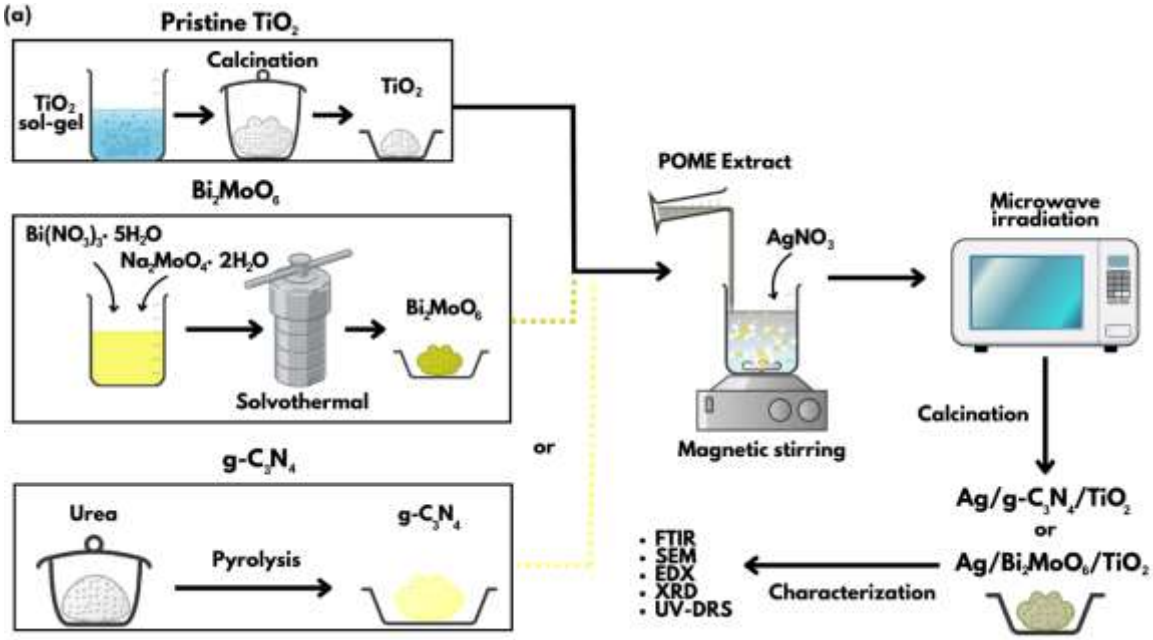

3.5 Characterization of POME-derived NCs

Scanning electron microscopy (SEM) coupled with Energy-dispersive X-ray spectroscopy (EDX) (Model: JEOL, JSM-IT500HR) was used for the determination of morphological properties and elemental composition of the NCs. Analysis of functional groups that were present in the NCs was done via Fourier transform infrared spectroscopy (FTIR) (Model: Thermo Nicolet iS10) by using KBr pellets as a standard at a wavelength of 4000 – 400 cm^{-1}. X-ray diffraction analysis (XRD, PANalytical X'pert Pro) was done to determine the crystalline structure and phase of the green-synthesized samples. UV-vis diffuse reflectance spectroscopy (UV-Vis DRS) (Model Carry 5000) was employed to determine the effective absorption spectra of NCs, and the Kubelka-Munk plot was established to confirm any changes in the energy bandgap.

3.6 Evaluation of photocatalytic activity

The photocatalytic efficiency of the synthesized NCs was determined by studying their ability to degrade OTC antibiotics under visible light (Figure 3.4). First, a fixed amount of the ternary NC was added to 10 mg/L of OTC solution and mixed with a magnetic stirrer. The suspension was left to stir in the dark for 1 hour to allow for the adsorption-desorption

equilibrium of OTC onto the photocatalyst. After 1 hour under dark conditions, the suspension was irradiated under the illumination of Xenon Lamp (300 W) at 5,800,000 lux to simulate sunlight. The photocatalytic degradation experiment was done for another 2 hours. A fixed aliquot was taken every 30 minutes over the 3-hour photocatalytic experiment under simulated sunlight. All aliquots of the suspension were spun with a tabletop centrifuge (Hettich, EBA 200) at 6000 rpm for 10 minutes before being subjected to analysis with a UV-Vis spectrophotometer. The analysis was done by monitoring the changes at λ max of 352 nm, the OTC removal efficiency was calculated as follows:

$$\text{Removal efficiency (\%)} = \frac{C_i - C_f}{C_i} \times 100\% \quad \text{.....(Eq 3.1)}$$

where C_i is the initial concentration of OTC and C_f is the final concentration of OTC. The photocatalytic treatment was conducted by varying the catalyst dosage (0.3 g/L, 0.6 g/L, 1.2 g/L) and the initial concentration of OTC (10 mg/L, 15 mg/L, 20 mg/L).

Additionally, a recyclability study was conducted to assess the stability of AGCNT and ABMOT over 4 consecutive rounds. This was done by running photocatalysis at optimized conditions of 0.6 g/L catalyst dosage with an initial concentration of 10 mg/L for OTC. After one cycle, the photocatalyst was recovered through centrifugation, washed with distilled water and ethanol to remove residual pollutants, followed by drying and subsequently reusing them under the same experimental conditions.

Figure 3–4: Photocatalytic evaluation of ABMOT and AGCNT NCs for the degradation of OTC under visible light.

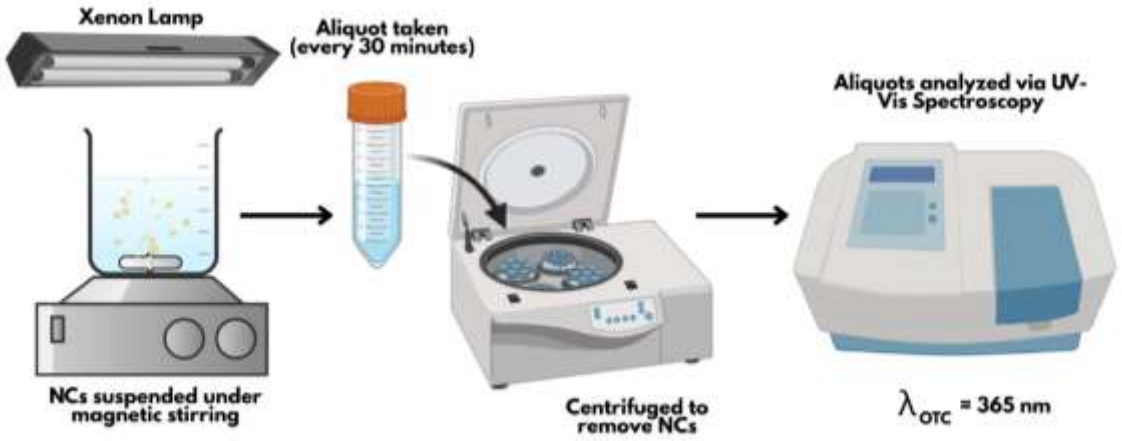

3.7 Evaluation of antibacterial activity

The antibacterial study was conducted via the disc diffusion method to determine the antibacterial effectiveness of both ABMOT and AGCNT NCs against both gram-positive bacteria, *E. coli* and gram-negative bacteria, *S. aureu*s (Figure 3.5). The bacterial strains were obtained from the Microbiology Laboratory 2, Faculty of Resource Science and Technology, UNIMAS. The bacterial strains were revived in nutrient broth (NB) and inoculated onto nutrient agar (NA) plates. Next, the inoculum was standardized by transferring several colonies into fresh NB and adjusting the culture to a turbidity that is equivalent to 0.5 McFarland standard. The antibacterial assay was conducted by first comparing the effectiveness of ABMOT and AGCNT with their unary and binary counterparts in inhibiting the growth of the bacterial samples. All samples were fixed at a concentration of 1 g/L. A determined amount of the samples mentioned was mixed in a phosphate buffer (PBS) solution. Sterile filter papers were then dipped into the PBS solution containing these samples. After that, the standardized inoculum was then swabbed onto NA plates using sterile cotton swabs and the treated filter papers were then placed on the surface of the agar and incubated at 37 °C for 24 hours. The diameter of the inhibition zones was measured after the incubation period. This experiment was repeated by varying the concentration of ABMOT and AGCNT at 1, 2, 4, 8, and 10 g/L, respectively.

Figure 3–5: Disk-diffusion method for the assessment of antibacterial activity of ABMOT and AGCNT NCs.

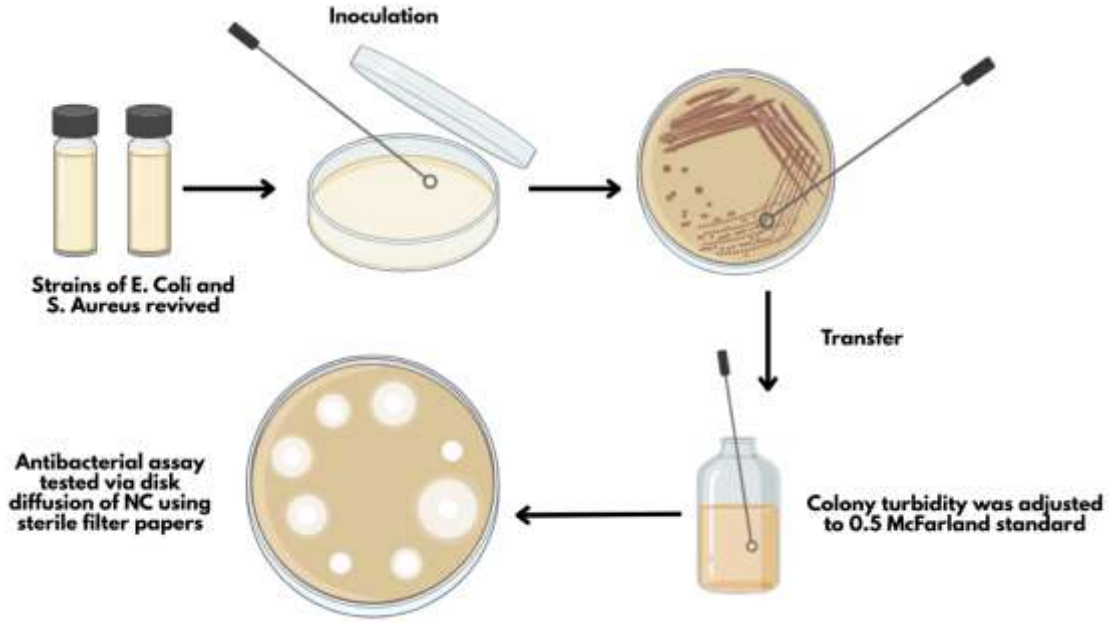

3.8 Fabrication of POME-derived ternary NC into PAN membranes

The fabrication of NCs into the PAN membrane was done via the phase inversion method. In this process, 85 g of DMSO was measured and poured into a beaker. This was followed by the addition of 1% of ABMOT NC based on the weight of PAN into the beaker containing the solvent. The solution was stirred for 1 hour at 80 °C. After thorough mixing, the solution was transferred into a conical flask, where 15 g of PAN powder was added. The mixture was then continuously stirred at 80 °C for 24 hours until complete dissolution and homogenization were achieved. The final solution was then cast onto a clean glass plate using a casting rod to obtain a uniform membrane film. The glass plate was then immersed in a deionized water coagulation bath to induce phase inversion and form the solid membrane structure. After complete phase separation, the membrane was carefully peeled off and further soaked in ultrapure water to remove residual solvents. The final membranes were stored in ultrapure water until further use. A similar method was used to fabricate AGCNT. A bare PAN membrane was also prepared in the same manner, except without the addition of NC. A summary of the composition used to prepare the bare PAN membrane and NC membranes is summarized in Table 3.1.

Table 3–1: Composition of ABMOT and AGCNT NCs-embedded PAN membranes

Membrane	PAN (g)	DMSO (g)	NC loading (g)
PAN	15.00	85.00	0.00
1% ABMOT@PAN	15.00	85.00	0.15
2% ABMOT@PAN	15.00	85.00	0.30
1% AGCNT@PAN	15.00	85.00	0.15
2% AGCNT@PAN	15.00	85.00	0.30

3.9 Characterization of membranes

The membranes were characterized using SEM (Model: JEOL JSM-IT500HR), coupled with EDX, to determine their surface morphology and cross-section. Additionally, FTIR spectroscopy (Model: Thermo Nicolet iS10, equipped with attenuated total reflectance

(ATR)) was used to confirm the chemical interaction of NCs within the membrane matrix in the spectral range of 2000–400 cm^{-1}.

3.10 Evaluation of fabricated membranes

The membrane permeation test served as the primary method for evaluating the performance of pristine PAN membranes and those incorporating ABMOT and AGCNT ternary NCs. This test consisted of pure water flux and OTC rejection. For the pure water flux test, membranes were compacted using a backflow that was fed back into the feed of the filtration system setup. Pure water flux was determined by pumping ultrapure water to the system at a pressure of 2 bar for 1 hour for stabilization of the membrane system. Then, the water flux test was conducted at a pressure of 1 bar for another hour, and the results were recorded every 10 minutes. The procedure was repeated 3 times to ensure accurate reading and replicability of water flux results. Similarly, the OTC rejection test was performed following the same procedure but with 10 g/L of OTC solution as the feed. The concentrations of the initial feed and permeate were measured using a UV-Vis spectrophotometer (Model: Perkin-Elmer LS55) at a λ max of 352 nm. The water flux and OTC rejection were obtained following the equation as described by Huang et al. (2022):

$$J_{flux} = \frac{V}{A \times t \times P} \left(\mathrm{L \cdot m^{-2} \cdot h^{-1}}\right) \quad \text{.....(Eq 3.2)}$$

$$\mathrm{RR}\ (\%) = \frac{C_{feed} - C_{permeate}}{C_{feed}} \times 100\% \quad \text{.....(Eq 3.3)}$$

where, J_{flux} represents the water flux ($L \cdot m^{-2} \cdot h^{-1}$), V is the volume of permeate, A, is the effective area of membrane (m^2), P is the operational pressure (bar), RR is rejection rate (%), C_{feed} is the concentration of OTC in the feed and $C_{permeate}$ is the concentration of OTC from the permeate collected. A summary of the membrane workflow is shown in Figure 3.6.

Figure 3–6: Schematic overview of the synthesis, characterization, and evaluation of NC-embedded PAN membranes.

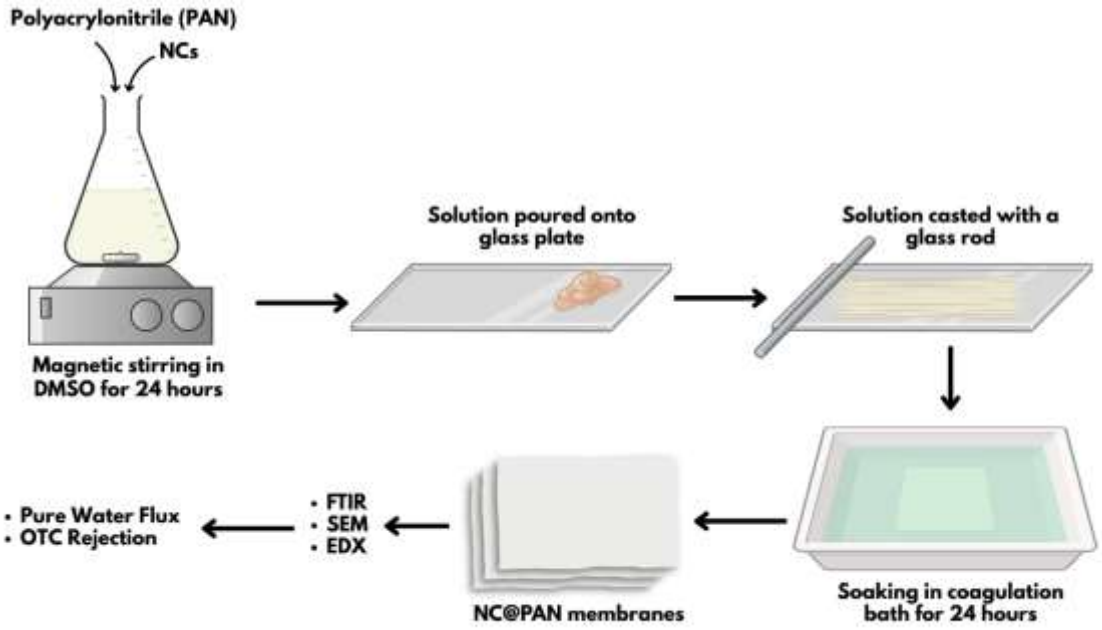

CHAPTER 4:

FINDINGS AND DISCUSSION

4.1 Analysis of POME extracts

4.1.1 TPC and TFC analysis of POME extracts

To verify the suitability of POME as a green reducing and stabilizing agent in NC synthesis, compound confirmation tests were conducted to determine the key phytochemicals, with particular attention to phenolic and flavonoid compounds. These compounds are well-known for their role in the green synthesis of NPs, as they can both reduce metal ions and prevent agglomeration, thereby promoting the formation of stable NPs. The TPC content of POME extracts obtained was 240.70 ± 2.64 gallic acid equivalent (GAE) mg/g (Table 4.1). These values align well with past studies that focused on the extraction of phenolics from POME, confirming that this waste stream harbors significant quantities of polyphenols (Ofori-Boateng & Lee, 2013). Notably, the phenolic content observed is comparable to that of other plant extracts that were previously studied, highlighting the potential of POME as a possible green source for nanomaterial synthesis. (Bhardwaj & Singh, 2021; Nguyen et al., 2022; Rahmawati et al., 2023). This opens up possibilities for agro-industrial waste to be utilized and become added-value products, thus promoting a circular economy.

The TFC in the extracts was found to be 42.50 quercetin equivalents (QE) mg/g (Table 4.1). Torres-Limiñana et al. (2022) reported the green synthesis of Ag-TiO_2 using an extract of *Eucalyptus globulus* and assessed the presence of secondary metabolites, namely the phenolics and flavonoid contents. Compared to the current study, their findings indicated that a higher flavonoid content relative to phenolics. This variation could be attributed to the differences in solvent selection, which may have favored the extraction of phenolics over flavonoids. Nevertheless, given that phenolics and flavonoids were detected in the POME extracts, their presence makes them well-suited for the synthesis of ABMOT and AGCNT.

Additionally, while there is no universal threshold for TPC and TFC values required for green nanomaterial synthesis, previous studies have shown that extracts containing sufficient phenolic and flavonoid compounds can effectively function as reducing and stabilizing agents (Hussain et al., 2025). The effectiveness of these extracts depends not only on their total content but also on the chemical nature and redox activity of the bioactive compounds present. In this study, the high TPC and appreciable TFC values obtained for POME fall within, and in some cases exceed, the ranges of 20 mg/L for TPC and TFC reported for successful green synthesis of nanomaterials (Vera et al., 2023). This further confirms the suitability of POME as a viable green source for the fabrication of ABMOT and AGCNT NCs.

Table 4–1: TPC expressed in gallic acid equivalent (GAE) (mg/g) and TFC expressed in quercetin equivalent (QE) (mg/g) of the POME extracts.

Extract	TPC as GAE (mg/g)	TFC as QE (mg/g)
POME Extract	240.70 ± 2.64	42.50 ± 0.01

4.2 Characterization of ABMOT and AGCNT

4.2.1 FTIR spectra

FTIR spectra of unary components, TiO_2, Bi_2MoO_6, g-C_3N_4, AgNP, as well as the ternary heterostructure of ABMOT and AGCNT, were analyzed within the range of 400 – 4000 cm^{-1} to identify the functional groups present in the NCs. Through FTIR analyses, it is possible to evaluate any potential chemical interactions between each component in the NCs matrix.

Figure 4.1 shows the FTIR spectra of both ABMOT and AGCNT, compared with their individual components. FTIR analysis shows that pristine TiO_2 had broad absorption peaks at 3425 cm^{-1} and strong peaks at 640 cm^{-1} corresponding to -OH stretching and Ti-O-Ti bonds, respectively (Figure 4.1c). Bi_2MoO_6 showed strong characteristic peaks at 1107 cm^{-1}, 813 cm^{-1} and 729 cm^{-1} corresponding to Bi-O bond, Mo-O stretching vibration modes and MoO_6 asymmetric stretching, respectively, as shown in Figure 4.1b (Cai et al., 2019;

Zhang et al., 2016). The characteristic peaks for g-C_3N_4 were mainly detected from 800-1700 cm^{-1}, with the s-triazine ring peak detected at 810 cm^{-1} (Figure 4.1a). The bands at 1639, 1566 and 1458 cm^{-1} are attributed to aromatic C-N vibrations, while bands at 1323 and 1246 cm^{-1} belong to the vibration of fully condensed N-$(C)_3$ and partially condensed C-N-H link, respectively (Xiao et al., 2021). The characteristic bands of AgNPs at 1384 cm^{-1} and 1620 cm^{-1} are mainly ascribed to C=C stretching of aliphatic alkenes and C=O from aldehydes or ketones, respectively, as seen in Figure 4.1d (Das et al., 2025). The presence of C=C and C=O peaks is ascribed to the phenolic compounds that are present on the surface of the AgNPs. Additionally, the C=O peak observed in TiO_2, Bi_2MoO_6, and ABMOT NCs may also arise from weakly adsorbed carbon dioxide from the surrounding environment, which can interact with surface hydroxyl groups to form surface carbonate species. The peaks observed at approximately 671 and 779 cm^{-1} are attributed to Ag-O-Ag stretching vibrations.

In the case of ABMOT (Figure 4.1e), most of the characteristic bands of TiO_2 were maintained, except for the appearance of broader bands between 600-800 cm^{-1}, a distinct peak at 1384 cm^{-1} and a widened peak at 3142 cm^{-1}. The observed could be linked to the presence of Bi-O and Mi-O bonds and bound organic compounds as described. Similarly, changes in the AGCNT peaks (Figure 4.1f) were detected. The broader peak at 3240 cm^{-1} is attributed to overlapping O-H stretching vibrations of TiO_2 and the N-H bonds of g-C_3N_4. The peaks in the 800-1700 cm^{-1} range associated with g-C_3N_4 remained intact, while the broad peaks observed between 600 and 800 cm^{-1} were attributed to the overlapping of s-triazine ring vibrations with Ti-O-Ti and Ag-O-Ag stretching modes, each within that range. Thus, the FTIR spectra of the samples confirm the presence of all key functional groups associated with ABMOT and AGCNT ternary heterostructures.

Figure 4–1: FTIR spectra of (a) Bi_2MoO_6, (b) g-C_3N_4, (c) TiO_2, (d) AgNP, (e) ABMOT NC and (f) AGCNT NC

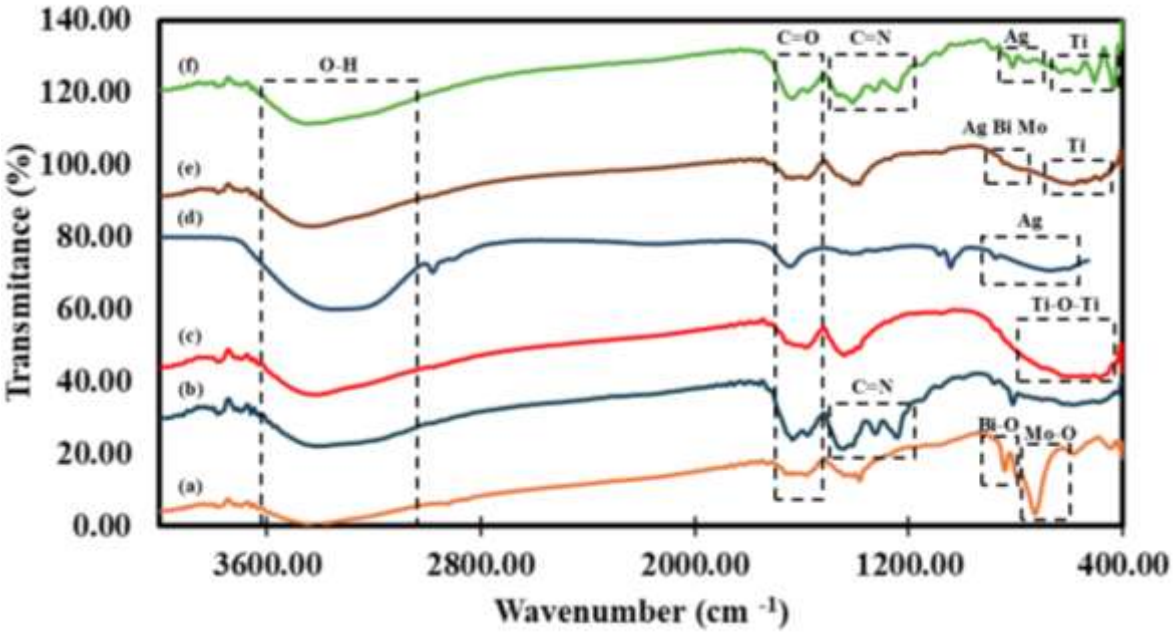

4.2.2 XRD analysis

XRD analysis was conducted to investigate the crystalline structure and phase composition of the synthesized samples. This is essential in confirming the successful formation of heterojunctions and the presence of individual components in ABMOT and AGCNT NC matrix. The diffraction patterns were compared with standards from the Joint Committee on Powder Diffraction Standards (JCPDS) files to identify the characteristic peaks corresponding to each phase. Additionally, shifts, broadening or disappearances of the peaks were analyzed to gain insights into the structural interactions among the components within the ternary heterostructures of ABMOT and AGCNT NCs.

The XRD patterns of Ag, Bi_2MoO_6, g-C_3N_4, TiO_2 and the ternary heterostructures of ABMOT and AGCNT are depicted in Figures 4.2 and 4.3, respectively. For individual samples of TiO_2 (Figures 4.2a and 4.3a), it was observed that characteristic peaks at 2θ = 25.4 °, 38.5 °, 48.1 °, 55.1 °, 63.0 ° (JCPDS 21-1272) correspond to anatase phase (101), (004), (200), (211), (204), and (220) crystal faces, respectively. The anatase phase of TiO_2 is well known to have the highest photocatalytic activity in comparison to the other polymorphs (Katal et al., 2020). This makes it suitable to be combined with other materials to further enhance its properties. Given the dominant formation of (101) crystal facets, this indicates

that the TiO_2 synthesized is thermodynamically stable and makes it favorable for long-term structural stability (Ye et al., 2013).

On the other hand, individual samples of AgNPs exhibited peaks of Ag (200) at 2θ = 44.6 °, Ag (220) and 2θ = 64.6 °, and Ag (311) at 2θ = 77.4 ° (JCPDS 04-0783) (Figure 4.2c and 4.3b). Similar peaks were observed in a past study by Aliero et al. (2024) in which the characteristic peaks of AgNPs that were synthesized with POME, also exhibited peaks corresponding to (200), (220), and (311). However, the major peaks at 2θ = 28 °, 32 °, and 38 ° were absent in the POME-derived AgNPs. This suggests that Ag species present are poorly crystalline or partially oxidized, potentially indicating the formation of Ag_2O or Ag-O related phases (Tan Sian Hui Abdullah et al., 2021). During the drying process, exposure to elevated temperatures may have disrupted the stabilizing interactions between AgNPs and POME-derived organic moieties, leading to structural disorder and reduced crystallinity, which in turn suppressed the appearance of distinct Ag^0 diffraction peaks.

Moreover, the diffraction peaks of g-C_3N_4 corresponded to a hexagonal crystal system (space group P31c), with peaks at 2θ = 27.5 ° and 38.3 ° (JCPDS 01-087-1522) which matched the planes (002) and (100), respectively (Figure 4.3c). The peak corresponding to the (002) plane indicates the interlayer stacking of aromatic s-triazine units, which formed a layer, graphitic-like structure that promotes π–π conjugation and facilitates charge carrier transport (Wudil et al., 2023). The notably intense (100) reflection suggests a high degree of in-plane structural ordering, likely due to enhanced periodicity within the polymeric framework (Muhmood et al., 2024). These XRD patterns of the g-C_3N_4 obtained coincide with FTIR spectra in which aromatic s-triazine units are detected, hence validating the succession of g-C_3N_4 formation with good structuring order and crystallinity.

Next, the diffraction peaks of pure Bi_2MoO_6 showed distinctive peaks around 2θ = 28.3 °, 32.5 °, 47.1 °, and 55.8 ° corresponding to (131), (200), (260) and (331) planes, respectively (Figure 4.2b). The XRD pattern suggests the formation of the orthorhombic Aurivillius phase of γ- Bi_2MoO_6 (JCPDS 21-0102). Thus, confirming the succession of crystalline Bi_2MoO_6. This particular phase is desirable because it has a greater capacity to capture visible light than its fluorite-structured counterparts, α-$Bi_2Mo_3O_{12}$ and β-$Bi_2Mo_2O_9$ (Lin et al., 2023).

Upon combining the individual components to form ABMOT and AGCNT ternary NCs, distinct changes were observed in their characteristic peaks. In the case of ABMOT

ternary NC, Ag peaks at 2θ = 44.6 ° (200) and 2θ = 64.8 ° (220) were detected, confirming that AgNPs were successfully deposited into the ternary NC matrix (Figure 4.2d). Similarly, all characteristic peaks of Bi_2MoO_6 and TiO_2 were retained, albeit with reduced intensity. This indicates the coexistence of different phases within the ternary system and reflects increased structural distortion, a typical feature of most NC systems.

A similar trend was observed in the AGCNT ternary NC, where the diffraction peaks of g-C_3N_4 and TiO_2 were preserved but with reduced intensity. However, a key distinction between the two ternary NCs was the form of Ag present. In the case of AGCNT ternary NC, peaks corresponding to typical metallic Ag were absent. However, a distinct peak at 2θ = 32.7 ° (111) corresponding to Ag_2O was present (JCPDS 031-1104) (Figure 4.3d). Based on this observation, it can be concluded that the variation in Ag phases between ABMOT and AGCNT NCs is attributed to the difference in the composite matrix. Past studies have shown that g-C_3N_4-based photocatalyst predominantly stabilizes Ag in the form of Ag_2O due to a more oxidative environment. Thus, the interaction of Ag^+ ions favors the formation of Ag_2O as compared to metallic Ag, allowing the AGCNT composite to benefit from p-n junction formation, which enhances the visible light absorption (Wang et al., 2022; Wu et al., 2015).

In contrast, when Bi_2MoO_6 is introduced into the NC matrix, the formation of metallic Ag is favorable, likely due to the narrow bandgap and efficient electron transfer which supported the full reduction of Ag^+ to Ag^0 (Lin et al., 2015; Wang et al., 2018). In general, the XRD analysis confirms the successful synthesis and crystallinity of each individual component and their respective incorporation into ABMOT and AGCNT ternary NCs. Furthermore, the difference in Ag species in ternary ABMOT and AGCNT highlights the critical influence of the composite matrix in forming varying species of Ag as a result of varying redox environments provided by Bi_2MoO_6 and g-C_3N_4, respectively. Overall, the XRD result validates the structural integration of each component into the desired ternary NC architectures.

Figure 4–2: XRD spectra of (a) TiO_2, (b) Bi_2MoO_6, (c) AgNP and (d) ABMOT NC

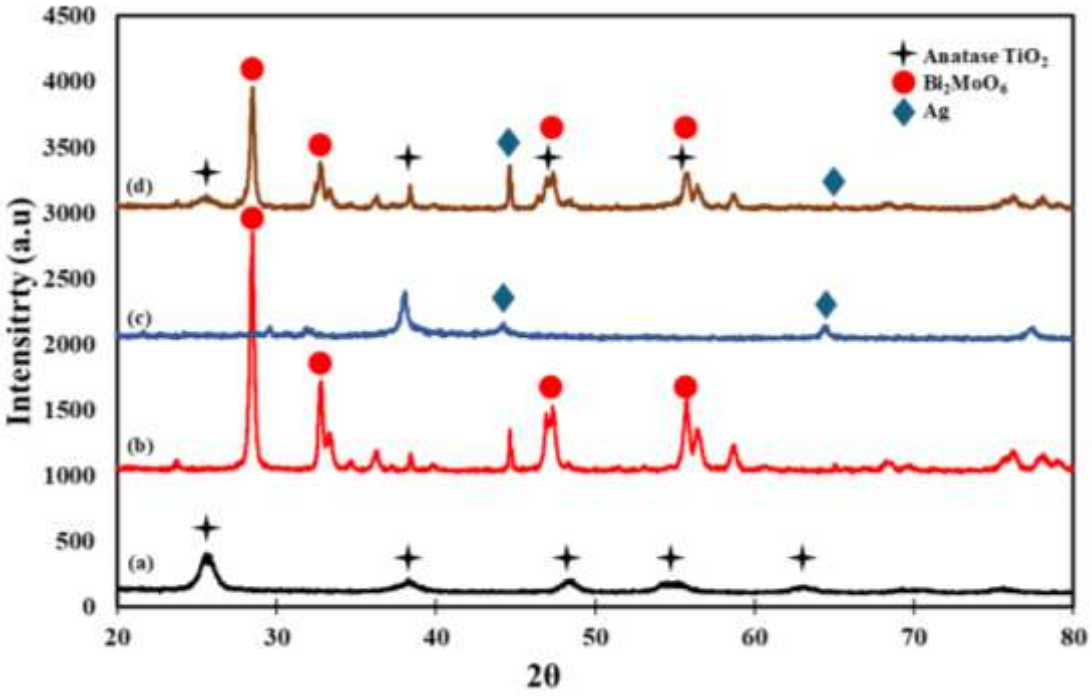

Figure 4–3: XRD spectra of (a) TiO_2, (b) AgNP, (c) g-C_3N_4 and (d) AGCNT NC

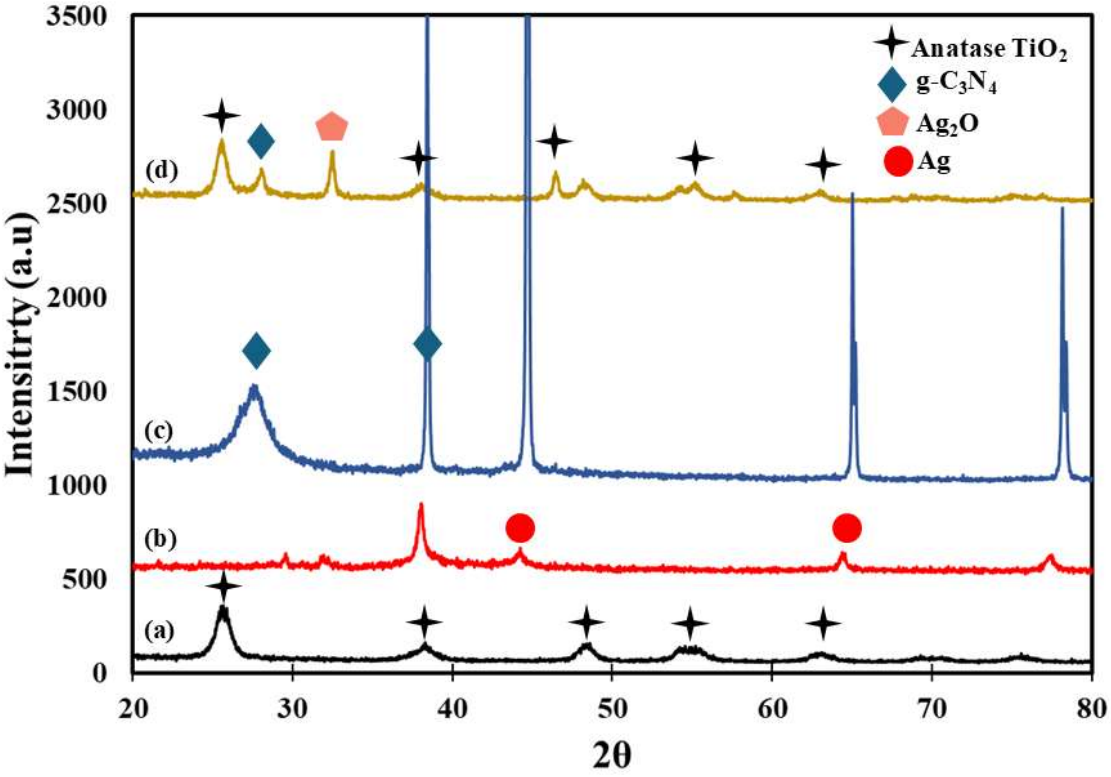

4.2.3 SEM-EDX analysis

To complement the structural insights provided by XRD analyses, further morphological and elemental characterization was carried out via SEM-EDX. This characterization step is essential to visually verify the successful incorporation of each component in the ternary heterostructures of ABMOT and AGCNT matrices. SEM images were acquired to observe morphological changes resulting from heterojunction formation in ABMOT and AGCNT ternary NC matrices, as shown in Figure 4.4. Moreover, elemental mapping aids in evaluating the homogeneity of ternary NC architecture. For Ag/TiO_2-based composites, morphology plays an important role in light scattering, active site accessibility, and the formation of effective interfacial contacts between the components (Ahmed et al., 2025; Khan et al., 2019).

The surface morphology of pristine TiO_2 synthesized via the sol-gel method exhibits smooth, spherical NPs that tend to agglomerate (Figure 4.4a), a common feature in nano-TiO_2 due to its high surface energy, van der Waals forces and hydrogen bonding, which drive the NPs to cluster together (Ahmad et al., 2021; Rachmaniar et al., 2024). Like pristine TiO_2, POME-derived AgNPs also form spherical NPs that tend to agglomerate (Figure 4.4b). The distribution of these AgNPs is largely influenced by bioactive molecules, as evidenced by the TPC and TFC analyses, where polyphenols and flavonoids act as capping agents to stabilize the aggregates. Similar results were also reported by Gan et al.(2012), who observed spherical POME-derived AuNPs with uniformly distributed aggregates. More recently, another study also reported that POME-derived AgNPs exhibited evenly distributed spherical NPs, stabilized by specific bioactive compounds such as ascorbic acid, gallic acid, and vanillic acid, which facilitated controlled particle size and shape (Aliero et al., 2025).

On the contrary, Bi_2MoO_6 formed very distinctive morphologies. Bi_2MoO_6 displayed nanoflake-like morphology, with thin plate-like structures that overlap each other (Figure 4.4c). Similar morphology of green hydrothermal synthesized perovskite Bi_2WO_6 was observed in a study by Kanwal et al., (2023). In their study, the perovskite nanomaterial was synthesized with the aid of *Azadirachta indica* leaves which facilitated controlled nucleation and prevented uncontrolled aggregation of the growing crystallites, thus allowing for the formation of plate-like nanostructures that aggregate to have a flower-like aggregate (Kanwal et al., 2023). In addition to forming stable AgNPs, the current study further highlights the ability of POME to be used in more complex synthesis systems, such as in the formation of perovskite-based materials. Next, g-C_3N_4 was observed to form sheet-like

morphology with loosely stacked layers and irregular edges (Figure 4.4d). Due to thermal polymerization, g-C_3N_4 forms nanosheets that are composed of s-triazine units. The formation of these stacked sheets validates the XRD from peaks of (002) plane attributed to s-triazine unit stacking, hence proving the succession of g-C_3N_4 formation.

In the ternary systems ABMOT and AGCNT, the formation of NCs resulted in a uniform dispersion of TiO_2 and AgNPs, which were well anchored to the surface of Bi_2MoO_6 and g-C_3N_4 (Figure 4.4e and 4.4f). The ternary composites appeared more compact and homogeneous, suggesting the successful assembly of components through microwave-assisted routes. This method provides a favorable environment for uniform dispersion and anchoring of the components by directly interacting with polar molecules (Matias et al., 2023). This enables an even removal of dispersants and allows for consistent nucleation throughout the system (Liu et al., 2020).

Figure 4–4: SEM micrograph of (a) TiO_2, (b) AgNP, (c) Bi_2MoO_6, (d) g-C_3N_4, (e) ABMOT, and (f) AGCNT.

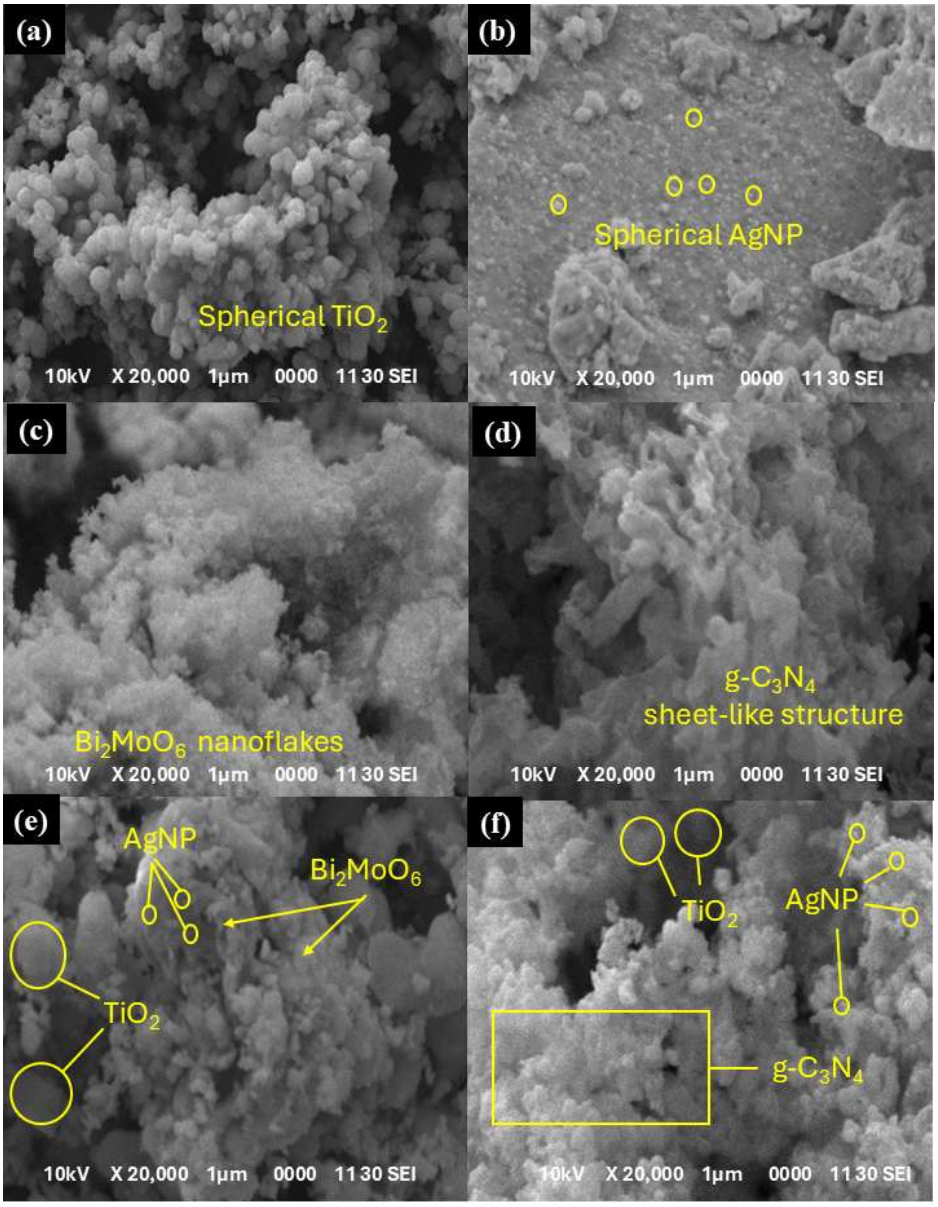

Further validation by EDX elemental mapping confirmed the uniform distribution of each element across the surfaces of ABMOT and AGCNT (Figure 4.5). Elemental mapping of ABMOT revealed a Ti to Bi and Mo ratio of approximately 1:0.3, with Ag forming around 2.97% by mass as shown in Table 4.2. In the case of AGCNT, although the C and N to Ti composition was expected to be approximately equal based on the 1:1 synthesis ratio, EDX mapping revealed actual ratios of 55.87%, 30.96%, and 1.88%, respectively (Table 4.3). The mass % of Ag in AGCNT was 4.89%.

Figure 4–5: EDX analysis and elemental mapping of (a) ABMOT and (b) AGCNT

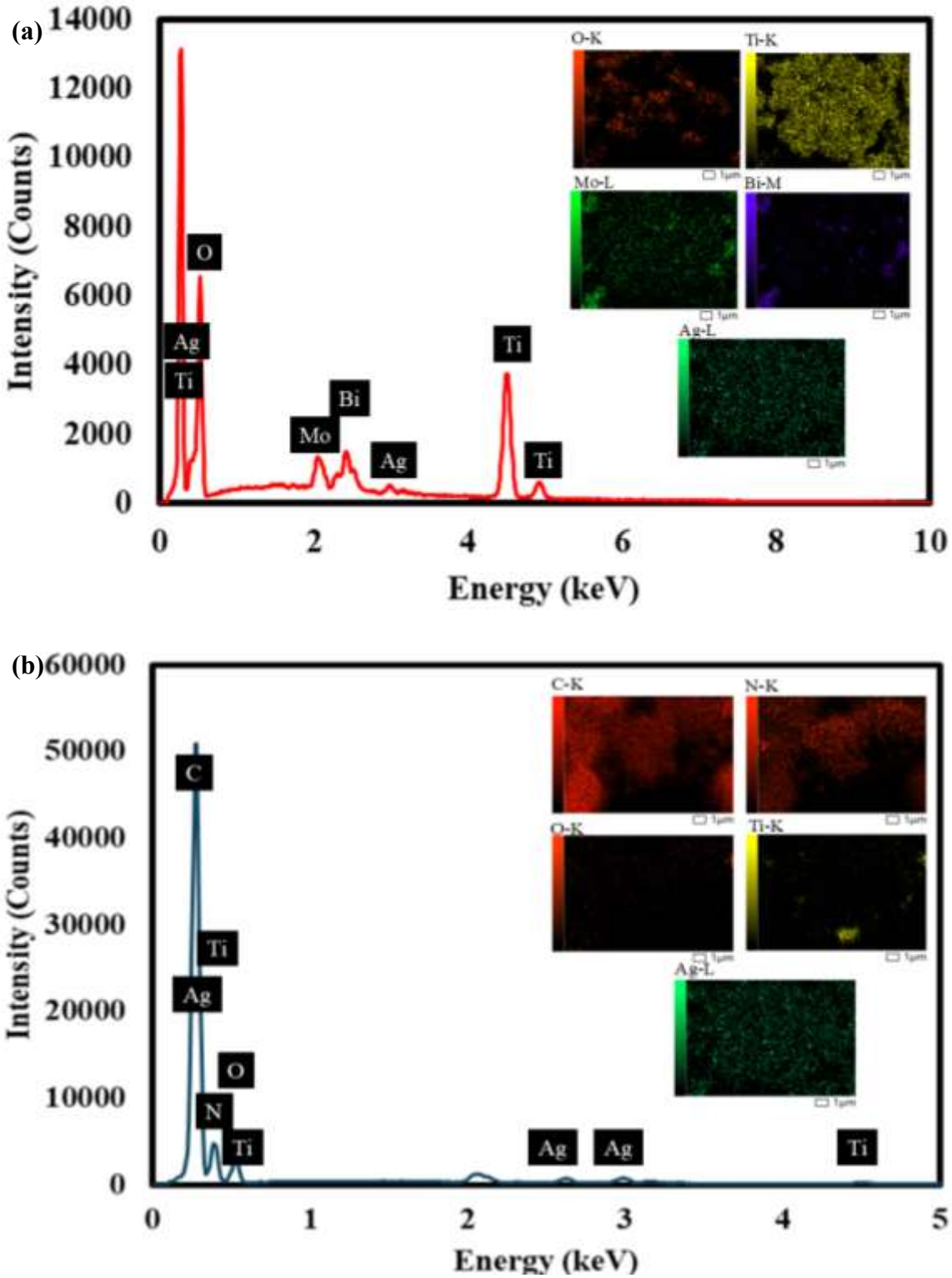

These data support the XRD findings of successful material integration. Nevertheless, it is worth noting that the overall composition and distribution of the elements may not directly translate into the mass percentage of elements detected through the EDX

mapping due to the possibility of surface coverage of different elements within the ternary system's matrix (Gui et al., 2023).

Table 4–2: Elemental composition of ABMOT and AGCNT NCs

Elements	Mass (%)	
	ABMOT	AGCNT
Ti	52.00±0.26	1.88±0.05
O	30.23±0.13	8.39±0.06
Ag	2.97±0.08	4.89±0.07
Bi	10.87±0.16	-
Mo	3.93±0.08	-
C	-	53.87±0.04
N	-	30.96±0.13

Note: "-" symbolizes elements that are not present in the composition of the material

4.2.4 Spectral analysis of UV-Vis DRS

The optical absorption behavior of the synthesized ABMOT and AGCNT NCs was evaluated using UV-Vis spectroscopy and Kubelka-Munk plot analysis, as shown in Figures 4.6 and 4.7. These results provide valuable insights into the materials' light harvesting capability and the modifications in their electronic structures resulting from heterojunction formation and the incorporation AgNPs.

In the ABMOT system (Figure 4.6a and 4.6b), pure TiO_2 showed a sharp absorption edge at around 400 nm with a bandgap of 3.00 eV, confirming that it mainly absorbs UV light. In contrast, Bi_2MoO_6 demonstrated broader absorption up to about 470 nm with a narrower bandgap of 2.45 eV, which aligns with its known ability to absorb visible light. The Bi_2MoO_6/TiO_2 composite displayed improved absorption between 300 and 450 nm, indicating effective heterojunction formation that enhances charge separation and broadens the absorption spectrum. Notably, the $Ag/Bi_2MoO_6/TiO_2$ NC had the highest absorption intensity, with a broad band extending beyond 500 nm. This improvement is mainly due to

the localized SPR effect of AgNPs, which strengthens local electromagnetic fields and extends light absorption into the visible range (Ahmadi et al., 2023; Yin et al., 2021).

Figure 4–6: UV-DRS spectra and (b) Kubelka-Munk plot of $Ag/Bi_2MoO_6/TiO_2$, Bi_2MoO_6/TiO_2 and its individual components

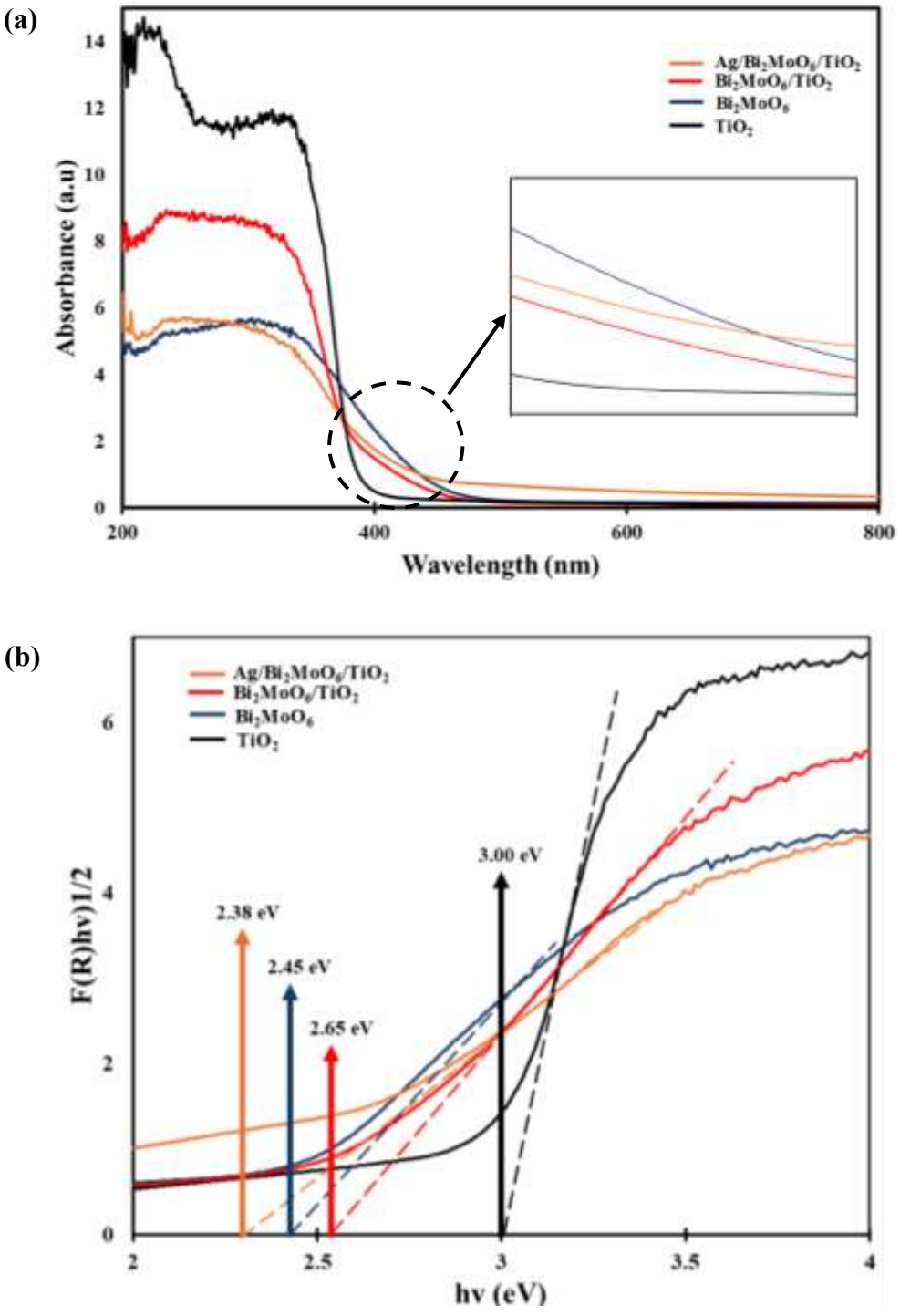

In the AGCNT system (Figures 4.7a and 4.7b), pure TiO_2 maintained its typical UV absorption, while g-C_3N_4 showed broad absorption up to around 450 nm, reflecting its π–π* electronic transitions and a measured bandgap of 2.60 eV. The TiO_2/g-C_3N_4 heterojunction (Figure 4.7) showed further improved absorption across the 300–450 nm range, confirming

a strong interfacial interaction and better light-harvesting ability. With the incorporation of AgNPs, the Ag/g-C_3N_4/TiO_2 (Figure 4.7) composite exhibited the highest overall absorption, particularly enhanced in the visible range due to the SPR effect of Ag. The slight increase in the apparent bandgap to 2.65 eV is likely attributed to the minor changes in the electronic environment and optical transitions induced by Ag, rather than intrinsic shifts in the semiconductor's band structure (Sui et al., 2020).

The slope of the Kubelka-Munk plot relates directly to the material's absorption coefficient and the nature of the electronic transitions. In both ABMOT and AGCNT composites, the addition of AgNPs produced steeper slopes than those observed in their respective heterojunctions without Ag. This suggests an enhanced absorption coefficient, indicating a greater probability of photon absorption and electronic transitions within the material (Volpp, 2023). The steeper slope also indicates improved crystallinity and fewer defect states within the composites, which enhance light-matter interactions (Tao et al., 2021). In the ABMOT system, the Bi_2MoO_6/TiO_2 heterojunction displayed a steeper slope compared to pure Bi_2MoO_6, suggesting that coupling with TiO_2 increased the overall electronic transition probabilities by providing more effective charge transfer pathways. Conversely, in the AGCNT system, the g-C_3N_4/TiO_2 composite exhibited a slope comparable to that of g-C_3N_4 alone; however, the incorporation of Ag further steepened the slope, highlighting Ag's role in promoting more efficient light absorption through plasmonic effects.

Overall, both the absorption spectra and Kubelka-Munk plot analyses confirmed that forming heterojunctions and incorporating AgNPs work together to enhance the optical properties of the ABMOT and AGCNT NCs. These improvements are expected to significantly boost their photocatalytic performance by enabling broader light absorption and more effective charge carrier generation

Figure 4–7: UV-DRS spectra and (b) Kubelka-Munk plot of Ag/g-C_3N_4/TiO_2, g-C_3N_4/TiO_2 and its individual components

(a)

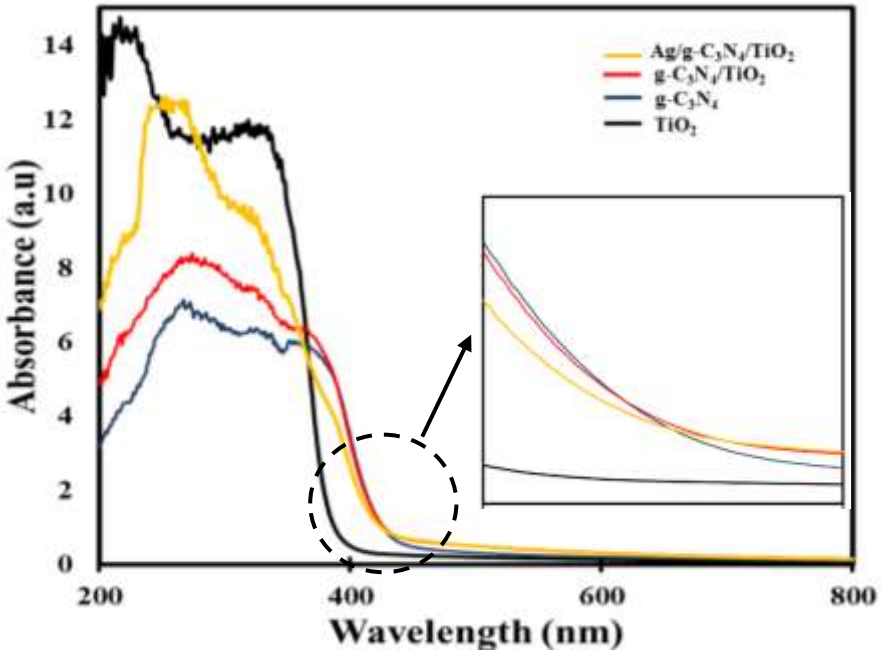

(b)

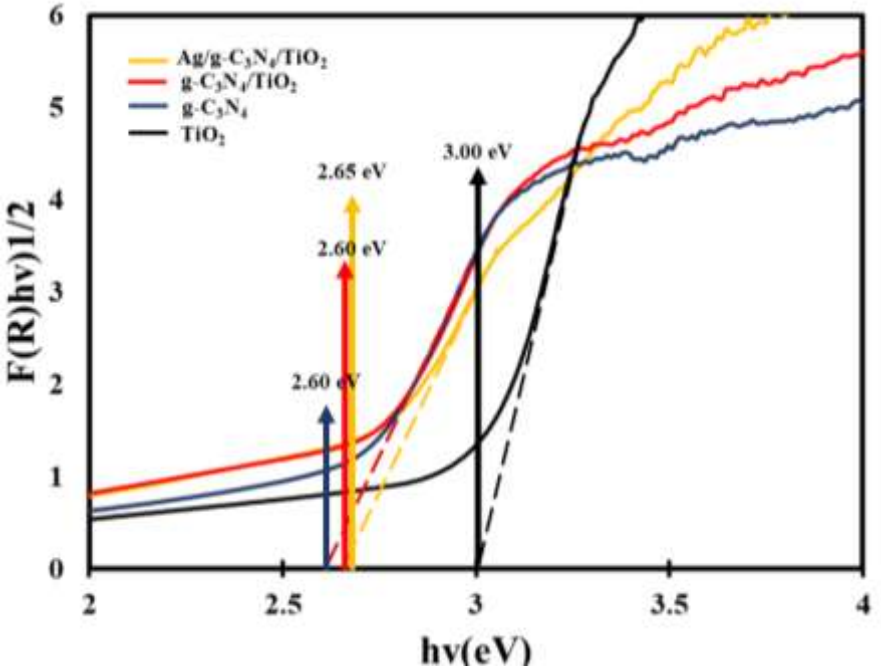

4.3 Photocatalytic performance of ABMOT and AGCNT

4.3.1 Parameters affecting the removal of OTC

4.3.1.1 Effect of catalyst dosage

Further investigation was conducted to determine the optimal dosage for ABMOT-AGCNT ternary NCs to degrade OTC under a xenon lamp as a visible-light source simulating sunlight for over 120 minutes (Figure 4.8). Varying catalyst loadings of 0.3 g/L, 0.6 g/L and 1.2 g/L were tested to evaluate the effect of catalyst dosages on the degradation process (Figure 4.8a and b). For both ternary composites, increasing the catalyst dosage from 0.3 g/L to 0.6 g/L enhanced the photocatalytic degradation of OTC. Specifically, OTC degradation increased from 88.3% to 97.2% for ABMOT and 48.7% to 81.3% for AGCNT. However, when the dosage increased to 1.2 g/L, a slight reduction in OTC degradation was observed for ABMOT and AGCNT at 91.8% and 76.6%, respectively.

This indicates that exceeding the optimal catalyst loading can saturate the photocatalyst surface, thereby reducing the overall removal efficiency. Although increasing the photocatalyst dosage up to a certain level can increase the number of reactive sites for photocatalysis, excessive loading could diminish the total surface area available for pollutant adsorption (Khader et al., 2024). Increasing the catalyst dosage beyond its optimal level can also increase opacity and light scattering, which in turn reduce the number of photons that can penetrate the catalyst surface, a crucial factor in initiating photocatalytic reactions (Santana et al., 2023).

Notably, ABMOT exhibited stronger adsorption than AGCNT during the dark phase, likely due to more abundant hydroxyl groups and the layered structure of Bi_2MoO_6 as observed in FTIR and SEM analysis. This results in an abundance of surface-active sites and facilitates stronger interactions with OTC molecules prior to visible light irradiation (Duong et al., 2024). In contrast, while AGCNT offers π–π interactions with aromatic antibiotic molecules, g-C_3N_4 is known to have a lower surface area and limited hydroxyl surface density (Muhmood et al., 2024). Hence, the weaker adsorption effect. The stronger initial adsorption of ABMOT increases pollutant concentration near active sites, thus allowing higher degradation of the adsorbed OTC on the surface of the ABMOT NCs. Therefore, the

optimal dosages for both ternary photocatalysts were determined to be 0.6 g/L and were chosen for further study.

Figure 4–8: Photocatalytic degradation of OTC with different dosages of (a) ABMOT and (b) AGCNT

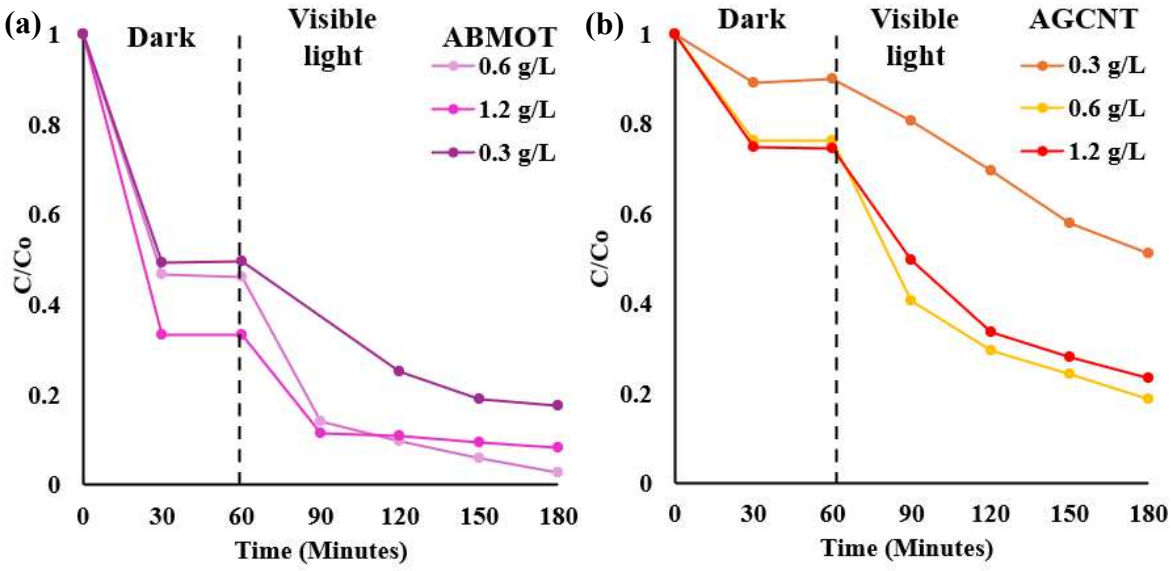

4.3.1.2 Effect of initial concentration

The effect of initial OTC concentration (10–20 mg/L) at a fixed dosage of 0.6 g/L was evaluated for both ternary NCs (Figure 4.9). Minimal changes were observed when the concentration increased from 10 to 15 mg/L, with ABMOT decreasing slightly from 97.2% to 93.5% and AGCNT from 81.3% to 80.3%. However, at 20 mg/L, AGCNT showed a marked decline in degradation efficiency, dropping sharply to 42.5%, contrary to ABMOT, which only decreased to 85.9%. The reduced photodegradation rate with increasing OTC concentrations could be due to excessive OTC loading on the photocatalyst surface, coupled with the accumulation of intermediates that block active sites and thereby suppress the formation of reactive oxygen species (ROS). A similar finding was also observed in a previous study involving the degradation of tetracycline hydrochloride by using Bi_2MoO_6/TiO_2-based photocatalyst, whereby the degradation efficiency declined from ~87.5% to 20.0% with the increasing initial concentration from 10 mg/L to 30 mg/L (Qi et al., 2025).

Furthermore, the dark adsorption phase also revealed a notable difference between the two photocatalysts at varying OTC concentrations. For ABMOT, a significant decrease

in the degradation rate was observed, particularly when the concentration was increased to 20 mg/L, further demonstrating that the layered structure of Bi_2MoO_6 and its higher hydroxyl density enable strong adsorption, allowing better removal of OTC even at high concentrations. Conversely, AGCNT shows weaker adsorption trends with increasing concentration, indicating the limited adsorption capacity. This is most evident at a concentration of 20 mg/L, where rapid saturation of surface-active sites restricts pollutant-catalyst interaction. Hence, the optimal initial concentration for the degradation of OTC was fixed as 10 mg/L.

Figure 4–9: Photocatalytic degradation of OTC with different initial concentrations for (a) ABMOT and (b) AGCNT

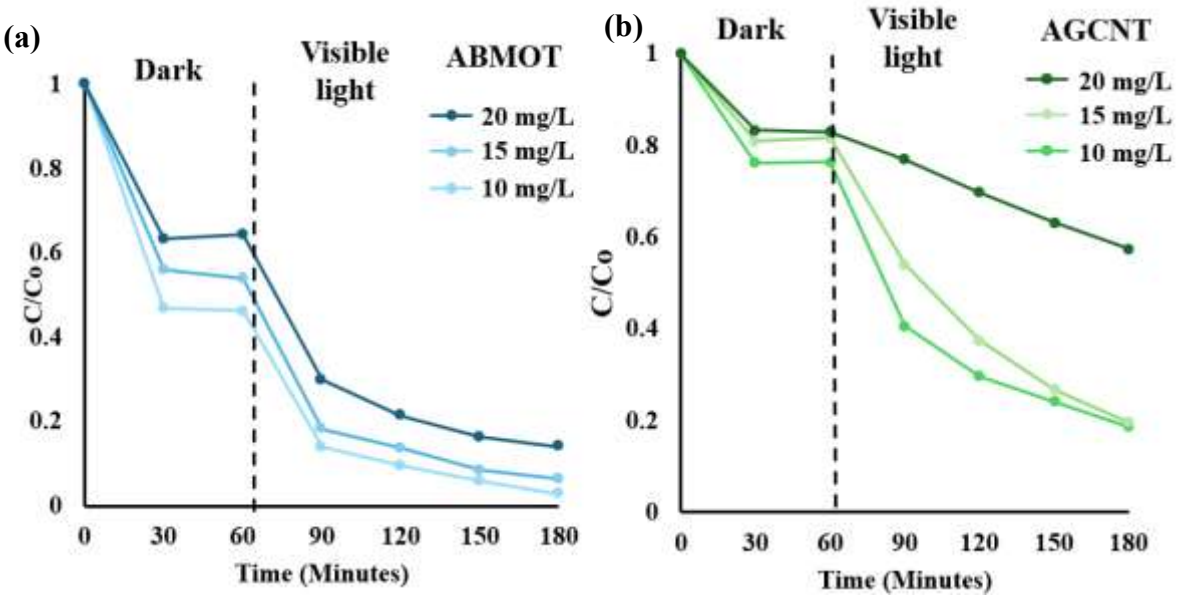

4.3.1.3 Recyclability potential of ABMOT and AGCNT

Recyclability study was conducted to determine the efficiency of the ABMOT and AGCNT ternary NCs in degrading OTC over 4 consecutive cycles (Figure 4.10). The stability of a photocatalyst is of utmost importance as it determines the scalability for larger industrial applications that require cost-effective processes. The recyclability study was conducted under optimized conditions, with ABMOT and AGCNT dosages of 0.6 g/L to treat 10 mg/L OTC for 120 minutes under visible-light irradiation. After 4 consecutive cycles, the degradation efficiency of AGCNT decreased slightly from 80.3% to 73.7% (Figure 4.10b) while ABMOT showed a minor reduction from 97.2% to 93.5% (Figure

4.10a). These results highlight the stability and efficiency of ternary ABMOT and AGCNT NCs.

Figure 4–10: Photocatalytic degradation of OTC by (a) ABMOT and (b) AGCNT after four cycles

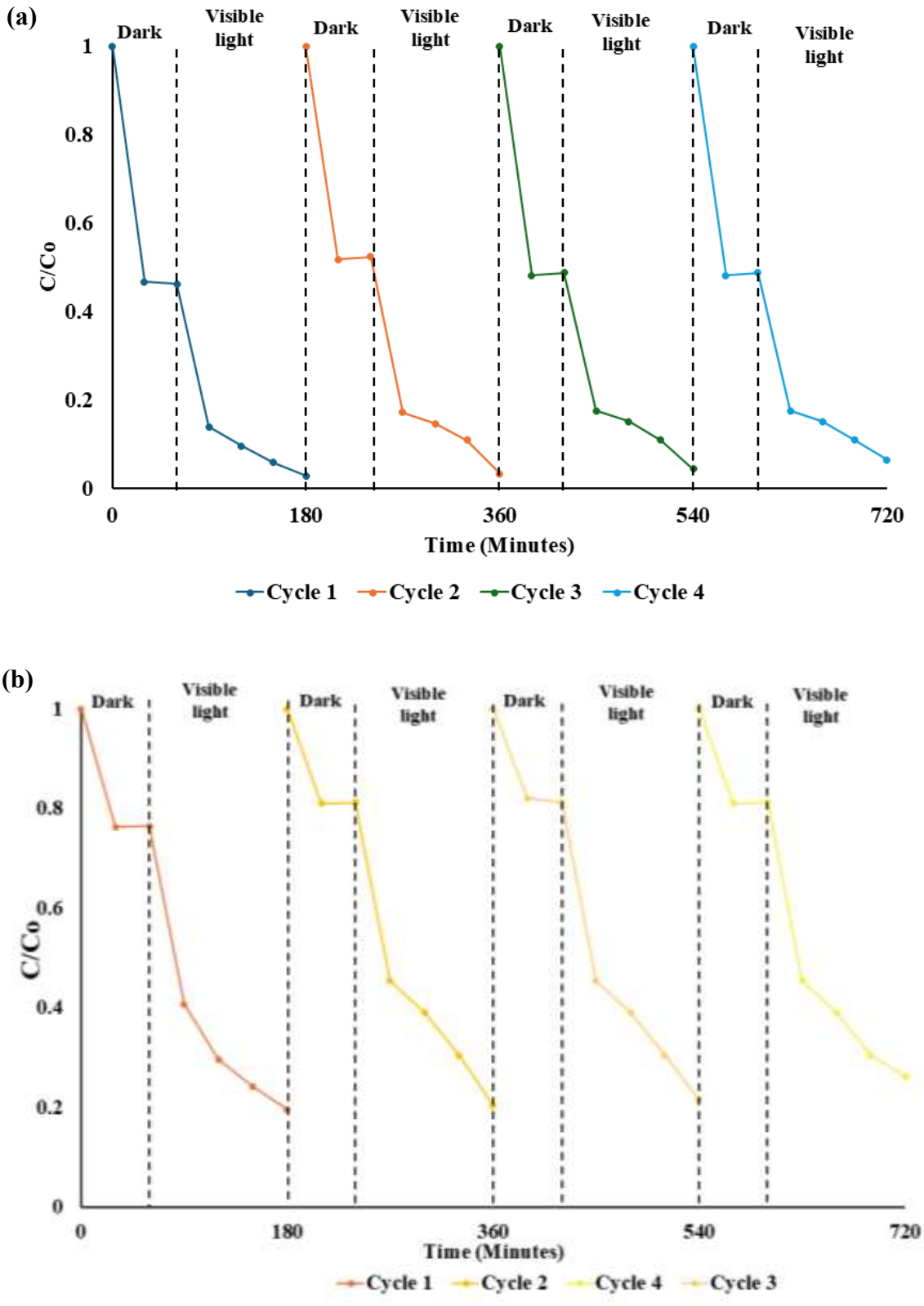

4.4 Antibacterial properties of AGCNT and ABMOT

The antibacterial properties of both ternary ABMOT and AGCNT were tested against gram-negative *E. coli* and gram-positive *S. aureus* via the disk diffusion method. Antibacterial activity was evaluated concerning the zone of inhibition (ZOI) induced by the photocatalyst (Figure 4.11). To evaluate the antibacterial activity, ABMOT and AGCNT were compared with their unary and binary counterparts at a fixed concentration. It was found that for all unary and binary samples of TiO_2, Bi_2MoO_6, g-C_3N_4, Bi_2MoO_6/TiO_2 and g-C_3N_4 /TiO_2, no measurable clear ZOIs were found, suggesting their negligible antibacterial properties. These results corroborate with past studies utilizing NCs containing TiO_2, Bi_2MoO_6 and g-C_3N_4 without the presence of other metal-based dopants or oxides in the ternary photocatalyst matrix (Ma et al., 2024; Vignesh et al., 2018). The main reason for this observation is due to the non-toxic nature of Ti, Bi and Mo-based oxides. In most cases, the antibacterial activity attributed to Ti, Bi and Mo-based metal oxides lie in the generation of reactive species to cause cell damage. However, in the disc diffusion method, the absence of light significantly dampens the antibacterial activity.

The presence of Ag in ABMOT and AGCNT produced clear ZOIs, confirming that the AgNPs induced antibacterial activity within the composite matrix. Ag is known to exhibit antibacterial properties due to the dissolution of Ag^+ ions, which readily attack cell membranes of microbes (Anees Ahmad et al., 2020). Increasing the Ag dosage from 1% to 10% increased the ZOI, with ABMOT increasing from 6.23 ± 1.05 mm to 13.68 ± 0.36 mm against *E. coli*, while AGCNT increased from 7.00 ± 0.48 mm to 8.43 ± 0.63 mm (Figure 4.11a). In the case of *S. aureus*, increasing Ag content in ABMOT yielded similar results with an increase in ZOIs from 7.35 ± 0.66 mm to 10.31 ± 1.07 mm, while AGCNT showed an increase from 7.6 ± 0.65 mm to 9.26 ± 0.40 mm (Figure 4.11b).

These results suggest that the antibacterial activity is predominantly driven by AgNPs, which likely enhance oxidative stress and disrupt bacterial cell membranes, thereby disrupting essential cellular functions and leading to cell death (Bahadur et al., 2016; Chen et al., 2013). Additionally, the antibacterial modes of action between the two ternary composites differ, as reflected in their varying ZOIs. Compared to AGCNT, ABMOT exhibited stronger antibacterial activity, which could be due to the higher rate of Ag dissolution resulting from Ag dispersion in the NC matrix.

Figure 4–11: Antibacterial activity of ABMOT and AGCNT against (a) gram-negative *E. coli* and (b) gram-positive *S. aureus* bacteria.

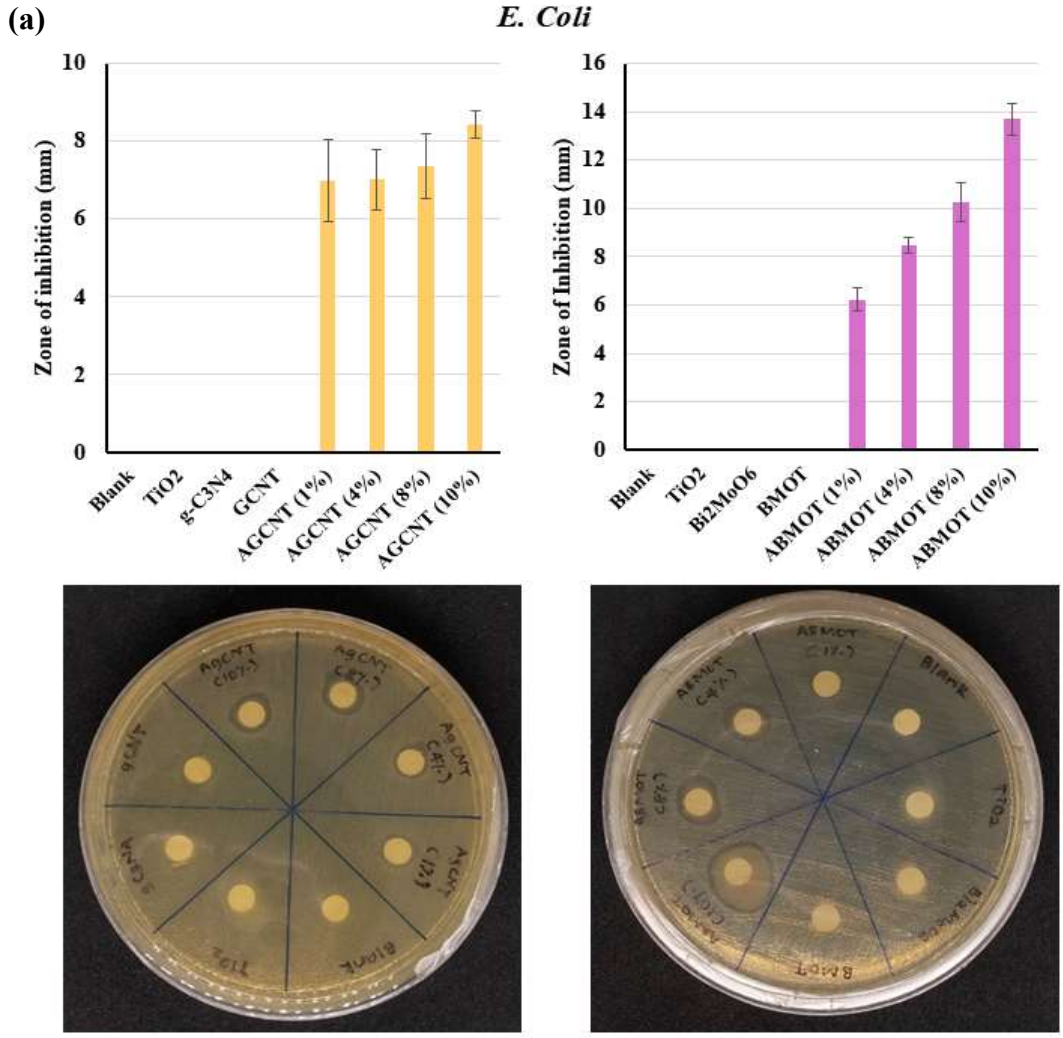

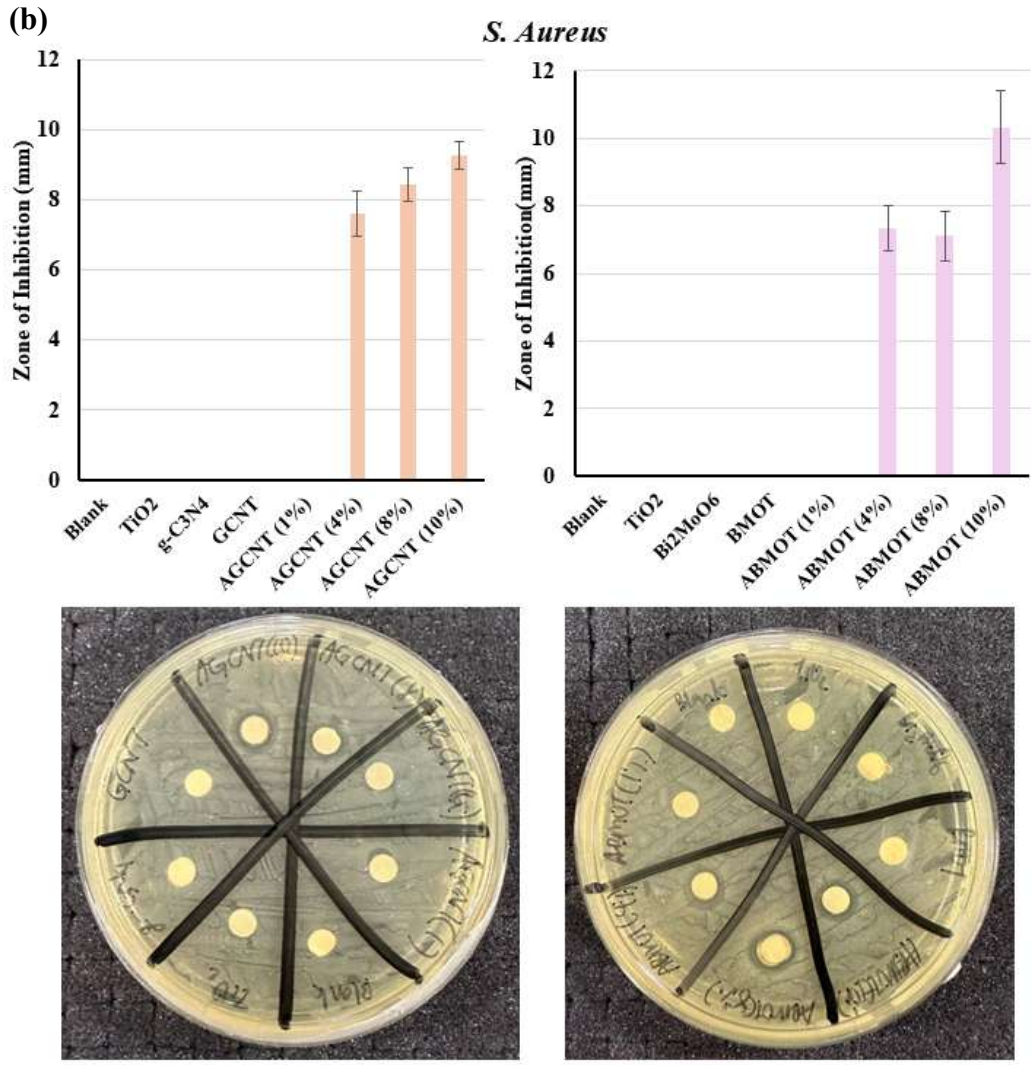

Moreover, a study on the effect of catalyst dosage on antibacterial activity was also conducted to determine the optimal dosage needed for bacterial inhibition (Figure 4.12). For both ABMOT and AGCNT samples, an increase in the catalyst dosage led to larger ZOIs. Nevertheless, in the case of AGCNT, the ZOI against gram-negative *E. coli* began to decline once the dosage exceeded 8 g/L (Figure 4.12). A similar trend was observed for ABMOT when the dosage exceeded 6 g/L, though the ZOI increased again up to 10 g/L. This could be attributed to the saturation point being reached, which limited the interactions between nanomaterials and bacterial cells. On the contrary, when similar conditions were conducted with gram-positive *S. aureu*s, a proportional relationship between concentration and ZOIs was observed. This is because higher concentration of nanomaterials is needed for a more effective disruption of bacterial activities, as gram-negative bacteria possess a thicker peptidoglycan layer compared to gram-positive bacteria (Dhanalekshmi et al., 2013). From a collective perspective, the overall photocatalytic performance and antibacterial activity of

both ABMOT and AGCNT ternary composites have been shown to be promising. Therefore, application of these ternary NCs was applied to a membrane matrix to study how they perform as photocatalytic membranes.

Figure 4–12: Effect of catalyst dosage on antibacterial activity by ABMOT and AGCNT against (a) gram-negative *E. coli* and (b) gram-positive *S. aureus* bacteria.

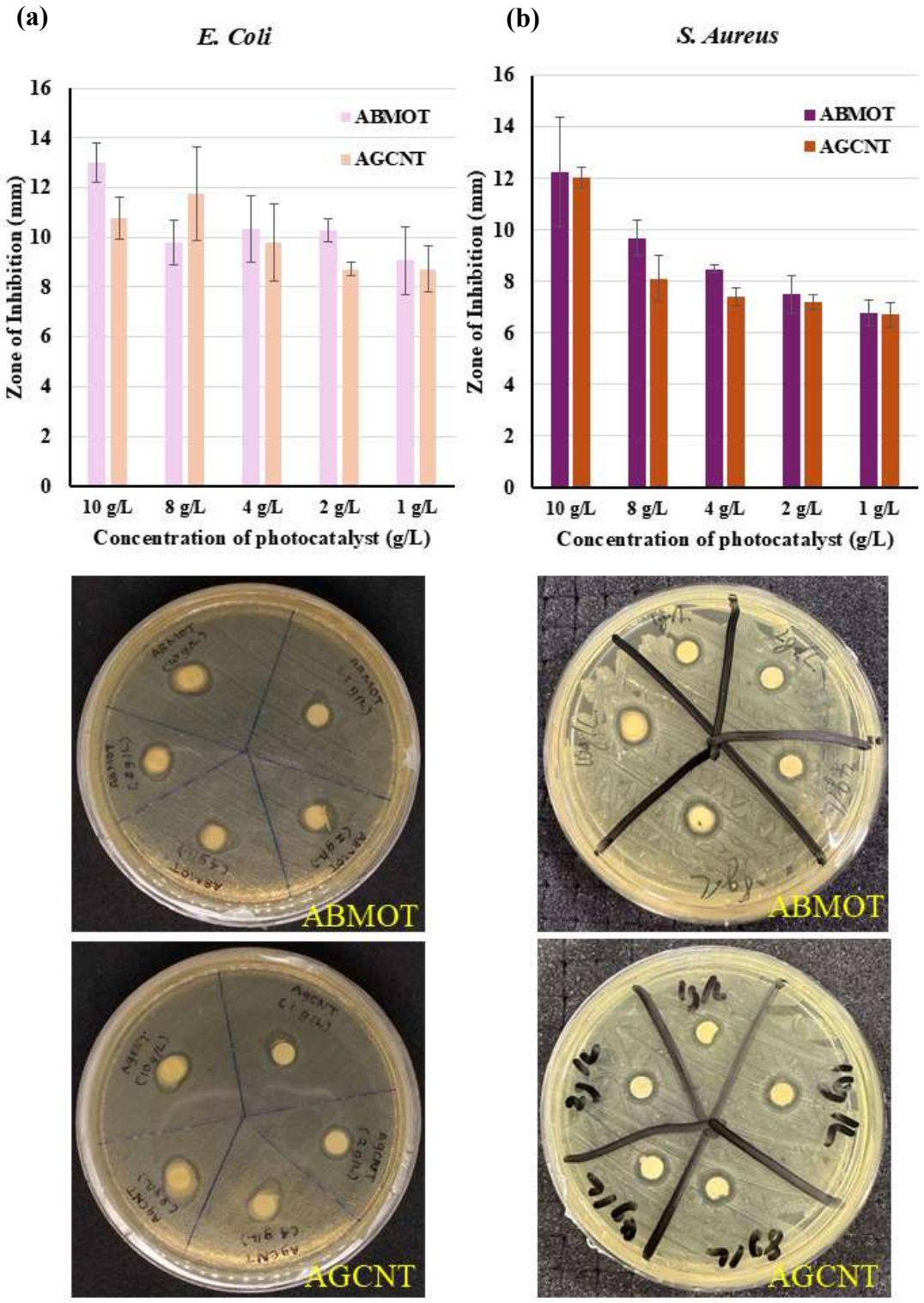

4.5 Immobilization of ABMOT and AGCNT into PAN membrane

4.5.1 Characterization of membranes

4.5.1.1 FTIR spectra

To investigate the physicochemical changes upon NC incorporation, FTIR analysis was employed to evaluate the chemical interactions and functional group retentions of NCs within the membrane matrix. Comparison between bare PAN membranes, ABMOT@PAN and AGCNT@PAN membranes were carried out within the range of 400 – 4000 cm^{-1} as observed in Figure 4.13. All samples displayed characteristic PAN absorption bands (Figure 4.13a), characteristic bands at ~2242 cm^{-1} (–C≡N stretching), ~1450 cm^{-1} (C–H bending), and ~3400 cm^{-1} (O–H stretching). Upon integration of ABMOT (Figure 4.13b) and AGCNT NCs (Figure 4.13c), slight shifts and changes in transmittance intensity were observed in the regions around 1630 cm^{-1} and 1000–700 cm^{-1}. These alterations suggest interactions between PAN polymer chains and the NCs' surface functionalities (Hartati et al., 2022). For instance, the broad band around 3400 cm^{-1}, associated with O–H bending, showed enhanced intensity in the ABMOT@PAN and AGCNT@PAN samples, possibly due to increased surface hydroxylation from the incorporated metal oxides. In the fingerprint region (~700–1000 cm^{-1}), additional features may correspond to stretching vibrations of metal–oxygen (M–O) bonds from Bi–O, Mo–O, Ti–O, or Ag–O linkages, further supporting successful NC integration. The C=N peaks associated with s-triazine stacking units in AGCNT@PAN are not clearly distinguishable, as they overlap with the PAN -C=N bending vibrations.

This result confirms chemical interactions between NCs and PAN within the NC membrane matrices, thereby validating the succession of ternary ABMOT and AGCNT NCs within PAN membranes. These modifications are expected to enhance membrane properties such as hydrophilicity and permeability properties of NC membranes (Sahu et al., 2023).

Figure 4–13: FTIR spectra of (a) PAN, (b) ABMOT@PAN and (c) AGCNT@PAN membranes

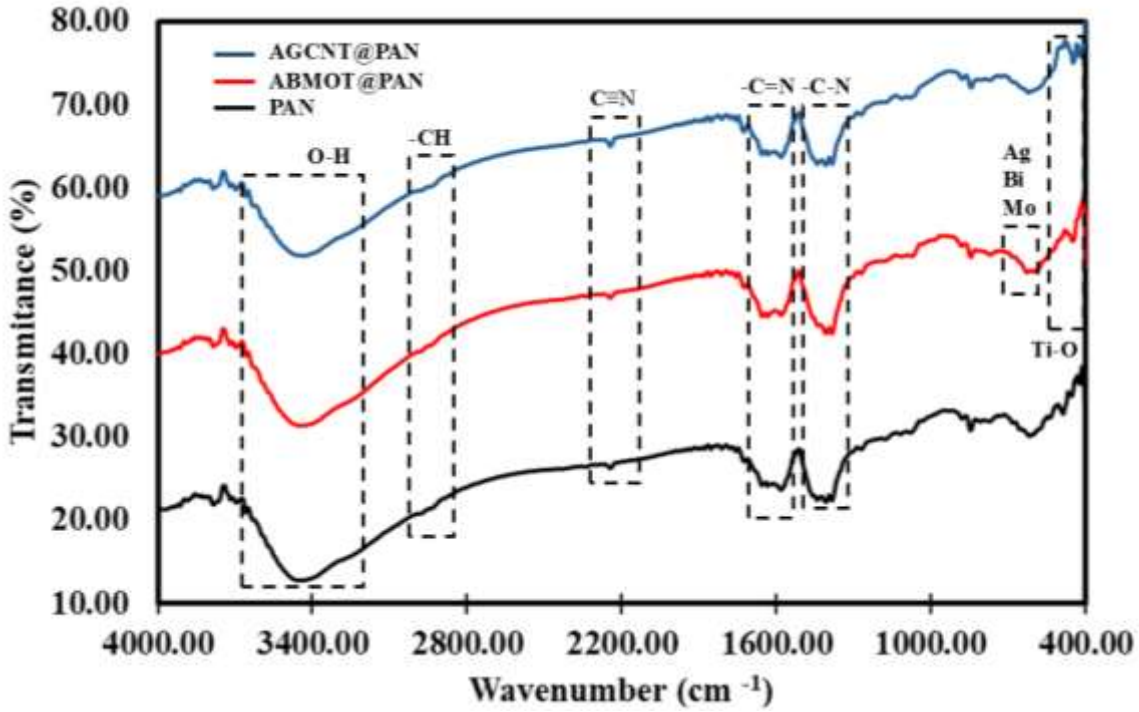

4.5.1.2 SEM-EDX analysis

Further validation of ternary NC incorporation in the PAN membrane was achieved through SEM-EDX analysis (Figure 4.14). The bare PAN membrane exhibited a relatively smooth, featureless surface, typical of pristine PAN prepared via phase inversion, with no visible particulate deposits or irregular surface features (Figure 4.14a). This smoothness indicates the formation of a uniform polymer film in the absence of NC additives (Xie et al., 2023).

The 1 wt% AGCNT@PAN membrane resulted in a noticeably rougher surface with fine granules distributed across it, suggesting that the NC particles were successfully embedded within and partially exposed on the membrane surface (Figure 4.14b). In contrast, the 1 wt% ABMOT@PAN membrane displayed discrete spherical particles and aggregates that were more clearly distinguishable compared to AGCNT@PAN (Figure 4.14c). These protrusions are attributed to the relatively larger particle size and agglomeration tendency of ABMOT, which may cause surface deposition during the casting and solvent exchange stages.

Increasing the NC loading to 2 wt% further intensified the observed surface texturing for both composites. The 2 wt% AGCNT@PAN sample exhibited more pronounced surface undulations and irregular granular coverage, indicating increased NC migration toward the surface (Figure 4.14d). The 2 wt% ABMOT@PAN membrane surfaces appeared even more irregular, with a combination of textured wave-like features and larger exposed particle clusters (Figure 4.14e).

Figure 4–14: SEM micrograph of (a) PAN, (b) 1% AGCNT@PAN, (c) 1% ABMOT@PAN, (d) 2% AGCNT@PAN and (e) 2% ABMO@PAN

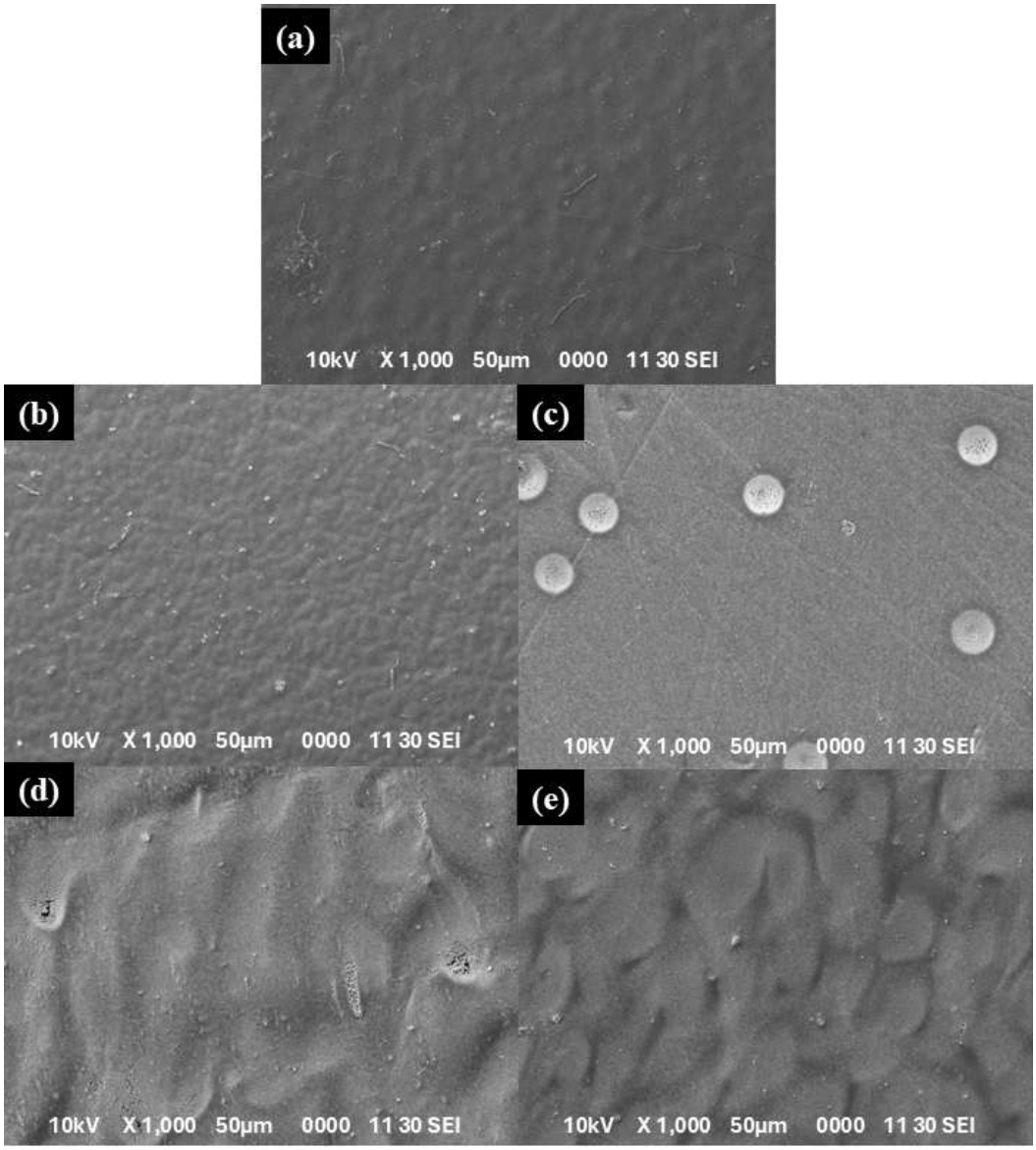

Furthermore, EDX elemental mapping verified the presence of each element in both ABMOT@PAN and AGCNT@PAN NC membranes (Figure 4.15). The absence of some elements, such as Ti within AGCNT@PAN and Ag/Bi within ABMOT@PAN membranes,

is attributed to the low amount of NCs compared to the mass of PAN in the NC-membrane matrix (Quadri et al., 2023). Nevertheless, trace amounts are still detected in the system, confirming the sequence of NC incorporation. A summary of the elemental composition is shown in Table 4.3.

Figure 4–15: EDX analysis and elemental mapping of (a) ABMOT@PAN and (b) AGCNT@PAN membranes

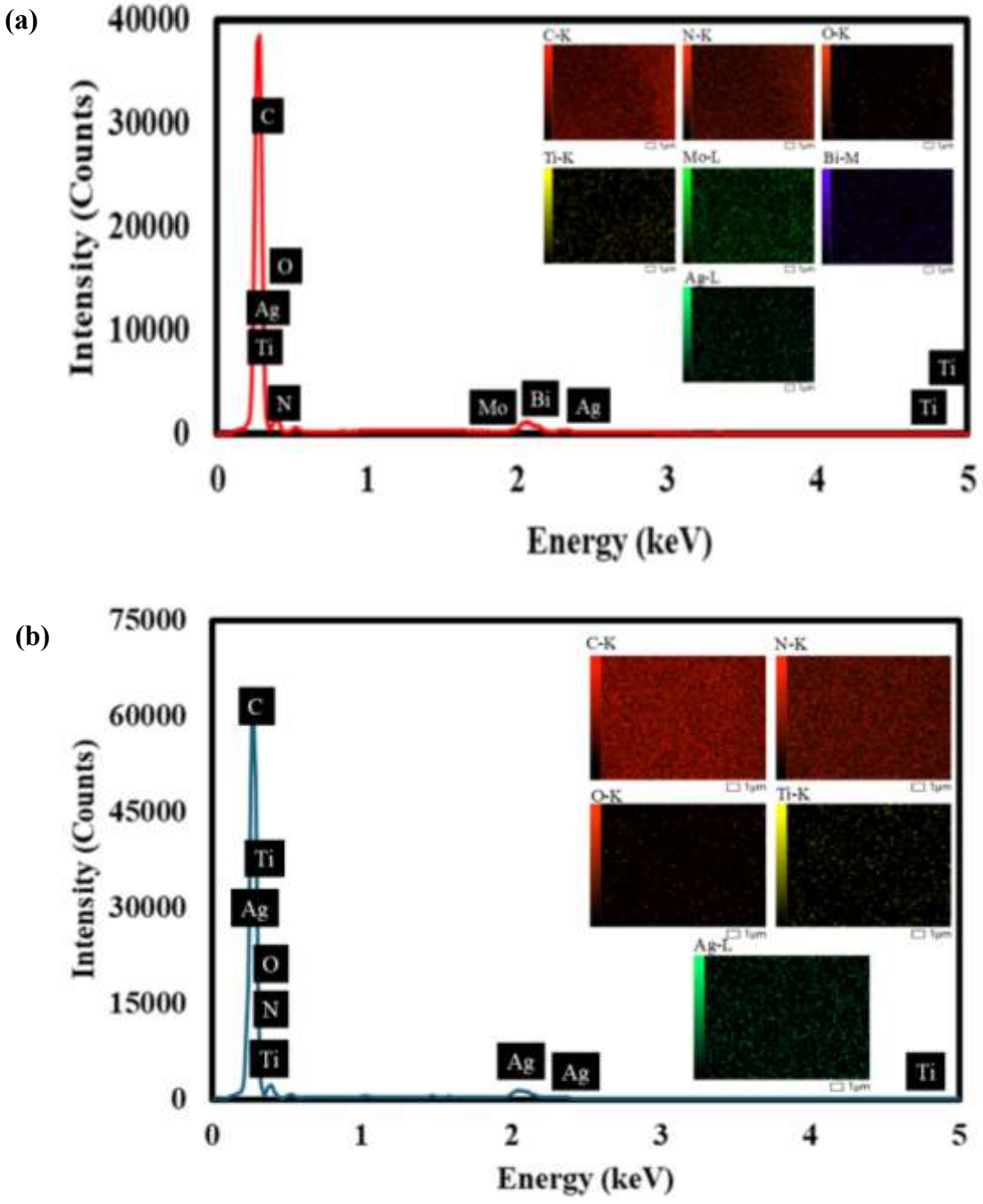

Overall, the SEM-EDX observations confirm that incorporating NCs into PAN membranes alters the surface morphology, with increasing NC content leading to greater

roughness and more pronounced surface features. These changes are more pronounced for ABMOT-loaded membranes compared to AGCNT-loaded membranes, likely due to differences in particle morphology, size distribution, and surface chemistry between the two NC types. The increased surface roughness is expected to enhance surface hydrophilicity and potentially improve photocatalytic activity under light exposure (Vatanpour et al., 2024).

Table 4–3: Elemental composition of ABMOT@PAN and AGCNT@PAN membranes

Elements	ABMOT@PAN	AGCNT@PAN
	Mass%	Mass %
Ti	0.24±0.04	Not detected
O	2.92±0.05	2.38±0.04
Ag	Not detected	0.22±0.04
Bi	Not detected	-
Mo	2.45±0.06	-
C	72.45±0.07	74.33±0.05
N	21.94±0.17	23.06±0.15

Note: "-"symbolizes elements that are not present in the composition of the material

4.5.2 Permeation test of NC membranes

Pure water flux (PWF) analysis was then carried out to evaluate the permeability of bare PAN and NC-integrated PAN membranes (Figure 4.16). The bare PAN membrane exhibited the lowest flux value of 129.17 $L \cdot m^{-2} \cdot h^{-1}$, attributable to its relatively smooth and less porous surface morphology observed in SEM images (Figure 4.14a). The incorporation of NCs resulted in a consistent increase in PWF across all tested membranes. With a 1 wt% loading, ABMOT@PAN achieved a flux of 144.39 $L \cdot m^{-2} \cdot h^{-1}$, whereas AGCNT@PAN recorded 142.21 $L \cdot m^{-2} \cdot h^{-1}$. Increasing NC loading to 2 wt% further enhanced permeability, with ABMOT@PAN reaching 163.48 $L \cdot m^{-2} \cdot h^{-1}$ and AGCNT@PAN peaking at 170.94 $L \cdot m^{-2} \cdot h^{-1}$. The increase in flux with higher NC loading is attributed to the increased surface roughness and hydrophilicity imparted by the NCs, which promote efficient water transport pathways (Ramon & Hoek, 2013). The comparatively higher PWF of AGCNT@PAN (2

wt%) suggests that the sheet-like morphology of g-C_3N_4 promotes better water channel formation and interfacial compatibility within the PAN matrix.

Figure 4–16: Pure water flux of pure PAN, ABMOT@PAN and AGCNT@PAN membranes

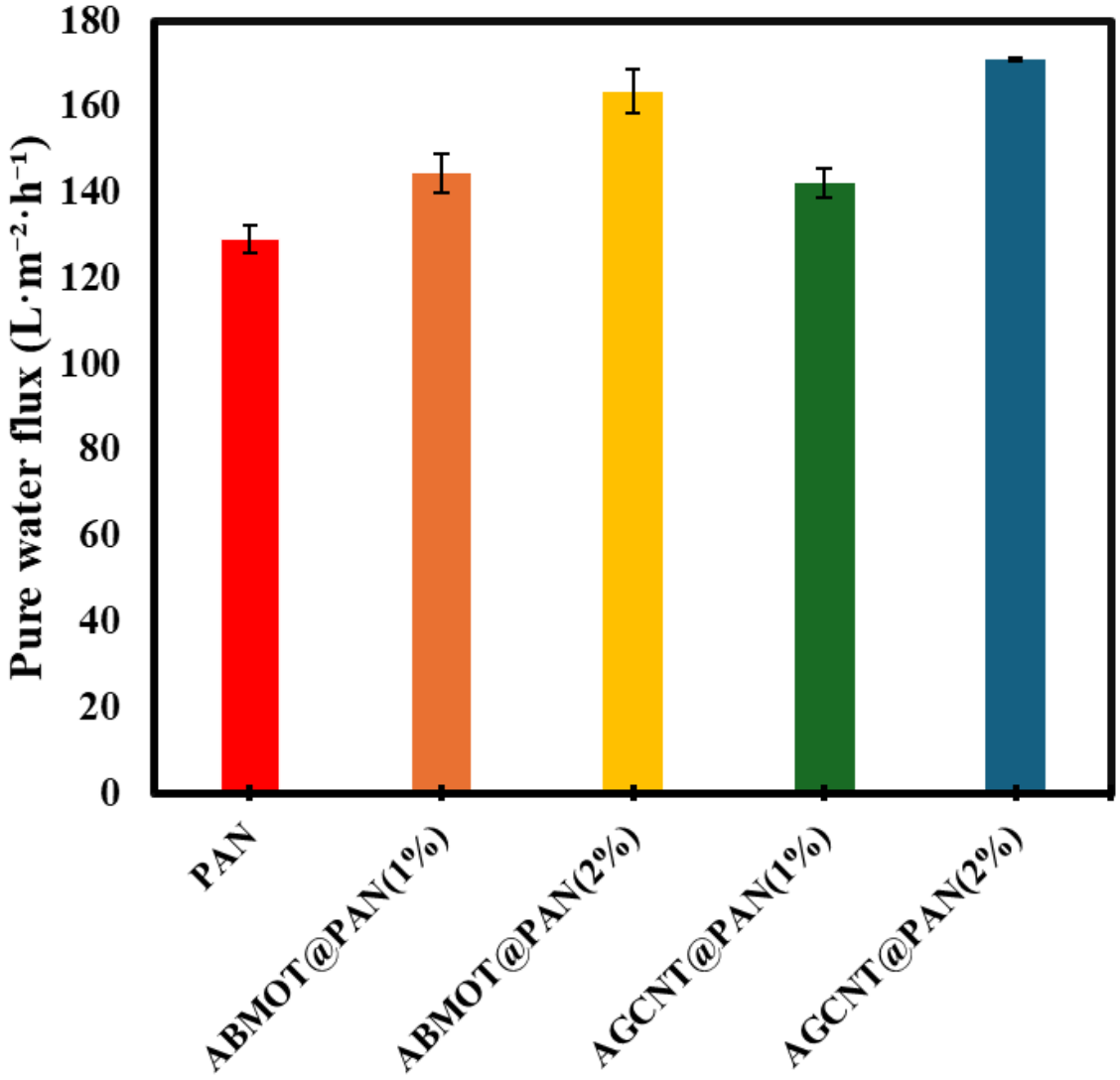

Rejection rate testing (Figure 4.17) revealed that bare PAN had the lowest contaminant removal efficiency (44.88%). The incorporation of NCs improved the rejection performance, with ABMOT@PAN achieving 72.30% at 1 wt% and 85.69% at 2 wt%, while AGCNT@PAN achieved 82.57% and 90.34% at the same loadings. The superior rejection performance of AGCNT-based membranes is attributed to their higher hydrophilicity, greater surface active site density, and improved NC dispersion, which collectively enhance size-exclusion and adsorption mechanisms (Arundhathi et al., 2024; Wu et al., 2022).

Figure 4–17: OTC rejection rate of pure PAN, ABMOT@PAN and AGCNT@PAN membranes

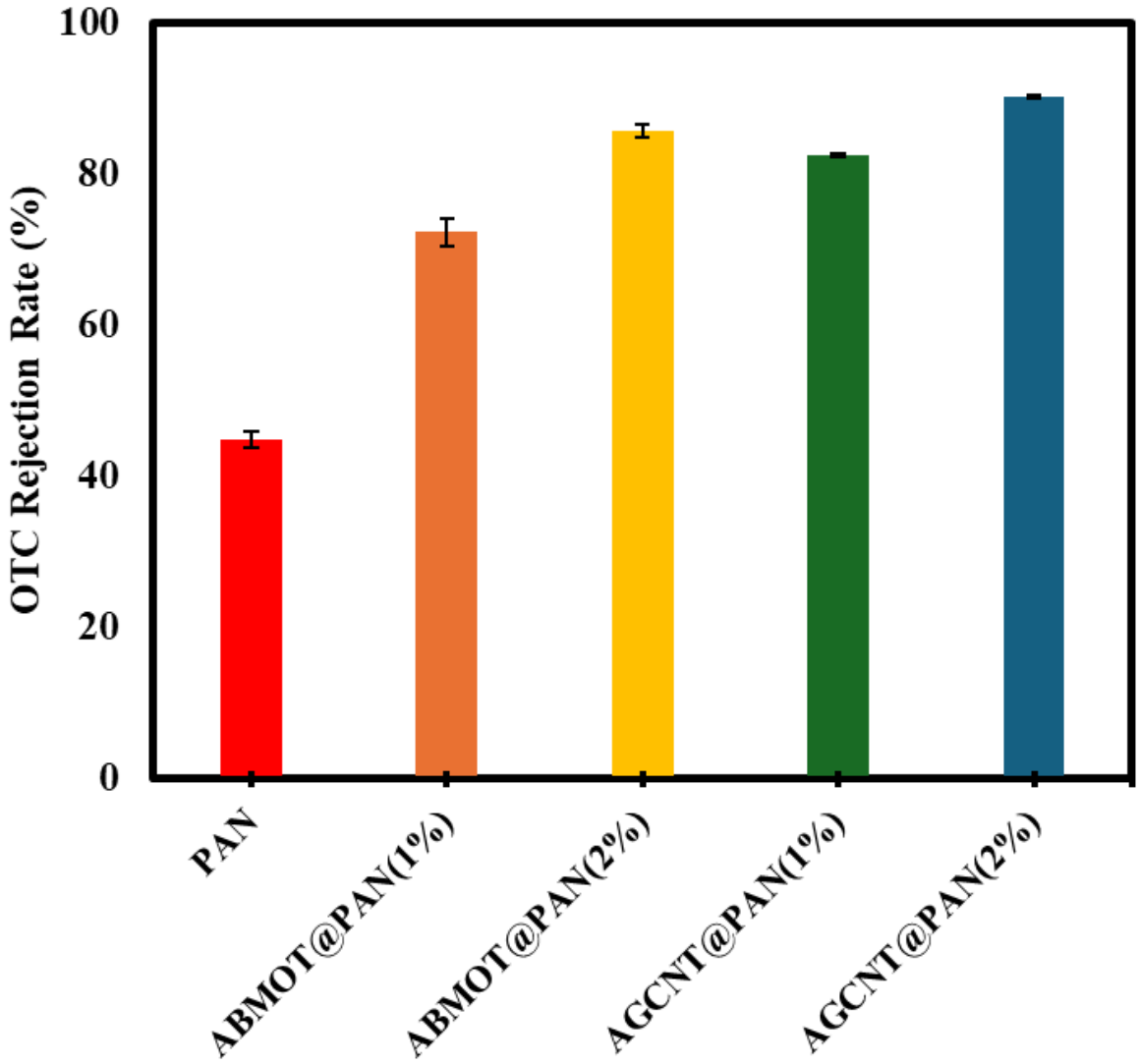

Although the NC@PAN membranes in this study were tested solely under filtration conditions and not for photocatalytic degradation, the superior performance of AGCNT in its powdered form suggests that, if integrated into photocatalytic membrane systems, AGCNT@PAN could potentially achieve higher contaminant removal rates while maintaining favourable permeability. This alignment between powdered catalyst activity and membrane separation efficiency highlights the potential of AGCNT as a more effective NC for multifunctional water treatment applications compared to ABMOT.

CHAPTER 5:

CONCLUSIONS

5.1 Conclusion

This study successfully synthesized ABMOT and AGCNT NCs via a POME-induced, microwave-assisted green synthesis approach, enabling rapid, energy-efficient formation of well-crystallized ternary heterojunctions using POME as a renewable reducing agent. This method reduced reaction time to minutes, avoided hazardous chemicals, and demonstrated a sustainable route for producing advanced photocatalysts.

Excellent photocatalytic performance was achieved through matrix-controlled silver speciation, as confirmed by XRD, FTIR, and SEM–EDX analyses. In the ABMOT system, Ag was predominantly present in the metallic state (Ag^0), likely due to favorable interfacial electron transfer and charge trapping at the Ag–Bi_2MoO_6/TiO_2 interfaces, which helped stabilize Ag^0 during synthesis and photocatalytic operation. In contrast, in the AGCNT system, Ag was mainly stabilized as Ag_2O, influenced by the oxidative surface environment of g-C_3N_4 and its interactions with oxygen-containing species, leading to the formation of Ag_2O and p–n heterojunctions with TiO_2. These heterostructures enhanced charge separation and light absorption, resulting in higher degradation efficiency at lower to moderate OTC concentrations. These complementary trends highlight that the composition of the composite matrix and interfacial interactions play a key role in Ag speciation and photocatalytic performance under different application conditions.

The incorporation of NCs into PAN membranes via the phase-inversion method further improved their functional performance. FTIR confirmed the introduction of hydrophilic functional groups, while SEM imaging revealed increased surface roughness, and EDX mapping showed a uniform distribution of the NCs across the membrane surface. These structural changes led to substantial improvements in pure water flux and rejection compared with bare PAN. AGCNT@PAN (2%) achieved the highest PWF (170.94

$L \cdot m^{-2} \cdot h^{-1}$) and rejection (90.34%), while ABMOT@PAN (2%) maintained a high PWF (163.48 $L \cdot m^{-2} \cdot h^{-1}$) with slightly lower rejection (85.69%), confirming that NC integration significantly enhanced both permeability and selectivity.

When comparing powdered and immobilized samples for OTC removal, powdered ABMOT and AGCNT showed higher intrinsic degradation rates because they were directly suspended in the reaction medium, ensuring maximum light exposure and catalyst–pollutant interaction. However, immobilized NCs in PAN membranes still achieved effective degradation while offering operational advantages, including ease of recovery, reduced post-treatment separation steps, and potential for continuous-flow applications. Although photocatalytic activity was slightly reduced in the immobilized form due to a lower exposed surface area, the membranes demonstrated stable performance and practical applicability, especially for scalable water treatment systems.

In summary, the research demonstrated the synergistic integration of green synthesis, matrix-optimized photocatalytic performance, and membrane technology to produce multifunctional materials capable of effectively removing OTC in both slurry and immobilized configurations. These findings provide a strong platform for advancing sustainable photocatalytic membrane systems tailored for real-world water purification challenges.

5.2 Recommendation

Future work on this study should focus on further optimization of the POME-induced, microwave-assisted synthesis parameters, including Ag precursor concentration, microwave power, irradiation time, and POME extract composition, to fine-tune particle size, morphology, and silver speciation. Given the strong influence of silver phase composition on photocatalytic activity, controlled synthesis strategies such as sequential reduction–oxidation steps or selective post-synthesis thermal treatments could be explored to tailor the dominant Ag species for targeted applications. The incorporation process into PAN membranes could also be refined by optimizing nanocomposite loading levels, dispersion methods, and casting parameters to achieve an improved balance between permeability and rejection.

While the current study has demonstrated excellent OTC degradation performance under controlled laboratory conditions, future work should extend this investigation to real-world water matrices, such as greywater, municipal wastewater, and industrial effluents, to assess robustness against complex contaminant mixtures. Pilot-scale demonstrations using both slurry and immobilized membrane configurations should be conducted outdoors under sunlight to evaluate performance under variable environmental conditions, along with assessments of silver leaching and potential ecotoxicity. Mechanistic studies, including charge-carrier dynamics and pathways for reactive oxygen species generation, should be conducted using advanced spectroscopic techniques to better understand the photocatalytic processes at play. Furthermore, extended operational trials should examine how membrane surface morphology, hydrophilicity, and fouling resistance evolve over time. Comparative analyses between powdered and immobilized systems should also be expanded to incorporate catalyst recovery efficiency, operational costs, and energy requirements. Finally, techno-economic and life-cycle assessments are recommended to evaluate the scalability, cost-effectiveness, and sustainability of deploying these materials in full-scale water treatment systems.

REFERENCES

Abey, S. A., Reis, N. M., Emanuelsson, E. A. C., & Expósito, A. J. (2025). Harnessing visible light: Advanced photocatalytic strategies for sustainable environmental reactions. *Chemical Engineering Journal*, *519*, 164951. https://doi.org/https://doi.org/10.1016/j.cej.2025.164951

Acharya, R., & Parida, K. (2020). A review on TiO2/g-C3N4 visible-light- responsive photocatalysts for sustainable energy generation and environmental remediation. *Journal of Environmental Chemical Engineering*, *8*(4), 103896. https://doi.org/https://doi.org/10.1016/j.jece.2020.103896

Ahmad, M. M., Mushtaq, S., Al Qahtani, H. S., Sedky, A., & Alam, M. W. (2021). Investigation of TiO2 Nanoparticles Synthesized by Sol-Gel Method for Effectual Photodegradation, Oxidation and Reduction Reaction. *Crystals*, *11*(12), 1456. https://www.mdpi.com/2073-4352/11/12/1456

Ahmadi, M., Alavi, S. M., & Larimi, A. (2023). Pt–Cu@Bi2MoO6/TiO2 Photocatalyst for CO2 Reduction. *Inorganic Chemistry*, *62*(49), 20372-20389. https://doi.org/10.1021/acs.inorgchem.3c03372

Ahmed, M. A., Mahmoud, S. A., & Mohamed, A. A. (2025). Interfacially engineered metal oxide nanocomposites for enhanced photocatalytic degradation of pollutants and energy applications [10.1039/D4RA08780A]. *RSC Advances*, *15*(20), 15561-15603. https://doi.org/10.1039/D4RA08780A

Ahmed, S. N., & Haider, W. (2018). Heterogeneous photocatalysis and its potential applications in water and wastewater treatment: a review. *Nanotechnology*, *29*(34), 342001. https://doi.org/10.1088/1361-6528/aac6ea

Al-hamoud, K., Shaik, M. R., Khan, M., Alkhathlan, H. Z., Adil, S. F., Kuniyil, M., Assal, M. E., Al-Warthan, A., Siddiqui, M. R. H., Tahir, M. N., Khan, S. T., Mousa, A. A., & Khan, M. (2022). Pulicaria undulata Extract-Mediated Eco-Friendly Preparation of TiO2 Nanoparticles for Photocatalytic Degradation of Methylene Blue and Methyl Orange. *ACS Omega*, *7*(6), 4812-4820. https://doi.org/10.1021/acsomega.1c05090

Albornoz Marin, S. L., de Oliveira, S. C., & Peralta-Zamora, P. (2022). Photocatalytic degradation of phenol by core–shell Cu@TiO2 nanostructures under visible radiation. *Journal of Photochemistry and Photobiology A: Chemistry*, *433*, 114129. https://doi.org/https://doi.org/10.1016/j.jphotochem.2022.114129

Aliero, A. S., Zawawi, N. A., Malek, N. A. N. N., Helmi Sani, M., & Usman, M. H. (2025). Biogenic Synthesis of Silver Nanoparticles Using Palm Oil Mill Effluent and its Antioxidant Potential. *Waste and Biomass Valorization*, *16*(7), 3535-3542. https://doi.org/10.1007/s12649-024-02872-y

Aliero, A. S., Zawawi, N. A., Malek, N. A. N. N., Usman, B. J., Asraf, M. H., Matmin, J., & Isah, M. (2024). Harnessing Palm Oil Mill Effluent for the Green Synthesis of Silver Nanoparticles: Optimization via Response Surface Methodology and Assessment of Antibacterial Activity. *Journal of Inorganic and Organometallic Polymers and Materials*. https://doi.org/10.1007/s10904-024-03478-6

Alkorbi, A. S., Muhammad Asif Javed, H., Hussain, S., Latif, S., Mahr, M. S., Mustafa, M. S., Alsaiari, R., & Alhemiary, N. A. (2022). Solar light-driven photocatalytic degradation of methyl blue by carbon-doped TiO2 nanoparticles. *Optical Materials*, *127*, 112259. https://doi.org/https://doi.org/10.1016/j.optmat.2022.112259

Ancy, K., Bindhu, M. R., Bai, J. S., Gatasheh, M. K., Hatamleh, A. A., & Ilavenil, S. (2022). Photocatalytic degradation of organic synthetic dyes and textile dyeing waste water

by Al and F co-doped TiO2 nanoparticles. *Environmental Research*, *206*, 112492. https://doi.org/https://doi.org/10.1016/j.envres.2021.112492

Anees Ahmad, S., Sachi Das, S., Khatoon, A., Tahir Ansari, M., Afzal, M., Saquib Hasnain, M., & Kumar Nayak, A. (2020). Bactericidal activity of silver nanoparticles: A mechanistic review. *Materials Science for Energy Technologies*, *3*, 756-769. https://doi.org/https://doi.org/10.1016/j.mset.2020.09.002

Anvari, A., Amoli-Diva, M., & Sadighi-Bonabi, R. (2021). Concurrent photocatalytic degradation and filtration with bi-plasmonic TiO2 for wastewater treatment. *Micro & Nano Letters*, *16*(3), 194-202. https://doi.org/https://doi.org/10.1049/mna2.12016

Aravind, M., Amalanathan, M., & Mary, M. S. M. (2021). Synthesis of TiO2 nanoparticles by chemical and green synthesis methods and their multifaceted properties. *SN Applied Sciences*, *3*(4), 409. https://doi.org/10.1007/s42452-021-04281-5

Arif, M., Zhang, M., Qiu, B., Yao, J., Bu, Q., Ali, A., Muhmood, T., Hussian, I., Liu, X., Zhou, B., & Wang, X. (2021). Synergistic effect of ultrathin thickness and surface oxygen vacancies in high-efficiency Ti-mediated Bi2MoO6 for immense photocatalytic nitrofurantoin degradation and Cr(VI) reduction. *Applied Surface Science*, *543*, 148816. https://doi.org/https://doi.org/10.1016/j.apsusc.2020.148816

Arifin, M. N., Jusoh, R., Abdullah, H., Ainirazali, N., & Setiabudi, H. D. (2023). Recent advances in advanced oxidation processes (AOPs) for the treatment of nitro- and alkyl-phenolic compounds. *Environmental Research*, *229*, 115936. https://doi.org/https://doi.org/10.1016/j.envres.2023.115936

Armaković, S. J., Savanović, M. M., & Armaković, S. (2023). Titanium Dioxide as the Most Used Photocatalyst for Water Purification: An Overview. *Catalysts*, *13*(1), 26. https://www.mdpi.com/2073-4344/13/1/26

Arumugam, A., Lee, K. E., Ng, P. Y., Shamsuddin, A. S., Zulkifli, A., & Goh, T. L. (2025). Pharmaceuticals as emerging pollutants: Implications for water resource management in Malaysia. *Emerging Contaminants*, *11*(2), 100470. https://doi.org/https://doi.org/10.1016/j.emcon.2025.100470

Arundhathi, B., Pabba, M., Raj, S. S., Sahu, N., & Sridhar, S. (2024). Advancements in Mixed-Matrix Membranes for Various Separation Applications: State of the Art and Future Prospects. *Membranes (Basel)*, *14*(11). https://doi.org/10.3390/membranes14110224

Athanasekou, C. P., Romanos, G. E., Katsaros, F. K., Kordatos, K., Likodimos, V., & Falaras, P. (2012). Very efficient composite titania membranes in hybrid ultrafiltration/photocatalysis water treatment processes. *Journal of Membrane Science*, *392-393*, 192-203. https://doi.org/https://doi.org/10.1016/j.memsci.2011.12.028

Bahadur, J., Agrawal, S., Panwar, V., Parveen, A., & Pal, K. (2016). Antibacterial properties of silver doped TiO2 nanoparticles synthesized via sol-gel technique. *Macromolecular Research*, *24*(6), 488-493. https://doi.org/10.1007/s13233-016-4066-9

Balu, S., Velmurugan, S., Palanisamy, S., Chen, S.-W., Velusamy, V., Yang, T. C. K., & El-Shafey, E.-S. I. (2019). Synthesis of α-Fe2O3 decorated g-C3N4/ZnO ternary Z-scheme photocatalyst for degradation of tartrazine dye in aqueous media. *Journal of the Taiwan Institute of Chemical Engineers*, *99*, 258-267. https://doi.org/https://doi.org/10.1016/j.jtice.2019.03.011

Bano, K., Mittal, S. K., Singh, P. P., & Kaushal, S. (2021). Sunlight driven photocatalytic degradation of organic pollutants using a MnV2O6/BiVO4 heterojunction: mechanistic perception and degradation pathways [10.1039/D1NA00499A]. *Nanoscale Advances*, *3*(22), 6446-6458. https://doi.org/10.1039/D1NA00499A

Bawazeer, S., Rauf, A., Shah, S. U. A., Shawky, A. M., Al-Awthan, Y. S., Bahattab, O. S., Uddin, G., Sabir, J., & El-Esawi, M. A. (2021). Green synthesis of silver nanoparticles using Tropaeolum majus: Phytochemical screening and antibacterial studies. *Green Processing and Synthesis*, *10*(1), 85-94. https://doi.org/doi:10.1515/gps-2021-0003

Bekele, T., & Alamnie, G. (2025). The photocatalytic degradation of organic pollutants-a comprehensive overview. *Results in Chemistry*, *18*, 102758. https://doi.org/https://doi.org/10.1016/j.rechem.2025.102758

Belousov, A. S., Parkhacheva, A. A., Markov, A. N., Petukhov, A. N., Kapinos, A. A., Atlaskin, A. A., Suvorov, S. S., & Vorotyntsev, A. V. (2024). Environmental application of versatile Bi-based perovskite photocatalysts and their Z-scheme and S-scheme heterojunctions. *Journal of Environmental Chemical Engineering*, *12*(5), 113309. https://doi.org/https://doi.org/10.1016/j.jece.2024.113309

Bhardwaj, D., & Singh, R. (2021). Green biomimetic synthesis of Ag–TiO2 nanocomposite using Origanum majorana leaf extract under sonication and their biological activities. *Bioresources and Bioprocessing*, *8*(1), 1. https://doi.org/10.1186/s40643-020-00357-z

Cai, L., Zhou, Y., Wang, Z., Chen, J., Ji, L., Guo, J., Wang, Y., Song, W., & Liu, J. (2019). Preparation and evaluation of a hierarchical Bi 2 MoO 6 /MSB composite for visible-light-driven photocatalytic performance. *RSC Advances*, *9*, 38280-38288. https://doi.org/10.1039/C9RA06559H

Celebi, N., Aydin, M. Y., Soysal, F., Ciftci, Y. O., & Salimi, K. (2021). Ligand-free fabrication of Au/TiO2 nanostructures for plasmonic hot-electron-driven photocatalysis: Photoelectrochemical water splitting and organic-dye degredation. *Journal of Alloys and Compounds*, *860*, 157908. https://doi.org/https://doi.org/10.1016/j.jallcom.2020.157908

Çeşmeli, S., & Biray Avci, C. (2019). Application of titanium dioxide (TiO2) nanoparticles in cancer therapies. *Journal of Drug Targeting*, *27*(7), 762-766. https://doi.org/10.1080/1061186X.2018.1527338

Chakhtouna, H., Benzeid, H., Zari, N., Qaiss, A. e. k., & Bouhfid, R. (2021). Recent progress on Ag/TiO2 photocatalysts: photocatalytic and bactericidal behaviors. *Environmental Science and Pollution Research*, *28*(33), 44638-44666. https://doi.org/10.1007/s11356-021-14996-y

Chakravorty, A., & Roy, S. (2024). A review of photocatalysis, basic principles, processes, and materials. *Sustainable Chemistry for the Environment*, *8*, 100155. https://doi.org/https://doi.org/10.1016/j.scenv.2024.100155

Chand, K., Abro, M. I., Aftab, U., Shah, A. H., Lakhan, M. N., Cao, D., Mehdi, G., & Ali Mohamed, A. M. (2019). Green synthesis characterization and antimicrobial activity against Staphylococcus aureus of silver nanoparticles using extracts of neem, onion and tomato [10.1039/C9RA01407A]. *RSC Advances*, *9*(30), 17002-17015. https://doi.org/10.1039/C9RA01407A

Chen, D., Cheng, Y., Zhou, N., Chen, P., Wang, Y., Li, K., Huo, S., Cheng, P., Peng, P., Zhang, R., Wang, L., Liu, H., Liu, Y., & Ruan, R. (2020). Photocatalytic degradation of organic pollutants using TiO2-based photocatalysts: A review. *Journal of Cleaner Production*, *268*, 121725. https://doi.org/https://doi.org/10.1016/j.jclepro.2020.121725

Chen, K., Dong, W., Huang, Y., Wang, F., Zhou, J. L., & Li, W. (2025). Photocatalysis for sustainable energy and environmental protection in construction: A review on surface engineering and emerging synthesis. *Journal of Environmental Chemical*

Engineering, *13*(5), 117529. https://doi.org/https://doi.org/10.1016/j.jece.2025.117529

Chen, K., Feng, X., Hu, R., Li, Y., Xie, K., Li, Y., & Gu, H. (2013). Effect of Ag nanoparticle size on the photoelectrochemical properties of Ag decorated TiO2 nanotube arrays. *Journal of Alloys and Compounds*, *554*, 72-79. https://doi.org/https://doi.org/10.1016/j.jallcom.2012.11.126

Chen, X., & Mao, S. S. (2007). Titanium Dioxide Nanomaterials: Synthesis, Properties, Modifications, and Applications. *Chemical Reviews*, *107*(7), 2891-2959. https://doi.org/10.1021/cr0500535

Collu, D. A., Carucci, C., Piludu, M., Parsons, D. F., & Salis, A. (2022). Aurivillius Oxides Nanosheets-Based Photocatalysts for Efficient Oxidation of Malachite Green Dye. *International Journal of Molecular Sciences*, *23*(10), 5422. https://www.mdpi.com/1422-0067/23/10/5422

Daels, N., Radoicic, M., Radetic, M., Van Hulle, S. W. H., & De Clerck, K. (2014). Functionalisation of electrospun polymer nanofibre membranes with TiO2 nanoparticles in view of dissolved organic matter photodegradation. *Separation and Purification Technology*, *133*, 282-290. https://doi.org/https://doi.org/10.1016/j.seppur.2014.06.040

Dahl, M., Liu, Y., & Yin, Y. (2014). Composite Titanium Dioxide Nanomaterials. *Chemical Reviews*, *114*(19), 9853-9889. https://doi.org/10.1021/cr400634p

Damodar, R. A., You, S.-J., & Chou, H.-H. (2009). Study the self cleaning, antibacterial and photocatalytic properties of TiO2 entrapped PVDF membranes. *Journal of Hazardous Materials*, *172*(2), 1321-1328. https://doi.org/https://doi.org/10.1016/j.jhazmat.2009.07.139

Das, R., Kumar, P., Singh, A. K., Agrawal, S., Albukhaty, S., Bhattacharya, I., Tiwari, K. N., Mishra, S. K., Tripathi, A. K., AlMalki, F. A., Alzubaidi, A. K., Al-Kaabi, W. J., Rajput, V. D., & Al-aqbi, Z. T. (2025). Green synthesis of silver nanoparticles using Trema Orientalis (L.) extract and evaluation of their antibacterial activity. *Green Chemistry Letters and Reviews*, *18*(1), 2444679. https://doi.org/10.1080/17518253.2024.2444679

Della Rocca, D. G., Peralta, R. M., Peralta, R. A., & Peralta Muniz Moreira, R. d. F. (2021). Recent development on Ag2MoO4-based advanced oxidation processes: a review. *Reaction Kinetics, Mechanisms and Catalysis*, *132*(1), 1-35. https://doi.org/10.1007/s11144-021-01934-9

Demir, M. E., Chehade, G., Dincer, I., Yuzer, B., & Selcuk, H. (2019). Synergistic effects of advanced oxidization reactions in a combination of TiO2 photocatalysis for hydrogen production and wastewater treatment applications. *International Journal of Hydrogen Energy*, *44*(43), 23856-23867. https://doi.org/https://doi.org/10.1016/j.ijhydene.2019.07.110

Devatha, C. P., & Thalla, A. K. (2018). Chapter 7 - Green Synthesis of Nanomaterials. In S. Mohan Bhagyaraj, O. S. Oluwafemi, N. Kalarikkal, & S. Thomas (Eds.), *Synthesis of Inorganic Nanomaterials* (pp. 169-184). Woodhead Publishing. https://doi.org/https://doi.org/10.1016/B978-0-08-101975-7.00007-5

Dhanalekshmi, D., Meena, K. s., & Ramesh, I. (2013). Synthesis and charatcerization of Ag@TiO_2 core-shell nanoparticle and study of its antibacterial property. *International Journal of Nanotechnology and Application*.

Dharma, H. N. C., Jaafar, J., Widiastuti, N., Matsuyama, H., Rajabsadeh, S., Othman, M. H. D., Rahman, M. A., Jafri, N. N. M., Suhaimin, N. S., Nasir, A. M., & Alias, N. H. (2022). A Review of Titanium Dioxide (TiO2)-Based Photocatalyst for Oilfield-

Produced Water Treatment. *Membranes*, *12*(3), 345. https://www.mdpi.com/2077-0375/12/3/345

Ding, Q., Zhang, L., & Yang, L. (2014). A simple approach for the synthesis of Ag-coated Ni@TiO2 nanocomposites as recyclable photocatalysts and SERS substrate to monitor catalytic degradation of dye molecules. *Materials Research Bulletin*, *53*, 205-210. https://doi.org/https://doi.org/10.1016/j.materresbull.2014.01.031

Djafer, L., Ayral, A., & Ouagued, A. (2010). Robust synthesis and performance of a titania-based ultrafiltration membrane with photocatalytic properties. *Separation and Purification Technology*, *75*(2), 198-203. https://doi.org/https://doi.org/10.1016/j.seppur.2010.08.001

Duong, T. T. H., Ding, S., Sebek, M., Lund, H., Bartling, S., Peppel, T., Le, T. S., & Steinfeldt, N. (2024). Effect of Bi2MoO6 Morphology on Adsorption and Visible-Light-Driven Degradation of 2,4-Dichlorophenoxyacetic Acid. *Molecules*, *29*(14), 3255. https://www.mdpi.com/1420-3049/29/14/3255

Eddy, D. R., Permana, M. D., Sakti, L. K., Sheha, G. A. N., Solihudin, Hidayat, S., Takei, T., Kumada, N., & Rahayu, I. (2023). Heterophase Polymorph of TiO(2) (Anatase, Rutile, Brookite, TiO(2) (B)) for Efficient Photocatalyst: Fabrication and Activity. *Nanomaterials (Basel)*, *13*(4). https://doi.org/10.3390/nano13040704

Elrasheedy, A., Nady, N., Bassyouni, M., & El-Shazly, A. (2019). Metal Organic Framework Based Polymer Mixed Matrix Membranes: Review on Applications in Water Purification. *Membranes*, *9*(7), 88. https://www.mdpi.com/2077-0375/9/7/88

Fatima, Q., Haidry, A. A., Zhang, H., El Jery, A., & Aldrdery, M. (2024). A critical review on advancement and challenges in using TiO2 as electron transport layer for perovskite solar cell. *Materials Today Sustainability*, *27*, 100857. https://doi.org/https://doi.org/10.1016/j.mtsust.2024.100857

Feng, T., & Yam, F. K. (2024a). A comparative study of TiO2 nanostructures prepared by one-step and two-step hydrothermal method: Physical and photoelectrochemical properties. *Physica B: Condensed Matter*, *684*, 415996. https://doi.org/https://doi.org/10.1016/j.physb.2024.415996

Feng, T., & Yam, F. K. (2024b). Photoelectrochemical properties of anatase TiO2 nanostructures prepared by hydrothermal method: Effect of illumination and external bias on charge transport. *Ceramics International*, *50*(11, Part B), 19886-19897. https://doi.org/https://doi.org/10.1016/j.ceramint.2024.03.116

Fischer, K., Grimm, M., Meyers, J., Dietrich, C., Gläser, R., & Schulze, A. (2015). Photoactive microfiltration membranes via directed synthesis of TiO2 nanoparticles on the polymer surface for removal of drugs from water. *Journal of Membrane Science*, *478*, 49-57. https://doi.org/https://doi.org/10.1016/j.memsci.2015.01.009

Frank, S. N., & Bard, A. J. (1977). Heterogeneous photocatalytic oxidation of cyanide ion in aqueous solutions at titanium dioxide powder. *Journal of the American Chemical Society*, *99*(1), 303-304. https://doi.org/10.1021/ja00443a081

Fujishima, A., & Honda, K. (1972). Electrochemical Photolysis of Water at a Semiconductor Electrode. *Nature*, *238*(5358), 37-38. https://doi.org/10.1038/238037a0

Gahlot, S., Dappozze, F., Mishra, S., & Guillard, C. (2021). High surface area g-C3N4 and g-C3N4-TiO2 photocatalytic activity under UV and Visible light: Impact of individual component. *Journal of Environmental Chemical Engineering*, *9*(4), 105587. https://doi.org/https://doi.org/10.1016/j.jece.2021.105587

Gan, P. P., Ng, S. H., Huang, Y., & Li, S. F. Y. (2012). Green synthesis of gold nanoparticles using palm oil mill effluent (POME): A low-cost and eco-friendly viable approach. *Bioresource Technology*, *113*, 132-135. https://doi.org/https://doi.org/10.1016/j.biortech.2012.01.015

Gomes, J. F., Lopes, A., Bednarczyk, K., Gmurek, M., Stelmachowski, M., Zaleska-Medynska, A., Quinta-Ferreira, M. E., Costa, R., Quinta-Ferreira, R. M., & Martins, R. C. (2018). Effect of Noble Metals (Ag, Pd, Pt) Loading over the Efficiency of TiO2 during Photocatalytic Ozonation on the Toxicity of Parabens. *ChemEngineering*, *2*(1), 4. https://www.mdpi.com/2305-7084/2/1/4

Guerra, F. D., Attia, M. F., Whitehead, D. C., & Alexis, F. (2018). Nanotechnology for Environmental Remediation: Materials and Applications. *Molecules*, *23*(7), 1760. https://www.mdpi.com/1420-3049/23/7/1760

Gui, X., Zhou, Y., Liang, Q., Zhou, M., Li, X., Xu, S., & Li, Z. (2023). Construction of porous ZnS/TiO2 S-scheme heterostructure derived from MOF-on-MOF with boosting photocatalytic H2-generation activity. *International Journal of Hydrogen Energy*, *48*(97), 38237-38250. https://doi.org/https://doi.org/10.1016/j.ijhydene.2023.06.129

Guo, F., Zhao, M., Xu, K., Huan, Y., Ge, S., Chen, Y., Huang, J., Cui, Y., Zhuang, J., Du, Y., Feng, H., & Hao, W. (2019). Evidence for the dynamic relaxation behavior of oxygen vacancies in Aurivillius Bi2MoO6 from dielectric spectroscopy during resistance switching [10.1039/C9TC02693B]. *Journal of Materials Chemistry C*, *7*(29), 8915-8922. https://doi.org/10.1039/C9TC02693B

Haggerty, J. E. S., Schelhas, L. T., Kitchaev, D. A., Mangum, J. S., Garten, L. M., Sun, W., Stone, K. H., Perkins, J. D., Toney, M. F., Ceder, G., Ginley, D. S., Gorman, B. P., & Tate, J. (2017). High-fraction brookite films from amorphous precursors. *Scientific Reports*, *7*(1), 15232. https://doi.org/10.1038/s41598-017-15364-y

Hartati, S., Zulfi, A., Maulida, P. Y. D., Yudhowijoyo, A., Dioktyanto, M., Saputro, K. E., Noviyanto, A., & Rochman, N. T. (2022). Synthesis of Electrospun PAN/TiO2/Ag Nanofibers Membrane As Potential Air Filtration Media with Photocatalytic Activity. *ACS Omega*, *7*(12), 10516-10525. https://doi.org/10.1021/acsomega.2c00015

Hena, S., Gutierrez, L., & Croué, J.-P. (2021). Removal of pharmaceutical and personal care products (PPCPs) from wastewater using microalgae: A review. *Journal of Hazardous Materials*, *403*, 124041. https://doi.org/https://doi.org/10.1016/j.jhazmat.2020.124041

Hitam, C. N. C., & Jalil, A. A. (2020). A review on exploration of Fe2O3 photocatalyst towards degradation of dyes and organic contaminants. *Journal of Environmental Management*, *258*, 110050. https://doi.org/https://doi.org/10.1016/j.jenvman.2019.110050

Huang, D., Li, Z., Zeng, G., Zhou, C., Xue, W., Gong, X., Yan, X., Chen, S., Wang, W., & Cheng, M. (2019). Megamerger in photocatalytic field: 2D g-C3N4 nanosheets serve as support of 0D nanomaterials for improving photocatalytic performance. *Applied Catalysis B: Environmental*, *240*, 153-173. https://doi.org/https://doi.org/10.1016/j.apcatb.2018.08.071

Huang, H., Xu, Y., Lu, Z., Zhang, A., Zhang, D., Xue, H., Dong, P., Zhang, J., & Goto, T. (2022). Highly permeable and dye-rejective nanofiltration membranes of TiO2 and Bi2S3 double-embedded Ti3C2Tx with a visible-light-induced self-cleaning ability. *Journal of Materials Research and Technology*, *18*, 4156-4168. https://doi.org/https://doi.org/10.1016/j.jmrt.2022.04.104

Hussain, A., Bilal, A., Azam, S., Akash, M. S. H., Imran, M., Ali, E., Kotwica-Mojzych, K., Glowacka, M., Mojzych, M., Ali, M., Ayub, M. A., Mammadova, K., Jan, A., & Khan, A. (2025). Green synthesis of iron and zinc nanoparticles, total phenolic and total flavonoid components, and pharmacological studies of Perovskia atriplicifolia Benth. *Scientific Reports*, *15*(1), 39448. https://doi.org/10.1038/s41598-025-23018-7

Imam, S. S., Sani, S., Mujahid, M., & Adnan, R. (2025). Valuable resources recovery from palm oil mill effluent (POME): A short review on sustainable wealth reclamation. *Waste Management Bulletin*, *3*(1), 1-16. https://doi.org/https://doi.org/10.1016/j.wmb.2024.12.002

Janczarek, M., Klapiszewski, Ł., Jędrzejczak, P., Klapiszewska, I., Ślosarczyk, A., & Jesionowski, T. (2022). Progress of functionalized TiO2-based nanomaterials in the construction industry: A comprehensive review. *Chemical Engineering Journal*, *430*, 132062. https://doi.org/https://doi.org/10.1016/j.cej.2021.132062

Jayapriya, M., & Arulmozhi, M. (2021). Beta vulgaris peel extract mediated synthesis of Ag/TiO2 nanocomposite: Characterization, evaluation of antibacterial and catalytic degradation of textile dyes-an electron relay effect. *Inorganic Chemistry Communications*, *128*, 108529. https://doi.org/https://doi.org/10.1016/j.inoche.2021.108529

Jiang, X., Wang, Z., Zhang, X., Jiang, G., Peng, Y., Xu, S., Cao, M., Dai, X., Liu, Z., & Ma, J. (2019). Enhanced photocatalytic activity of biosynthesized Au-Ag/TiO2 catalyst by removing excess anchored biomolecules. *Journal of Nanoparticle Research*, *21*(10), 211. https://doi.org/10.1007/s11051-019-4622-2

Jiang, Y., Sun, H., Guo, J., Liang, Y., Qin, P., Yang, Y., Luo, L., Leng, L., Gong, X., & Wu, Z. (2024). Vacancy Engineering in 2D Transition Metal Chalcogenide Photocatalyst: Structure Modulation, Function and Synergy Application. *Small*, *20*(34), 2310396. https://doi.org/https://doi.org/10.1002/smll.202310396

Jiménez Reinosa, J., Leret, P., Álvarez-Docio, C. M., del Campo, A., & Fernández, J. F. (2016). Enhancement of UV absorption behavior in ZnO–TiO2 composites. *Boletín de la Sociedad Española de Cerámica y Vidrio*, *55*(2), 55-62. https://doi.org/https://doi.org/10.1016/j.bsecv.2016.01.004

Kanakaraju, D., anak Kutiang, F. D., Lim, Y. C., & Goh, P. S. (2022). Recent progress of Ag/TiO2 photocatalyst for wastewater treatment: Doping, co-doping, and green materials functionalization. *Applied Materials Today*, *27*, 101500. https://doi.org/https://doi.org/10.1016/j.apmt.2022.101500

Kanakaraju, D., Chandrasekaran, A., & Lim, Y. C. (2024). Facile synthesis and characterization of a visible light-active ternary TiO2/ZnS/g-C3N4 heterostructure for multipollutant degradation. *Journal of Materials Science*, *59*(3), 810-827. https://doi.org/10.1007/s10853-023-09282-w

Kanakaraju, D., Glass, B. D., & Goh, P. S. (2025). Advanced oxidation process-mediated removal of pharmaceuticals from water: a review of recent advances. *Environmental Science and Pollution Research*, *32*(24), 14316-14350. https://doi.org/10.1007/s11356-025-36547-5

Kanwal, S., Khan, M. I., Uzair, M., Fatima, M., Bukhari, M. A., Saman, Z., Elsaeedy, H. I., Urram, S., Mufarreh Elqahtani, Z., & Alwadai, N. (2023). A facile green approach to the synthesis of Bi2WO6@V2O5 heterostructure and their photocatalytic activity evaluation under visible light irradiation for RhB dye removal. *Arabian Journal of Chemistry*, *16*(5), 104685. https://doi.org/https://doi.org/10.1016/j.arabjc.2023.104685

Katal, R., Masudy-Panah, S., Tanhaei, M., Farahani, M. H. D. A., & Jiangyong, H. (2020). A review on the synthesis of the various types of anatase TiO2 facets and their applications for photocatalysis. *Chemical Engineering Journal*, *384*, 123384. https://doi.org/https://doi.org/10.1016/j.cej.2019.123384

Khader, E. H., Muslim, S. A., Saady, N. M. C., Ali, N. S., Salih, I. K., Mohammed, T. J., Albayati, T. M., & Zendehboudi, S. (2024). Recent advances in photocatalytic advanced oxidation processes for organic compound degradation: A review.

Desalination and Water Treatment, *318*, 100384. https://doi.org/https://doi.org/10.1016/j.dwt.2024.100384

Khan, I., Saeed, K., & Khan, I. (2019). Nanoparticles: Properties, applications and toxicities. *Arabian Journal of Chemistry*, *12*(7), 908-931. https://doi.org/https://doi.org/10.1016/j.arabjc.2017.05.011

Khan, J. A., Sayed, M., Khan, S., Shah, N. S., Dionysiou, D. D., & Boczkaj, G. (2020). Chapter 9 - Advanced oxidation processes for the treatment of contaminants of emerging concern. In A. J. Hernández-Maldonado & L. Blaney (Eds.), *Contaminants of Emerging Concern in Water and Wastewater* (pp. 299-365). Butterworth-Heinemann. https://doi.org/https://doi.org/10.1016/B978-0-12-813561-7.00009-2

Kim, M. G., Kang, J. M., Lee, J. E., Kim, K. S., Kim, K. H., Cho, M., & Lee, S. G. (2021). Effects of Calcination Temperature on the Phase Composition, Photocatalytic Degradation, and Virucidal Activities of TiO2 Nanoparticles. *ACS Omega*, *6*(16), 10668-10678. https://doi.org/10.1021/acsomega.1c00043

Kirubakaran, D., Wahid, J. B. A., Karmegam, N., Jeevika, R., Sellapillai, L., Rajkumar, M., & SenthilKumar, K. J. (2026). A Comprehensive Review on the Green Synthesis of Nanoparticles: Advancements in Biomedical and Environmental Applications. *Biomedical Materials & Devices*, *4*(1), 388-413. https://doi.org/10.1007/s44174-025-00295-4

Kocijan, M., Vukšić, M., Kurtjak, M., Ćurković, L., Vengust, D., & Podlogar, M. (2022). TiO2-Based Heterostructure Containing g-C3N4 for an Effective Photocatalytic Treatment of a Textile Dye. *Catalysts*, *12*(12), 1554. https://www.mdpi.com/2073-4344/12/12/1554

Kong, J., Yang, T., Rui, Z., & Ji, H. (2019). Perovskite-based photocatalysts for organic contaminants removal: Current status and future perspectives. *Catalysis Today*, *327*, 47-63. https://doi.org/https://doi.org/10.1016/j.cattod.2018.06.045

Kubacka, A., Fernández-García, M., & Colón, G. (2012). Advanced Nanoarchitectures for Solar Photocatalytic Applications. *Chemical Reviews*, *112*(3), 1555-1614. https://doi.org/10.1021/cr100454n

Kumar, A., Kumar, A., & Krishnan, V. (2020). Perovskite Oxide Based Materials for Energy and Environment-Oriented Photocatalysis. *ACS Catalysis*, *10*(17), 10253-10315. https://doi.org/10.1021/acscatal.0c02947

Kumar, B., Smita, K., Angulo, Y., & Cumbal, L. (2016). Valorization of rambutan peel for the synthesis of silver-doped titanium dioxide (Ag/TiO2) nanoparticles. *5*(4), 371-377. https://doi.org/doi:10.1515/gps-2016-0003 (Green Processing and Synthesis)

Kumar, S., Yadav, S., Kataria, N., Chauhan, A. K., Joshi, S., Gupta, R., Kumar, P., Chong, J. W. R., Khoo, K. S., & Show, P. L. (2023). Recent Advancement in Nanotechnology for the Treatment of Pharmaceutical Wastewater: Sources, Toxicity, and Remediation Technology. *Current Pollution Reports*, *9*(2), 110-142. https://doi.org/10.1007/s40726-023-00251-0

Kumaravel, V., Mathew, S., Bartlett, J., & Pillai, S. C. (2019). Photocatalytic hydrogen production using metal doped TiO2: A review of recent advances. *Applied Catalysis B: Environmental*, *244*, 1021-1064. https://doi.org/https://doi.org/10.1016/j.apcatb.2018.11.080

Kumari, P., & Kumar, A. (2023). ADVANCED OXIDATION PROCESS: A remediation technique for organic and non-biodegradable pollutant. *Results in Surfaces and Interfaces*, *11*, 100122. https://doi.org/https://doi.org/10.1016/j.rsurfi.2023.100122

Kusdianto, K., Jiang, D., Kubo, M., & Shimada, M. (2018). Effect of annealing temperature on the photocatalytic activity of Ag–TiO2 nanocomposite films by one-step gas-

phase deposition. *Materials Research Bulletin*, *97*, 497-505. https://doi.org/https://doi.org/10.1016/j.materresbull.2017.08.062

Kweinor Tetteh, E., & Rathilal, S. (2021). Application of biomagnetic nanoparticles for biostimulation of biogas production from wastewater treatment. *Materials Today: Proceedings*, *45*, 5214-5220. https://doi.org/https://doi.org/10.1016/j.matpr.2021.01.720

Lang, J., Takahashi, K., Kubo, M., & Shimada, M. (2022). Preparation of TiO2-CNT-Ag Ternary Composite Film with Enhanced Photocatalytic Activity via Plasma-Enhanced Chemical Vapor Deposition. *Catalysts*, *12*(5), 508. https://www.mdpi.com/2073-4344/12/5/508

Leong, S., Razmjou, A., Wang, K., Hapgood, K., Zhang, X., & Wang, H. (2014). TiO2 based photocatalytic membranes: A review. *Journal of Membrane Science*, *472*, 167-184. https://doi.org/https://doi.org/10.1016/j.memsci.2014.08.016

Li, D., Song, H., Meng, X., Shen, T., Sun, J., Han, W., & Wang, X. (2020). Effects of Particle Size on the Structure and Photocatalytic Performance by Alkali-Treated TiO2. *Nanomaterials*, *10*(3), 546. https://www.mdpi.com/2079-4991/10/3/546

Li, R., Li, T., & Zhou, Q. (2020). Impact of Titanium Dioxide (TiO2) Modification on Its Application to Pollution Treatment—A Review. *Catalysts*, *10*(7), 804. https://www.mdpi.com/2073-4344/10/7/804

Lin, H., Huang, C. P., Li, W., Ni, C., Shah, S. I., & Tseng, Y.-H. (2006). Size dependency of nanocrystalline TiO2 on its optical property and photocatalytic reactivity exemplified by 2-chlorophenol. *Applied Catalysis B: Environmental*, *68*(1), 1-11. https://doi.org/https://doi.org/10.1016/j.apcatb.2006.07.018

Lin, X., Hou, J., Jiang, S., Lin, Z., Wang, M., & Che, G. (2015). A Z-scheme visible-light-driven Ag/Ag3PO4/Bi2MoO6 photocatalyst: synthesis and enhanced photocatalytic activity [10.1039/C5RA22110B]. *RSC Advances*, *5*(127), 104815-104821. https://doi.org/10.1039/C5RA22110B

Lin, Y.-F., Tung, K.-L., Tzeng, Y.-S., Chen, J.-H., & Chang, K.-S. (2012). Rapid atmospheric plasma spray coating preparation and photocatalytic activity of macroporous titania nanocrystalline membranes. *Journal of Membrane Science*, *389*, 83-90. https://doi.org/https://doi.org/10.1016/j.memsci.2011.10.018

Lin, Z., Xu, J., Gu, H., Huang, J., Lin, J., Shao, J., Wang, D., & Li, H. (2023). A review on research progress in photocatalytic degradation of organic pollutants by Bi2MoO6. *Journal of Environmental Chemical Engineering*, *11*(5), 110911. https://doi.org/https://doi.org/10.1016/j.jece.2023.110911

Liu, G., Zhang, S., Xu, L., Hu, Y., Li, X., Zhang, S., & Zeng, H. (2022). Recent advances of eco-friendly quantum dots light-emitting diodes for display. *Progress in Quantum Electronics*, *86*, 100415. https://doi.org/https://doi.org/10.1016/j.pquantelec.2022.100415

Liu, W., Iordan, C. M., Cherubini, F., Hu, X., & Fu, D. (2021). Environmental impacts assessment of wastewater treatment and sludge disposal systems under two sewage discharge standards: A case study in Kunshan, China. *Journal of Cleaner Production*, *287*, 125046. https://doi.org/https://doi.org/10.1016/j.jclepro.2020.125046

Liu, Y., Tian, J., Wei, L., Wang, Q., Wang, C., & Yang, C. (2020). A novel microwave-assisted impregnation method with water as the dispersion medium to synthesize modified g-C3N4/TiO2 heterojunction photocatalysts. *Optical Materials*, *107*, 110128. https://doi.org/https://doi.org/10.1016/j.optmat.2020.110128

Liu, Z., Tian, J., Zeng, D., Yu, C., Huang, W., Yang, K., Liu, X., & Liu, H. (2019). Binary-phase TiO2 modified Bi2MoO6 crystal for effective removal of antibiotics under

visible light illumination. *Materials Research Bulletin*, *112*, 336-345. https://doi.org/https://doi.org/10.1016/j.materresbull.2019.01.002

Lucas-Gómez, I., Carrasco-Torres, G., Bahena-Uribe, D., Santoyo-Salazar, J., Fernández-Martínez, E., Sánchez-Crisóstomo, I., Pescador-Rojas, J. A., & Aparicio-Burgos, J. E. (2020). Green synthesis of silver nanoparticles with phytosterols and betalain pigments as reducing agents present in cactus Myrtillocactus geometrizans. *MRS Advances*, *5*(63), 3361-3369. https://doi.org/10.1557/adv.2020.415

Luttrell, T., Halpegamage, S., Tao, J., Kramer, A., Sutter, E., & Batzill, M. (2014). Why is anatase a better photocatalyst than rutile? - Model studies on epitaxial TiO2 films. *Scientific Reports*, *4*(1), 4043. https://doi.org/10.1038/srep04043

Ma, X., Wang, H., Chen, Y., Fu, L., Zhou, J., Zhang, L., Xing, Z., Zhang, Q., & Xia, L. (2024). Application of Ag@g-C3N4/TiO2 cotton fabric flexible substrate with dual functionality: Photocatalytic reusability and SERS signal amplification for food safety detection. *Applied Surface Science*, *661*, 160068. https://doi.org/https://doi.org/10.1016/j.apsusc.2024.160068

Magaña-López, R., Zaragoza-Sánchez, P. I., Jiménez-Cisneros, B. E., & Chávez-Mejía, A. C. (2021). The Use of TiO2 as a Disinfectant in Water Sanitation Applications. *Water*, *13*(12), 1641. https://www.mdpi.com/2073-4441/13/12/1641

Malakootian, M., Nasiri, A., & Amiri Gharaghani, M. (2020). Photocatalytic degradation of ciprofloxacin antibiotic by TiO2 nanoparticles immobilized on a glass plate. *Chemical Engineering Communications*, *207*(1), 56-72. https://doi.org/10.1080/00986445.2019.1573168

Malik, J., Kumar, S., Srivastava, P., Bag, M., & Mandal, T. K. (2021). Cation disorder and octahedral distortion control of internal electric field, band bending and carrier lifetime in Aurivillius perovskite solid solutions for enhanced photocatalytic activity [10.1039/D1MA00304F]. *Materials Advances*, *2*(14), 4832-4842. https://doi.org/10.1039/D1MA00304F

Martin, D. J., Reardon, P. J. T., Moniz, S. J. A., & Tang, J. (2014). Visible Light-Driven Pure Water Splitting by a Nature-Inspired Organic Semiconductor-Based System. *Journal of the American Chemical Society*, *136*(36), 12568-12571. https://doi.org/10.1021/ja506386e

Matias, M. L., Reis-Machado, A. S., Rodrigues, J., Calmeiro, T., Deuermeier, J., Pimentel, A., Fortunato, E., Martins, R., & Nunes, D. (2023). Microwave Synthesis of Visible-Light-Activated g-C3N4/TiO2 Photocatalysts. *Nanomaterials*, *13*(6), 1090. https://www.mdpi.com/2079-4991/13/6/1090

Mohamed, K. M., Benitto, J. J., Vijaya, J. J., & Bououdina, M. (2023). Recent Advances in ZnO-Based Nanostructures for the Photocatalytic Degradation of Hazardous, Non-Biodegradable Medicines. *Crystals*, *13*(2), 329. https://www.mdpi.com/2073-4352/13/2/329

Mohan, P. S., Sonsuddin, F., Mainal, A. B., Yahya, R., Venkatraman, G., Vadivelu, J., Al-Farraj, D. A., Al-Mohaimeed, A. M., & Alarjani, K. M. (2021). Facile In-Situ Fabrication of a Ternary ZnO/TiO2/Ag Nanocomposite for Enhanced Bactericidal and Biocompatibility Properties. *Antibiotics*, *10*(1), 86. https://www.mdpi.com/2079-6382/10/1/86

Mohapatra, T., Manekar, S., Kumar Sahu, V., Soni, A. K., Banerjee, S., & Ghosh, P. (2021). Green synthesized Ag-TiO2 for degradation of organic dye through visible light driven photo-reactor and its kinetics. *19*(9), 893-900. https://doi.org/doi:10.1515/ijcre-2021-0111 (International Journal of Chemical Reactor Engineering)

Molinari, R., Pirillo, F., Falco, M., Loddo, V., & Palmisano, L. (2004). Photocatalytic degradation of dyes by using a membrane reactor. *Chemical Engineering and Processing: Process Intensification*, *43*(9), 1103-1114. https://doi.org/https://doi.org/10.1016/j.cep.2004.01.008

Monga, D., & Basu, S. (2019). Enhanced photocatalytic degradation of industrial dye by g-C3N4/TiO2 nanocomposite: Role of shape of TiO2. *Advanced Powder Technology*, *30*(5), 1089-1098. https://doi.org/https://doi.org/10.1016/j.apt.2019.03.004

Muhmood, T., Ahmad, I., Haider, Z., Haider, S. K., Shahzadi, N., Aftab, A., Ahmed, S., & Ahmad, F. (2024). Graphene-like graphitic carbon nitride (g-C3N4) as a semiconductor photocatalyst: Properties, classification, and defects engineering approaches. *Materials Today Sustainability*, *25*, 100633. https://doi.org/https://doi.org/10.1016/j.mtsust.2023.100633

Neikov, O. D., & Yefimov, N. A. (2019). Chapter 9 - Nanopowders. In O. D. Neikov, S. S. Naboychenko, & N. A. Yefimov (Eds.), *Handbook of Non-Ferrous Metal Powders (Second Edition)* (pp. 271-311). Elsevier. https://doi.org/https://doi.org/10.1016/B978-0-08-100543-9.00009-9

Nemiwal, M., Zhang, T. C., & Kumar, D. (2021). Recent progress in g-C3N4, TiO2 and ZnO based photocatalysts for dye degradation: Strategies to improve photocatalytic activity. *Science of The Total Environment*, *767*, 144896. https://doi.org/https://doi.org/10.1016/j.scitotenv.2020.144896

Nethravathi, P. C., Udayabhanu, Nagaraju, G., & Suresh, D. (2022). TiO2 and Ag-TiO2 nanomaterials for enhanced photocatalytic and antioxidant activity: Green synthesis using Cucumis melo juice. *Materials Today: Proceedings*, *49*, 841-848. https://doi.org/https://doi.org/10.1016/j.matpr.2021.05.670

Nguyen, T. H., Hoang, N. H., Van Tran, C., Nguyen, P. T. M., Dang, T.-D., Chung, W. J., Chang, S. W., Nguyen, D. D., Senthil Kumar, P., & La, D. D. (2022). Green synthesis of a photocatalyst Ag/TiO2 nanocomposite using Cleistocalyx operculatus leaf extract for degradation of organic dyes. *Chemosphere*, *306*, 135474. https://doi.org/https://doi.org/10.1016/j.chemosphere.2022.135474

Nunzi, F., & De Angelis, F. (2022). Modeling titanium dioxide nanostructures for photocatalysis and photovoltaics [10.1039/D2SC02872G]. *Chemical Science*, *13*(33), 9485-9497. https://doi.org/10.1039/D2SC02872G

Nuzul, M. I., Jong, V. Y. M., Koo, L. F., Chan, T. H., Ang, C. H., Idris, J., Husen, R., & Wong, S. W. (2022). Effects of Extraction Methods on Phenolic Content in the Young Bamboo Culm Extracts of Bambusa beecheyana Munro. *Molecules*, *27*(7), 2359. https://www.mdpi.com/1420-3049/27/7/2359

Ofori-Boateng, C., & Lee, K. T. (2013). Sustainable utilization of oil palm wastes for bioactive phytochemicals for the benefit of the oil palm and nutraceutical industries. *Phytochemistry Reviews*, *12*(1), 173-190. https://doi.org/10.1007/s11101-013-9270-z

Ong, W.-J., Tan, L.-L., Ng, Y. H., Yong, S.-T., & Chai, S.-P. (2016). Graphitic Carbon Nitride (g-C3N4)-Based Photocatalysts for Artificial Photosynthesis and Environmental Remediation: Are We a Step Closer To Achieving Sustainability? *Chemical Reviews*, *116*(12), 7159-7329. https://doi.org/10.1021/acs.chemrev.6b00075

Pascariu, P., Cojocaru, C., Samoila, P., Airinei, A., Olaru, N., Rotaru, A., Romanitan, C., Tudoran, L. B., & Suchea, M. (2022). Cu/TiO2 composite nanofibers with improved photocatalytic performance under UV and UV–visible light irradiation. *Surfaces and Interfaces*, *28*, 101644. https://doi.org/https://doi.org/10.1016/j.surfin.2021.101644

Paumo, H. K., Dalhatou, S., Katata-Seru, L. M., Kamdem, B. P., Tijani, J. O., Vishwanathan, V., Kane, A., & Bahadur, I. (2021). TiO2 assisted photocatalysts for degradation of

emerging organic pollutants in water and wastewater. *Journal of Molecular Liquids*, *331*, 115458. https://doi.org/https://doi.org/10.1016/j.molliq.2021.115458

Pradhan, S. P., Swain, S., Sa, N., Pilla, S. N., Behera, A., Sahu, P. K., & Chandra Si, S. (2022). Photocatalysis of environmental organic pollutants and antioxidant activity of flavonoid conjugated gold nanoparticles. *Spectrochimica Acta Part A: Molecular and Biomolecular Spectroscopy*, *282*, 121699. https://doi.org/https://doi.org/10.1016/j.saa.2022.121699

Qamar, O. A., Jamil, F., Hussain, M., Bae, S., Inayat, A., Shah, N. S., Waris, A., Akhter, P., Kwon, E. E., & Park, Y.-K. (2023). Advances in synthesis of TiO2 nanoparticles and their application to biodiesel production: A review. *Chemical Engineering Journal*, *460*, 141734. https://doi.org/https://doi.org/10.1016/j.cej.2023.141734

Qi, N., Yi, Y., Tang, Y., Liu, X., Yuan, Y., He, Z., Shi, X., Fang, Y., He, Y., & Wei, S. (2025). Constructing a novel Bi2MoO6/TiO2/Ti3C2 composite with efficient carrier separation for excellent photocatalytic purification of TC. *Journal of Alloys and Compounds*, *1010*, 177575. https://doi.org/https://doi.org/10.1016/j.jallcom.2024.177575

Quadri, T. W., Fayemi, O. E., Olasunkanmi, L. O., & Ebenso, E. E. (2023). Chapter 15 - Survey of different electrochemical and analytical techniques for corrosion measurements. In J. Aslam, C. Verma, & C. Mustansar Hussain (Eds.), *Electrochemical and Analytical Techniques for Sustainable Corrosion Monitoring* (pp. 293-323). Elsevier. https://doi.org/https://doi.org/10.1016/B978-0-443-15783-7.00012-8

Rachmaniar, S., Nugraha, D. A., Santjojo, D. J. D. H., Tjahjanto, R. T., Mufti, N., & Masruroh. (2024). Prevention of particle agglomeration in sol–gel synthesis of TiO2 nanoparticles via addition of surfactant. *Journal of Nanoparticle Research*, *26*(3), 45. https://doi.org/10.1007/s11051-024-05943-2

Raes, A., Minja, A. C., Ag, K. R., & Verbruggen, S. W. (2024). Recent advances in metal-doped defective TiO2 for photocatalytic CO2 conversion. *Current Opinion in Chemical Engineering*, *44*, 101013. https://doi.org/https://doi.org/10.1016/j.coche.2024.101013

Rahimpour, A., Jahanshahi, M., Rajaeian, B., & Rahimnejad, M. (2011). TiO2 entrapped nano-composite PVDF/SPES membranes: Preparation, characterization, antifouling and antibacterial properties. *Desalination*, *278*(1), 343-353. https://doi.org/https://doi.org/10.1016/j.desal.2011.05.049

Rahmawati, T., Butburee, T., Sangkhun, W., Wutikhun, T., Padchasri, J., Kidkhunthod, P., Phromma, S., Eksangsri, T., Kangwansupamonkon, W., Leeladee, P., & Sapcharoenkun, C. (2023). Green synthesis of Ag-TiO2 nanoparticles using turmeric extract and its enhanced photocatalytic activity under visible light. *Colloids and Surfaces A: Physicochemical and Engineering Aspects*, *665*, 131206. https://doi.org/https://doi.org/10.1016/j.colsurfa.2023.131206

Ramon, G. Z., & Hoek, E. M. V. (2013). Transport through composite membranes, part 2: Impacts of roughness on permeability and fouling. *Journal of Membrane Science*, *425-426*, 141-148. https://doi.org/https://doi.org/10.1016/j.memsci.2012.08.004

Rana, A., Yadav, K., & Jagadevan, S. (2020). A comprehensive review on green synthesis of nature-inspired metal nanoparticles: Mechanism, application and toxicity. *Journal of Cleaner Production*, *272*, 122880. https://doi.org/https://doi.org/10.1016/j.jclepro.2020.122880

Ranjithkumar, R., Lakshmanan, P., Palanisami, N., Devendran, P., Nallamuthu, N., Sudhahar, S., & Kumar, M. K. (2023). Facile, Morphology-Controlled and Mass Production of 0D-Ag/2D-g-C3N4/3D-TiO2 Nano-composite Materials: Effect of

Silver Morphology and Loading on the Electrochemical Performance. *Electronic Materials Letters*, *19*(2), 172-183. https://doi.org/10.1007/s13391-022-00385-1

Ravishankar, T. N., Banuprakash, G., & de O. Vaz, M. (2022). Synthesis of Ag@TiO2/NiFe2O4 ternary nanostructures and evaluation of their photocatalytic activities. *Journal of Materials Science: Materials in Electronics*, *33*(29), 23153-23173. https://doi.org/10.1007/s10854-022-09080-1

Riaz, S., & Park, S.-J. (2020). An overview of TiO2-based photocatalytic membrane reactors for water and wastewater treatments. *Journal of Industrial and Engineering Chemistry*, *84*, 23-41. https://doi.org/https://doi.org/10.1016/j.jiec.2019.12.021

Rizvi, H. I., Munir, R. M., Iqbal, T., Younas, A., Afsheen, S., Qureshi, M. T., Aamir, L., Elaimi, M. A., Sultana, K., Riaz, K. N., & Yousaf, M. (2024). Novel existence of Mn and Cu in WO3 nanostructures for promising photocatalytic activity against MB dye and Levofloxacin antibiotic. *Journal of Alloys and Compounds*, *993*, 174549. https://doi.org/https://doi.org/10.1016/j.jallcom.2024.174549

Sadek, O., Touhtouh, S., Rkhis, M., Anoua, R., El Jouad, M., Belhora, F., & Hajjaji, A. (2022). Synthesis by sol-gel method and characterization of nano-TiO2 powders. *Materials Today: Proceedings*, *66*, 456-458. https://doi.org/https://doi.org/10.1016/j.matpr.2022.06.385

Saeed, M., Muneer, M., Khosa, M. K. K., Akram, N., Khalid, S., Adeel, M., Nisar, A., & Sherazi, S. (2019). Azadirachta indica leaves extract assisted green synthesis of Ag-TiO2 for degradation of Methylene blue and Rhodamine B dyes in aqueous medium. *8*(1), 659-666. https://doi.org/doi:10.1515/gps-2019-0036 (Green Processing and Synthesis)

Sahu, A., Dosi, R., Kwiatkowski, C., Schmal, S., & Poler, J. C. (2023). Advanced Polymeric Nanocomposite Membranes for Water and Wastewater Treatment: A Comprehensive Review. *Polymers*, *15*(3), 540. https://www.mdpi.com/2073-4360/15/3/540

Samy, M., Tang, S., Zhang, Y., & Leung, D. Y. C. (2024). Understanding the variations in degradation pathways and generated by-products of antibiotics in modified TiO2 and ZnO photodegradation systems: A comprehensive review. *Journal of Environmental Management*, *370*, 122402. https://doi.org/https://doi.org/10.1016/j.jenvman.2024.122402

Santana, R. M. d. R., Napoleão, D. C., Rodriguez-Diaz, J. M., Gomes, R. K. d. M., Silva, M. G., Lima, V. M. E. d., Melo Neto, A. A. d., Vinhas, G. M., & Duarte, M. M. M. B. (2023). Efficient microbial cellulose/Fe3O4 nanocomposite for photocatalytic degradation by advanced oxidation process of textile dyes. *Chemosphere*, *326*, 138453. https://doi.org/https://doi.org/10.1016/j.chemosphere.2023.138453

Selvamani, M., Balachandran, S., Kesavan, A. V., & Vinoth, V. (2023). Bi2MoO6 nano-flowers for Bi-functional application: Anticancer activity against B16F10 (Mice melanoma) and photocatalytic dye degradation. *Surfaces and Interfaces*, *42*, 103340. https://doi.org/https://doi.org/10.1016/j.surfin.2023.103340

Sewnet, A., Alemayehu, E., Abebe, M., Mani, D., Thomas, S., & Lennartz, B. (2023). Hydrothermal Synthesis of Heterostructured g-C3N4/Ag–TiO2 Nanocomposites for Enhanced Photocatalytic Degradation of Organic Pollutants. *Materials*, *16*(15), 5497. https://www.mdpi.com/1996-1944/16/15/5497

Shankar, S., & Rhim, J.-W. (2016). Tocopherol-mediated synthesis of silver nanoparticles and preparation of antimicrobial PBAT/silver nanoparticles composite films. *LWT - Food Science and Technology*, *72*, 149-156. https://doi.org/https://doi.org/10.1016/j.lwt.2016.04.054

Shi, Y., Huang, J., Zeng, G., Cheng, W., & Hu, J. (2019). Photocatalytic membrane in water purification: is it stepping closer to be driven by visible light? *Journal of Membrane Science*, *584*, 364-392. https://doi.org/https://doi.org/10.1016/j.memsci.2019.04.078

Shoaib, A., Ji, M., Qian, H., Liu, J., Xu, M., & Zhang, J. (2016). Noble metal nanoclusters and their in situ calcination to nanocrystals: Precise control of their size and interface with TiO2 nanosheets and their versatile catalysis applications. *Nano Research*, *9*(6), 1763-1774. https://doi.org/10.1007/s12274-016-1069-y

Singh, J., Palsaniya, S., & Soni, R. K. (2020). Mesoporous dark brown TiO2 spheres for pollutant removal and energy storage applications. *Applied Surface Science*, *527*, 146796. https://doi.org/https://doi.org/10.1016/j.apsusc.2020.146796

Ślósarczyk, K., Jakóbczyk-Karpierz, S., Różkowski, J., & Witkowski, A. J. (2021). Occurrence of Pharmaceuticals and Personal Care Products in the Water Environment of Poland: A Review. *Water*, *13*(16), 2283. https://www.mdpi.com/2073-4441/13/16/2283

Sowani, H., Mohite, P., Damale, S., Kulkarni, M., & Zinjarde, S. (2016). Carotenoid stabilized gold and silver nanoparticles derived from the Actinomycete Gordonia amicalis HS-11 as effective free radical scavengers. *Enzyme and Microbial Technology*, *95*, 164-173. https://doi.org/https://doi.org/10.1016/j.enzmictec.2016.09.016

Starr, B. J., Tarabara, V. V., Herrera-Robledo, M., Zhou, M., Roualdès, S., & Ayral, A. (2016). Coating porous membranes with a photocatalyst: Comparison of LbL self-assembly and plasma-enhanced CVD techniques. *Journal of Membrane Science*, *514*, 340-349. https://doi.org/https://doi.org/10.1016/j.memsci.2016.04.050

Sui, G., Li, J., Du, L., Zhuang, Y., Zhang, Y., Zou, Y., & Li, B. (2020). Preparation and characterization of g-C3N4/Ag–TiO2 ternary hollowsphere nanoheterojunction catalyst with high visible light photocatalytic performance. *Journal of Alloys and Compounds*, *823*, 153851. https://doi.org/https://doi.org/10.1016/j.jallcom.2020.153851

Sutar, R. S., Barkul, R. P., Delekar, S. D., & Patil, M. K. (2020). Sunlight assisted photocatalytic degradation of organic pollutants using g-C3N4-TiO2 nanocomposites. *Arabian Journal of Chemistry*, *13*(4), 4966-4977. https://doi.org/https://doi.org/10.1016/j.arabjc.2020.01.019

Tan Sian Hui Abdullah, H. S., Aqlili Riana Mohd Asseri, S. N., Khursyiah Wan Mohamad, W. N., Kan, S.-Y., Azmi, A. A., Yong Julius, F. S., & Chia, P. W. (2021). Green synthesis, characterization and applications of silver nanoparticle mediated by the aqueous extract of red onion peel. *Environmental pollution (Barking, Essex : 1987)*, *271*, 116295. https://doi.org/10.1016/j.envpol.2020.116295

Tao, L., Chen, Z., Li, Z., Wang, J., Xu, X., & Xu, J.-B. (2021). Enhancing light-matter interaction in 2D materials by optical micro/nano architectures for high-performance optoelectronic devices. *InfoMat*, *3*(1), 36-60. https://doi.org/https://doi.org/10.1002/inf2.12148

Tavakoli, F., Badiei, A., & Ghasemi, J. B. (2019). Novel and ecofriendly synthesis of Ag-TiO2-G photocatalyst and investigate the effect of graphene in photodegradation of an organic pollutant in water. *Journal of Water and Environmental Nanotechnology*, *4*(1), 31-39. https://doi.org/10.22090/jwent.2019.01.003

Teh, S. S., Hock Ong, A. S., & Mah, S. H. (2017). Recovery and Utilization of Palm Oil Mill Effluent Source as Value-Added Food Products. *Journal of Oleo Science*, *66*(11), 1183-1191. https://doi.org/10.5650/jos.ess17078

Teixeira, I. F., Barbosa, E. C. M., Tsang, S. C. E., & Camargo, P. H. C. (2018). Carbon nitrides and metal nanoparticles: from controlled synthesis to design principles for

improved photocatalysis [10.1039/C8CS00479J]. *Chemical Society Reviews*, *47*(20), 7783-7817. https://doi.org/10.1039/C8CS00479J

Torres-Limiñana, J., Feregrino-Pérez, A. A., Vega-González, M., Escobar-Alarcón, L., Cervantes-Chávez, J. A., & Esquivel, K. (2022). Green Synthesis via Eucalyptus globulus L. Extract of Ag-TiO2 Catalyst: Antimicrobial Activity Evaluation toward Water Disinfection Process. *Nanomaterials*, *12*(11), 1944. https://www.mdpi.com/2079-4991/12/11/1944

Truong, H. T., Pham, T. T., & Pham, H. V. (2025). Enhanced Photocatalytic Activity of Ag-Doped WO3 for Antibiotic and Bacterial Removal in Fishponds. *Aquaculture Research*, *2025*(1), 6634836. https://doi.org/https://doi.org/10.1155/are/6634836

Utomo, R. S. B., Sentanuhady, J., & Muflikhun, M. A. (2024). TiO2–SiO2 nanocomposite via a novel sol-gel method with the addition of an energy monitoring device: Synthesized, characterization and anti-bacterial applications. *Ceramics International*, *50*(13, Part A), 23367-23378. https://doi.org/https://doi.org/10.1016/j.ceramint.2024.04.059

Vatanpour, V., Camadan, I., Kara, N., Naziri Mehrabani, S. A., Feizpoor, S., Habibi-Yangjeh, A., & Koyuncu, I. (2024). TiO2/AgBr nanocomposite as a novel hydrophilic and photocatalytic modifier in the fabrication of polyethersulfone membrane for wastewater treatment. *Separation and Purification Technology*, *349*, 127905. https://doi.org/https://doi.org/10.1016/j.seppur.2024.127905

Venkata Reddy, C., Reddy, K. R., Shetti, N. P., Mishra, A., & Basu, S. (2019). Chapter 30 - Recent Progress in TiO2- and ZnO-Based Nanostructured Hybrid Photocatalysts for Water Purification and Hydrogen Generation. In S. Thomas, D. Pasquini, S.-Y. Leu, & D. A. Gopakumar (Eds.), *Nanoscale Materials in Water Purification* (pp. 815-843). Elsevier. https://doi.org/https://doi.org/10.1016/B978-0-12-813926-4.00039-2

Vera, J., Herrera, W., Hermosilla, E., Díaz, M., Parada, J., Seabra, A. B., Tortella, G., Pesenti, H., Ciudad, G., & Rubilar, O. (2023). Antioxidant Activity as an Indicator of the Efficiency of Plant Extract-Mediated Synthesis of Zinc Oxide Nanoparticles. *Antioxidants*, *12*(4), 784. https://www.mdpi.com/2076-3921/12/4/784

Vignesh, S., Muppudathi, A. L., & Sundar, J. K. (2018). Multifunctional performance of gC3N4-BiFeO3-Cu2O hybrid nanocomposites for magnetic separable photocatalytic and antibacterial activity. *Journal of Materials Science: Materials in Electronics*, *29*(13), 10784-10801. https://doi.org/10.1007/s10854-018-9144-7

Volpp, J. (2023). Laser light absorption of high-temperature metal surfaces. *Heliyon*, *9*(10), e21021. https://doi.org/https://doi.org/10.1016/j.heliyon.2023.e21021

Wang, D., Loo, J. F. C., Chen, J., Yam, Y., Chen, S.-C., He, H., Kong, S. K., & Ho, H. P. (2019). Recent Advances in Surface Plasmon Resonance Imaging Sensors. *Sensors*, *19*(6), 1266. https://www.mdpi.com/1424-8220/19/6/1266

Wang, D., Shen, H., Guo, L., Wang, C., Fu, F., & Liang, Y. (2018). Ag/Bi2MoO6-x with enhanced visible-light-responsive photocatalytic activities via the synergistic effect of surface oxygen vacancies and surface plasmon. *Applied Surface Science*, *436*, 536-547. https://doi.org/https://doi.org/10.1016/j.apsusc.2017.12.002

Wang, H., Zhang, Q., Qiu, M., & Hu, B. (2021). Synthesis and application of perovskite-based photocatalysts in environmental remediation: A review. *Journal of Molecular Liquids*, *334*, 116029. https://doi.org/https://doi.org/10.1016/j.molliq.2021.116029

Wang, R., Sakai, N., Fujishima, A., Watanabe, T., & Hashimoto, K. (1999). Studies of Surface Wettability Conversion on TiO2 Single-Crystal Surfaces. *The Journal of Physical Chemistry B*, *103*(12), 2188-2194. https://doi.org/10.1021/jp983386x

Wang, Y., Zheng, Z., Li, Y., Jia, P., & Liu, T. (2022). Study on Photocatalytic Activity of Ag2O Modified BiOI/g-C3N4 Composite Photocatalyst for Degradation of RhB.

Journal of Electronic Materials, *51*(10), 5508-5520. https://doi.org/10.1007/s11664-022-09822-1

Wetchakun, K., Wetchakun, N., & Sakulsermsuk, S. (2019). An overview of solar/visible light-driven heterogeneous photocatalysis for water purification: TiO2- and ZnO-based photocatalysts used in suspension photoreactors. *Journal of Industrial and Engineering Chemistry*, *71*, 19-49. https://doi.org/https://doi.org/10.1016/j.jiec.2018.11.025

Wu, L., Luo, Y., Zhou, S., Wu, Z., & Chen, X. (2021). Fabrication of Ag-TiO2 functionalized activated carbon for dyes degradation based on tea residues. *Colloids and Surfaces A: Physicochemical and Engineering Aspects*, *627*, 127130. https://doi.org/https://doi.org/10.1016/j.colsurfa.2021.127130

Wu, M., Yan, J.-M., Zhang, X.-W., Zhao, M., & Jiang, Q. (2015). Ag2O modified g-C3N4 for highly efficient photocatalytic hydrogen generation under visible light irradiation [10.1039/C5TA03358F]. *Journal of Materials Chemistry A*, *3*(30), 15710-15714. https://doi.org/10.1039/C5TA03358F

Wu, Y., Chen, M., Lee, H.-J., A. Ganzoury, M., Zhang, N., & de Lannoy, C.-F. (2022). Nanocomposite Polymeric Membranes for Organic Micropollutant Removal: A Critical Review. *ACS ES&T Engineering*, *2*(9), 1574-1598. https://doi.org/10.1021/acsestengg.2c00201

Wudil, Y. S., Ahmad, U. F., Gondal, M. A., Al-Osta, M. A., Almohammedi, A., Sa'id, R. S., Hrahsheh, F., Haruna, K., & Mohamed, M. J. S. (2023). Tuning of graphitic carbon nitride (g-C3N4) for photocatalysis: A critical review. *Arabian Journal of Chemistry*, *16*(3), 104542. https://doi.org/https://doi.org/10.1016/j.arabjc.2023.104542

Xiao, Y., Lyu, H., Yang, C., Zhao, B., Wang, L., & Tang, J. (2021). Graphitic carbon nitride/biochar composite synthesized by a facile ball-milling method for the adsorption and photocatalytic degradation of enrofloxacin. *Journal of Environmental Sciences*, *103*, 93-107. https://doi.org/https://doi.org/10.1016/j.jes.2020.10.006

Xie, Y., Wang, X., Li, H., Wang, T., Feng, W., & Li, J. (2023). PAN/TiO2 Ultrafiltration Membrane for Enhanced BSA Removal and Antifouling Performance. *Catalysts*, *13*(10), 1320. https://www.mdpi.com/2073-4344/13/10/1320

Yamakata, A., & Vequizo, J. J. M. (2019). Curious behaviors of photogenerated electrons and holes at the defects on anatase, rutile, and brookite TiO2 powders: A review. *Journal of Photochemistry and Photobiology C: Photochemistry Reviews*, *40*, 234-243. https://doi.org/https://doi.org/10.1016/j.jphotochemrev.2018.12.001

Yang, X., Liang, J., Fu, H., Ran, X., & An, X. (2022). Fabrication of Au-Ag@TiO2 ternary core-shell nanostructures with enhanced sunlight photocatalytic activity. *Powder Technology*, *404*, 117463. https://doi.org/https://doi.org/10.1016/j.powtec.2022.117463

Yao, S., Wang, D., Li, J., You, J., Zhu, Y., Gong, W., Xu, K., Liang, Y., Yang, Y., & Yang, Y. (2024). Gas sensing activity and mechanism of Aurivillius-type Bi2MoO6 nanosheets with different crystal facets. *Sensors and Actuators B: Chemical*, *418*, 136290. https://doi.org/https://doi.org/10.1016/j.snb.2024.136290

Ye, L., Mao, J., Liu, J., Jiang, Z., Peng, T., & Zan, L. (2013). Synthesis of anatase TiO2 nanocrystals with {101}, {001} or {010} single facets of 90% level exposure and liquid-phase photocatalytic reduction and oxidation activity orders [10.1039/C3TA11791J]. *Journal of Materials Chemistry A*, *1*(35), 10532-10537. https://doi.org/10.1039/C3TA11791J

Yin, Z., Qi, S., Deng, S., Xu, K., Liu, Z., Zhang, M., & Sun, Z. (2021). Bi2MoO6/TiO2 heterojunction modified with Ag quantum dots: a novel photocatalyst for the efficient

degradation of tetracycline hydrochloride. *Journal of Alloys and Compounds*, *888*, 161582. https://doi.org/https://doi.org/10.1016/j.jallcom.2021.161582

Ying, S., Guan, Z., Ofoegbu, P. C., Clubb, P., Rico, C., He, F., & Hong, J. (2022). Green synthesis of nanoparticles: Current developments and limitations. *Environmental Technology & Innovation*, *26*, 102336. https://doi.org/https://doi.org/10.1016/j.eti.2022.102336

You, S.-J., Semblante, G. U., Lu, S.-C., Damodar, R. A., & Wei, T.-C. (2012). Evaluation of the antifouling and photocatalytic properties of poly(vinylidene fluoride) plasma-grafted poly(acrylic acid) membrane with self-assembled TiO2. *Journal of Hazardous Materials*, *237-238*, 10-19. https://doi.org/https://doi.org/10.1016/j.jhazmat.2012.07.071

Žerjav, G., Žižek, K., Zavašnik, J., & Pintar, A. (2022). Brookite vs. rutile vs. anatase: What`s behind their various photocatalytic activities? *Journal of Environmental Chemical Engineering*, *10*(3), 107722. https://doi.org/https://doi.org/10.1016/j.jece.2022.107722

Zhang, J., Zhou, P., Liu, J., & Yu, J. (2014). New understanding of the difference of photocatalytic activity among anatase, rutile and brookite TiO2 [10.1039/C4CP02201G]. *Physical Chemistry Chemical Physics*, *16*(38), 20382-20386. https://doi.org/10.1039/C4CP02201G

Zhang, W., He, H., Li, H., Duan, L., Zu, L., Zhai, Y., Li, W., Wang, L., Fu, H., & Zhao, D. (2021). Visible-Light Responsive TiO2-Based Materials for Efficient Solar Energy Utilization. *Advanced Energy Materials*, *11*(15), 2003303. https://doi.org/https://doi.org/10.1002/aenm.202003303

Zhang, X., & Jiang, S. P. (2022). Layered g-C3N4/TiO2 nanocomposites for efficient photocatalytic water splitting and CO2 reduction: a review. *Materials Today Energy*, *23*, 100904. https://doi.org/https://doi.org/10.1016/j.mtener.2021.100904

Zhang, Z., Zheng, T., Xu, J., & Zeng, H. (2016). Polythiophene/Bi2MoO6: A novel conjugated polymer/nanocrystal hybrid composite for photocatalysis. *Journal of Materials Science*, *51*(8), 3846-3853. https://doi.org/10.1007/s10853-015-9703-8

Zhou, B., Hong, H., Zhang, H., Yu, S., & Tian, H. (2019). Heterostructured Ag/g-C3N4/TiO2 with enhanced visible light photocatalytic performances. *Journal of Chemical Technology & Biotechnology*, *94*(12), 3806-3814. https://doi.org/https://doi.org/10.1002/jctb.6105

Zhu, X., Pathakoti, K., & Hwang, H.-M. (2019). Chapter 10 - Green synthesis of titanium dioxide and zinc oxide nanoparticles and their usage for antimicrobial applications and environmental remediation. In A. K. Shukla & S. Iravani (Eds.), *Green Synthesis, Characterization and Applications of Nanoparticles* (pp. 223-263). Elsevier. https://doi.org/https://doi.org/10.1016/B978-0-08-102579-6.00010-1

Zoubi, W. A., Al-Hamdani, A. A. S., Sunghun, B., & Ko, Y. G. (2021). A review on TiO2-based composites for superior photocatalytic activity. *Reviews in Inorganic Chemistry*, *41*(4), 213-222. https://doi.org/doi:10.1515/revic-2020-0025

APPENDICES

Appendix 1: Raw data analysis of OTC degradation by parameters

Effect of dosage

Catalyst: $Ag/Bi_2MoO_6/TiO_2$

0.03 g

Time (Minutes)	Abs 1	Abs 2	Abs 3	Average	Concentration	C/C_o	Removal (%)
0	0.1928	0.1927	0.1927	0.1927	10.4751	1.0000	0.0000
30	0.0955	0.0948	0.0946	0.0949	5.1601	0.4926	50.7393
60	0.0957	0.0956	0.0957	0.0957	5.1988	0.4963	50.3698
90	0.0484	0.0484	0.0484	0.0484	2.6308	0.2511	74.8852
120	0.0367	0.0367	0.0367	0.0367	1.9970	0.1906	80.9356
150	0.0341	0.0341	0.0341	0.0341	1.8536	0.1770	82.3045
180	0.0224	0.0226	0.0225	0.0225	1.2238	0.1168	88.3170

0.06 g

Time (Minutes)	Abs 1	Abs 2	Abs 3	Average	Concentration	C/C_o	Removal (%)
0	0.1930	0.1950	0.1980	0.1953	10.6159	1.0000	0.0000
30	0.0910	0.0920	0.0910	0.0913	4.9638	0.4676	53.2423
60	0.0900	0.0900	0.0910	0.0903	4.9094	0.4625	53.7543
90	0.0250	0.0290	0.0280	0.0273	1.4855	0.1399	86.0068
120	0.0190	0.0190	0.0180	0.0187	1.0145	0.0956	90.4437
150	0.0110	0.0110	0.0120	0.0113	0.6159	0.0580	94.1980
180	0.0050	0.0057	0.0056	0.0054	0.2953	0.0278	97.2184

0.12 g

Time (Minutes)	Abs 1	Abs 2	Abs 3	Average	Concentration	C/C_o	Removal (%)
0	0.1960	0.1980	0.1960	0.1967	10.6884	1.0000	0.0000
30	0.0650	0.0650	0.0660	0.0653	3.5507	0.3322	66.7797
60	0.0660	0.0650	0.0660	0.0657	3.5688	0.3339	66.6102
90	0.0230	0.0230	0.0220	0.0227	1.2319	0.1153	88.4746
120	0.0200	0.0220	0.0220	0.0213	1.1594	0.1085	89.1525
150	0.0190	0.0170	0.0200	0.0187	1.0145	0.0949	90.5085
180	0.0160	0.0160	0.0160	0.0160	0.8696	0.0814	91.8644

Catalyst: Ag/g-C_3N_4/TiO_2

0.03 g

Time (Minutes)	Abs 1	Abs 2	Abs 3	Average	Concentration	C/C_o	Removal (%)
0	0.2090	0.2100	0.2150	0.2113	11.4855	1.0000	0.0000
30	0.1910	0.1850	0.1900	0.1887	10.2536	0.8927	10.7256
60	0.1900	0.1910	0.1900	0.1903	10.3442	0.9006	9.9369
90	0.1690	0.1740	0.1690	0.1707	9.2754	0.8076	19.2429
120	0.1470	0.1450	0.1490	0.1470	7.9891	0.6956	30.4416
150	0.1250	0.1200	0.1230	0.1227	6.6667	0.5804	41.9558
180	0.1080	0.1090	0.1080	0.1083	5.8877	0.5126	48.7382

0.06 g

Time (Minutes)	Abs 1	Abs 2	Abs 3	Average	Concentration	C/C_o	Removal (%)
0	0.2130	0.2110	0.2130	0.2123	11.5399	1.0000	0.0000
30	0.1620	0.1610	0.1630	0.1620	8.8043	0.7630	23.7049
60	0.1630	0.1620	0.1620	0.1623	8.8225	0.7645	23.5479
90	0.0820	0.0880	0.0890	0.0863	4.6920	0.4066	59.3407
120	0.0620	0.0660	0.0610	0.0630	3.4239	0.2967	70.3297
150	0.0500	0.0550	0.0490	0.0513	2.7899	0.2418	75.8242
180	0.0400	0.0400	0.0390	0.0397	2.1558	0.1868	81.3187

0.12 g

Time (Minutes)	Abs 1	Abs 2	Abs 3	Average	Concentration	C/C_o	Removal (%)
0	0.2110	0.2100	0.2090	0.2100	11.4130	1.0000	0.0000
30	0.1540	0.1590	0.1580	0.1570	8.5326	0.7476	25.2381
60	0.1560	0.1560	0.1580	0.1567	8.5145	0.7460	25.3968
90	0.1040	0.1050	0.1040	0.1043	5.6703	0.4968	50.3175
120	0.0700	0.0710	0.0700	0.0703	3.8225	0.3349	66.5079
150	0.0590	0.0590	0.0580	0.0587	3.1884	0.2794	72.0635
180	0.0480	0.0490	0.0500	0.0490	2.6630	0.2333	76.6667

Effect of pollutant initial concentration

Catalyst: $Ag/Bi_2MoO_6/TiO_2$

10 ppm

Time (Minutes)	Abs 1	Abs 2	Abs 3	Average	Concentration	C/C_o	Removal (%)
0	0.1930	0.1950	0.1980	0.1953	10.6159	1.0000	0.0000
30	0.0910	0.0920	0.0910	0.0913	4.9638	0.4676	53.2423
60	0.0900	0.0900	0.0910	0.0903	4.9094	0.4625	53.7543
90	0.0250	0.0290	0.0280	0.0273	1.4855	0.1399	86.0068
120	0.0190	0.0190	0.0180	0.0187	1.0145	0.0956	90.4437
150	0.0110	0.0110	0.0120	0.0113	0.6159	0.0580	94.1980
180	0.0050	0.0057	0.0056	0.0054	0.2953	0.0278	97.2184

15 ppm

Time (Minutes)	Abs 1	Abs 2	Abs 3	Average	Concentration	C/C_o	Removal (%)
0	0.2820	0.2830	0.2810	0.2820	15.3261	1.0000	0.0000
30	0.1570	0.1590	0.1578	0.1579	8.5833	0.5600	43.9953
60	0.1500	0.1510	0.1560	0.1523	8.2790	0.5402	45.9811
90	0.0510	0.0515	0.0516	0.0514	2.7917	0.1822	81.7849
120	0.0390	0.0391	0.0380	0.0387	2.1033	0.1372	86.2766
150	0.0240	0.0243	0.0239	0.0241	1.3080	0.0853	91.4657
180	0.0180	0.0183	0.0181	0.0181	0.9855	0.0643	93.5697

20 ppm

Time (Minutes)	Abs 1	Abs 2	Abs 3	Average	Concentration	C/C_o	Removal (%)
0	0.3600	0.3580	0.3560	0.3580	19.4565	1.0000	0.0000
30	0.2280	0.2240	0.2285	0.2268	12.3279	0.6336	36.6387
60	0.2300	0.2310	0.2305	0.2305	12.5264	0.6438	35.6182
90	0.1090	0.1080	0.1050	0.1073	5.8333	0.2998	70.0186
120	0.0770	0.0760	0.0760	0.0763	4.1486	0.2132	78.6778
150	0.0580	0.0590	0.0584	0.0585	3.1775	0.1633	83.6685
180	0.0500	0.0501	0.0509	0.0503	2.7355	0.1406	85.9404

Catalyst: Ag/g-C_3N_4/TiO_2

10 ppm

Time (Minutes)	Abs 1	Abs 2	Abs 3	Average	Concentration	C/C_o	Removal (%)
0	0.2130	0.2110	0.2130	0.2123	11.5399	1.0000	0.0000
30	0.1620	0.1610	0.1630	0.1620	8.8043	0.7630	23.7049
60	0.1630	0.1620	0.1620	0.1623	8.8225	0.7645	23.5479
90	0.0820	0.0880	0.0890	0.0863	4.6920	0.4066	59.3407
120	0.0620	0.0660	0.0610	0.0630	3.4239	0.2967	70.3297
150	0.0500	0.0550	0.0490	0.0513	2.7899	0.2418	75.8242
180	0.0400	0.0400	0.0390	0.0397	2.1558	0.1868	81.3187

15 ppm

Time (Minutes)	Abs 1	Abs 2	Abs 3	Average	Concentration	C/C_o	Removal (%)
0	0.2840	0.2880	0.2850	0.2857	15.5254	1.0000	0.0000
30	0.2310	0.2330	0.2310	0.2317	12.5906	0.8110	18.9032
60	0.2340	0.2330	0.2330	0.2333	12.6812	0.8168	18.3197
90	0.1550	0.1530	0.1550	0.1543	8.3877	0.5403	45.9743
120	0.1070	0.1090	0.1060	0.1073	5.8333	0.3757	62.4271
150	0.0760	0.0760	0.0780	0.0767	4.1667	0.2684	73.1622
180	0.0570	0.0560	0.0550	0.0560	3.0435	0.1960	80.3967

20 ppm

Time (Minutes)	Abs 1	Abs 2	Abs 3	Average	Concentration	C/C_o	Removal (%)
0	0.3790	0.3780	0.3790	0.3787	20.5797	1.0000	0.0000
30	0.3160	0.3160	0.3150	0.3157	17.1558	0.8336	16.6373
60	0.3130	0.3150	0.3140	0.3140	17.0652	0.8292	17.0775
90	0.2900	0.2910	0.2930	0.2913	15.8333	0.7694	23.0634
120	0.2630	0.2660	0.2630	0.2640	14.3478	0.6972	30.2817
150	0.2390	0.2380	0.2410	0.2393	13.0072	0.6320	36.7958
180	0.2180	0.2180	0.2170	0.2177	11.8297	0.5748	42.5176

Appendix 2: Raw data analysis of antibacterial activity against *E. Coli* and *S. Aureus*

Control Experiment

E. Coli

Sample	ZOI 1 (mm)	ZOI 2 (mm)	ZOI 3 (mm)	Average (mm)	STD
Blank	0.0000	0.0000	0.0000	0.0000	0.0000
TiO_2	0.0000	0.0000	0.0000	0.0000	0.0000
Bi_2MoO_6	0.0000	0.0000	0.0000	0.0000	0.0000
BMOT	0.0000	0.0000	0.0000	0.0000	0.0000
ABMOT (1%)	6.2000	5.2000	7.3000	6.2333	1.0504
ABMOT (4%)	9.3000	8.4000	7.7500	8.4833	0.7784
ABMOT (8%)	10.9500	9.3500	10.5000	10.2667	0.8251
ABMOT (10%)	14.1000	13.4500	13.5000	13.6833	0.3617

Sample	ZOI 1 (mm)	ZOI 2 (mm)	ZOI 3 (mm)	Average (mm)	STD
Blank	0.0000	0.0000	0.0000	0.0000	0.0000
TiO_2	0.0000	0.0000	0.0000	0.0000	0.0000
g-C_3N_4	0.0000	0.0000	0.0000	0.0000	0.0000
GCNT	0.0000	0.0000	0.0000	0.0000	0.0000
AGCNT (1%)	6.6500	6.8000	7.5500	7.0000	0.4822
AGCNT (4%)	7.1000	6.6500	7.3000	7.0167	0.3329
AGCNT (8%)	8.2500	6.7000	7.1000	7.3500	0.8047
AGCNT (10%)	8.8000	8.8000	7.7000	8.4333	0.6351

S. Aureus

Sample	ZOI 1 (mm)	ZOI 2 (mm)	ZOI 3 (mm)	Average (mm)	STD
Blank	0.0000	0.0000	0.0000	0.0000	0.0000
TiO_2	0.0000	0.0000	0.0000	0.0000	0.0000
Bi_2MoO_6	0.0000	0.0000	0.0000	0.0000	0.0000
BMOT	0.0000	0.0000	0.0000	0.0000	0.0000
ABMOT (1%)	0.0000	0.0000	0.0000	0.0000	0.0000
ABMOT (4%)	8.1000	7.1000	6.8500	7.3500	0.6614
ABMOT (8%)	6.3500	7.2000	7.8000	7.1167	0.7286
ABMOT (10%)	10.3000	11.4000	9.2500	10.3167	1.0751

Sample	ZOI 1 (mm)	ZOI 2 (mm)	ZOI 3 (mm)	Average (mm)	STD
Blank	0.0000	0.0000	0.0000	0.0000	0.0000
TiO_2	0.0000	0.0000	0.0000	0.0000	0.0000
g-C_3N_4	0.0000	0.0000	0.0000	0.0000	0.0000
GCNT	0.0000	0.0000	0.0000	0.0000	0.0000
AGCNT (1%)	0.0000	0.0000	0.0000	0.0000	0.0000
AGCNT (4%)	7.5000	7.0000	8.3000	7.6000	0.6557
AGCNT (8%)	8.1000	8.2000	9.0000	8.4333	0.4933
AGCNT (10%)	9.5000	9.5000	8.8000	9.2667	0.4041

Effect of catalyst concentration

Catalyst: $Ag/Bi_2MoO_6/TiO_2$

E. Coli

Concentration (g/L)	ZOI 1 (mm)	ZOI 2 (mm)	ZOI 3 (mm)	Average (mm)	STD
10	12.1000	13.4000	13.5000	13.0000	0.7810
8	10.3000	10.3000	8.7500	9.7833	0.8949
4	9.4000	9.7000	11.8500	10.3167	1.3364
2	10.4000	10.7000	9.8000	10.3000	0.4583
1	8.1500	8.4500	10.6500	9.0833	1.3650

S. Aureus

Concentration (g/L)	ZOI 1 (mm)	ZOI 2 (mm)	ZOI 3 (mm)	Average (mm)	STD
10	13.5500	13.8500	10.0000	12.2583	2.1415
8	11.5500	11.8000	10.5000	9.7000	0.6898
4	9.7000	9.4000	9.5500	8.4833	0.1500
2	7.0000	7.9000	8.4500	7.5000	0.7320
1	6.7000	7.4000	6.4000	6.7750	0.5132

Catalyst: $Ag/g\text{-}C_3N_4/TiO_2$

E. Coli

Concentration (g/L)	ZOI 1 (mm)	ZOI 2 (mm)	ZOI 3 (mm)	Average (mm)	STD
10	11.1000	11.4000	9.8000	10.7667	0.8505
8	9.6500	13.3000	12.3000	11.7500	1.8861
4	8.4500	11.5000	9.4500	9.8000	1.5548
2	8.7500	8.4500	9.0000	8.7333	0.2754
1	8.0000	9.8000	8.4000	8.7333	0.9452

S. Aureus

Concentration (g/L)	ZOI 1 (mm)	ZOI 2 (mm)	ZOI 3 (mm)	Average (mm)	STD
10	11.7500	11.9000	12.5000	12.0500	0.3969
8	8.4500	8.8000	7.1000	8.1167	0.8977
4	7.6500	7.0000	7.6000	7.4167	0.3617
2	6.9000	7.4500	7.3000	7.2167	0.2843
1	7.2500	6.4000	6.5000	6.7167	0.4646